Fabrication of Zinc Oxide (ZnO) Nanorods on Aluminium Doped ZnO (AZO) Seeding Layers

A Dissertation Submitted to the Department of Physics for the Partial Fulfillment of the requirements for the Degree of Master of Philosophy (M.Phil.)

Mukul Hossain

Exam Roll No: 01, Registration No: 71, Session: 2016- 2017

Department of Physics, University of Dhaka,

Dhaka-1000, Bangladesh

June, 2025

DECLARATION

I hereby declare that the research presented in my dissertation, titled **"Fabrication of Zinc Oxide (ZnO) Nanorods on Aluminium Doped ZnO (AZO) Seeding Layers"** is wholly original and has not been submitted for consideration for any other academic degree. I accept full responsibility for the authenticity and integrity of the research contained within this thesis.

(Mukul Hossain)

Exam Roll No: 01, Registration No: 71, Session: 2016- 2017

Department of Physics, University of Dhaka,

Dhaka 1000, Bangladesh.

June, 2025

CERTIFICATE

This is to certify that Mr. Mukul Hossain is an M.Phil student of the Department of Physics at the University of Dhaka. As a student, he conducted his research on the topic of the **Fabrication of Zinc Oxide (ZnO) Nanorods on Aluminium Doped ZnO (AZO) Seeding Layers.** This work was carried out under our supervision and we confirm that he demonstrated a high level of skill and dedication in his research.

(Dr. Syed Farid Uddin Farhad)
Joint Supervisor
and
Principal Scientific Officer
Industrial Physics Division, BCSIR
Dhaka 1000, Bangladesh

(Dr. Ishtiaque M. Syed)
Supervisor
and
Professor, Department of Physics,
University of Dhaka,
Dhaka 1000, Bangladesh.

ACKNOWLEDGEMENTS

Firstly, thank the Almighty Allah for giving me the strength to complete this research.

I would like to express my deepest gratitude and sincere appreciation to my supervisor, Professor Dr. Ishtiaque M. Syed, Department of Physics, University of Dhaka, for his steadfast guidance, insightful suggestions, and continuous encouragement throughout my academic research and the preparation of this thesis. His mentorship has been instrumental not only in shaping the scientific direction of this work but also in fostering my development as a researcher. The successful completion of this M.Phil. thesis would not have been possible without his invaluable support and motivation.

I am equally indebted to my co-supervisor, Dr. Syed Farid Uddin Farhad, Principal Scientific Officer, Industrial Physics Division (IPD), BCSIR Laboratory, Dhaka, for his academic and technical support. His generous access to laboratory resources, unwavering supervision, and practical insights have significantly contributed to the advancement of my research.

The experimental investigations and research activities detailed in this thesis were carried out at the Energy Conversion and Storage Research (ECSR) facility, with the Industrial Physics Division (IPD) at the BCSIR Dhaka Laboratories, under the Bangladesh Council of Scientific and Industrial Research (BCSIR).

I gratefully acknowledge the cooperation and assistance provided by Mr. Mohammad Sajjad Hossain, Senior Scientific Officer, and Mr. Nazmul Islam Tanvir, Scientific Officer, both of the IPD, as well as Mr. M. S. Bashar, Principal Scientific Officer, IERD, BCSIR. Their technical expertise and support during various stages of the experimental phase greatly facilitated the smooth progress of this research.

I am deeply grateful to the faculty and staff of the Department of Physics at the University of Dhaka for their unwavering support and encouragement during my thesis journey. Finally, I am deeply grateful to my wife, Mst. Rubia Khatun, and my parents for their unwavering support, patience, and understanding throughout the entire duration of my studies and the writing of this thesis. Their love and constant encouragement have been a continuous source of strength and inspiration.

DEDICATION

This thesis is dedicated to my beloved parents and all of my teachers.

ABSTRACT

Aluminium-doped zinc oxide (AZO) thin films and ZnO nanorods (NRs) were synthesized and characterized to explore their structural, optical, and electrical properties. AZO seed layers with varying Al concentrations 2, 3, 5, and 8 mol% were deposited on soda-lime glass via spin coating, followed by hydrothermal growth of ZnO NRs. XRD and SEM confirmed vertically aligned, c-axis-oriented nanorods, with morphology influenced by doping and annealing temperature. Optimal crystallinity was achieved at 250 °C, while higher temperatures led to lattice relaxation and reduced structural quality.

Photoluminescence revealed UV near-band-edge emission (~380 nm) and visible deep-level emission (500–700 nm), with DLE intensity suppressed at 8 mol% doping, indicating reduced defect density. Both AZO and ZnO NRs showed high optical transparency, and band gaps ranged from 3.44–3.55 eV (AZO) and 3.05–3.15 eV (ZnO NRs), tunable via Al doping. The electrical conductivity and film thickness were strongly influenced by both Al concentration and annealing conditions. The favorable combination of structural integrity, high transparency, tunable band gaps, and improved conductivity renders these AZO/ZnO nanostructures promising candidates for application in a wide range of optoelectronic devices.

TABLE OF CONTENTS

Figure. No.	LIST OF FIGURES	Page No.

Table **LIST OF TABLES** **Page No.**

LIST OF ABBREVIATIONS

ZnO	Zinc Oxide
AZO	Aluminum Doped Znic Oxide
ETL	Electron Transport Layer
TCO	Transparent Conducting Oxides
XRD	X-ray Diffraction
SEM	Scanning Electron Microscopy
EDX	Energy Dispersive X-ray Spectroscopy
UV-Vis	Ultra-violate Visible
MEA	Monoethanolamine
HMT	Hexamethyl tetraamine
ZAD	Zinc Acetate dihydride
ZN	Zinc Nitrate
λ	Wavelength
μ	Mobility of charge carrier
θ	Bragg angle
D	Crystallite size
β	Full width half maximum
A	Absorbance
T	Transmittance
α	Absorption coefficient
K	Extinction coefficient
ρ	Electrical resistivity
σ	Electrical conductivity
T	Thickness

CHAPTER 1: INTRODUCTION

1.1 Introduction

Global population growth has caused unprecedented growth of energy demand, and energy generation and environmental protection have become critical issues in material science [1, 2]. The current world energy demand is 16.70 TW and is expected to increase approximately twice in the next 30 years, as a result of population increase and enhanced living [3, 4]. It is expected that demand will almost double in the next 30 years as a result of continuous population growth and increased standard of living [5]. Given the importance of energy for everyday life and economic stability, the inability to provide electricity generation based on fossil fuels affects the environment with negative impacts due to greenhouse gas emissions and global warming. There's an imminent urgency for viable energy solutions [6]. Solar power has huge environmental benefits and contributes towards sustainable development. Since no dirty gases, such as carbon dioxide or methane, are emitted, solar power helps to enhance the quality of the air, preventing global warming. In addition, studies by the National Renewable Energy Laboratory (NREL) show that if solar power is more widely deployed, it would significantly reduce emissions of nitrogen oxides, sulfur dioxide and particulate matter—all of which are hazardous to public health [6, 7]. The Sun is a great supplier of energy, for this reason, solar power is a safe, clean, and renewable alternative to reduce air, water, and ground pollution, preserving our ecology and our health with economic and environmental advantages. It provides a solution to the growing energy demand, climate change, and the depletion of resources. Solar electricity is comparatively more affordable than traditional electricity [9]. Over the past few decades, scientists have developed various types of solar cells, advancing solar energy technology. Initially, the high cost of solar energy limited its widespread adoption; however, sustained investments and technological advancements have gradually reduced costs over the past 25 years [10]. Recently, the reduction in solar energy prices has been particularly

significant. This trend is encapsulated by Swanson's Law, which observes that “the price of solar photovoltaic modules tends to drop by approximately 20% for every doubling of the collective shipped volume” [11]. As a result, solar energy has become more competitive and attractive due to price reductions. The development of solar cells, which transform light energy into electrical energy, was driven by the demand for a device that could convert sunlight into electricity. Solar cells have evolved through several generations, including the first, second, and third generations.

The first-generation solar cell is mainly based on the Silicon wafer. This technology achieved up to 24% efficiency. The second-generation solar cells are based on thin films, including amorphous silicon, as well as CdTe and CIGS thin films [12]. This technology significantly reduces the production cost but has a lower efficiency than the first-generation solar cells. Some of the materials are not friendly and have a disposal problem. Third generation solar cells include polymer-based dye sensitised, nanocrystal-based and concentrated solar cells [13]. This generation has the lowest production cost of all the solar cells produced to date, but it has a significant problem: it has achieved an efficiency of only up to 10% [14].

Among them, zinc oxide (ZnO) is one of the promising materials for making the next generation of solar cells due to its wide bandgap, electron transport layers, transparent conductive oxides, and cost-effective synthesis methods. In this study, we have prepared Al-doped zinc oxide (AZO) seeding layers on the soda lime glass (SLG) substrate by the spin coating method. And subsequently growth of zinc oxide nanorods (ZnO NRs) on AZO seed layers by the hydrothermal method [15]. Also, the annealing effect at different concentrations was examined according to Farhad et al.

1.2 Motivation

In modern times, solar energy technology has become increasingly popular for its low cost of electricity. Silicon cells are traditional and achieve high efficiency, but the disadvantage of the

silicon-based solar cells is their expensive production, installation cost, and environmental problems such as toxicity, recycling, and disposal. Many researchers are concentrating on the development of solar cells that deliver energy at high efficiencies, cost-effectiveness, and eco-friendliness [16, 17]. In this case, ZnO has played an important role due to its several advantages, such as earth abundance, non-toxic nature, low-cost fabrication facility, and direct energy band gap for conversion of solar energy into electrical energy.

Several studies have focused on ZnO is an n-type semiconductor. it is non-toxic, affordable, widely available in nature, and environmentally friendly [18-20]. Zinc oxide has a wide band-gap (3.3-3.4 eV) and a large exciton binding energy (~60 meV) [21, 22]. It has a large electrical conductivity, simple crystal-growth techniques, and also produces low-cost optoelectronic devices. Because of the wide band gap of ZnO, it can absorb ultraviolet light, transparent to visible light. ZnO has excellent electron mobility compared to TiO_2. ZnO and TiO_2 are commonly used as n-type window layers in solar cells, but ZnO is better than TiO_2 [23]. because it allows electrons to move more easily and can be made at lower temperatures, which improves charge movement and makes it cheaper and easier to produce. ZnO is a commonly used electron transport layer (ETL), transport conducting oxide (TCO) layer of thin film solar cells and can be transparent in the visible range [24]. The material properties can be changed by doping, such as surface area, structural optical properties and conductivity of the semiconductor [25]. By this process, energy storage ability is increased, electron transfer is promoted, and lattice mismatches between them are reduced [26]. Doping is a defect that effectively modifies the surface area, structural, optical, and electrical properties of materials. Aluminium is considered suitable for doping to ensure the sustainability of ZnO thin films, which are also recognized as non-toxic and low-cost. Therefore, Al-doped zinc oxide (Al: ZnO) can be regarded as an essential material for transparent conductive oxide (TCO) technology [27]. Al is widely chosen to dope ZnO for TCO applications because Al-doped ZnO films

(AZO) exhibit very low resistivity compared to ITO films, which are currently used commercially. Al-doped ZnO (AZO) seed layers are effective for fabricating vertically aligned ZnO nanorods (NRs), which are essential for optoelectronic applications due to their high surface area and physical properties [28]. The seed layers generally promote better alignment, higher density, and improved electrical and optical characteristics. It made preferred applications in sensors, optoelectronics, and photovoltaics. This study focused on the fabrication of AZO seeding layers by the spin coating technique and vertical growth of zinc oxide nanorods (ZnO NRs) by the hydrothermal method. AZO seeding layers were important for growing vertically aligned ZnO Nanorod assemblies [29-30]. The deposition of AZO seed and ZnO NRs thin films provided the energy storage device with more scope, which is another goal of the current effort.

1.3 Objectives of the Thesis

In this research, the objectives are given below:

- To synthesise aluminium-doped zinc oxide (AZO) seeding layers on the soda lime glass (SLG) substrate by the spin coating method.
- Aluminium doping concentration at 2%, 3%, 5%, and 8 mol% on the procured zinc acetate dihydrate (ZAD) solution.
- Vertically grown ZnO NRs on AZO thin films by the hydrothermal method.
- To determine the film's thickness using a home-built gravimetric method.
- To examine the surface morphology of AZO and ZnO NRs thin films through Scanning Electron Microscope (SEM) analysis.
- To investigate the structural characteristics of the synthesised samples using X-ray Diffraction (XRD).
- To evaluate the elemental composition of AZO thin films by Energy Dispersive X-rays (EDX).

- To determine the optical characteristics, like optical band gap, transmittance, and diffuse reflection, using UV-VIS-NIR spectroscopy.
- To estimate the average crystal size of the prepared films.
- To calculate the resistivity of the films using a four-point collinear probe method.

1.4 Outline of the Thesis

The thesis structure is as follows:

Chapter one discussed the overall current scenario of global energy demand, particularly solar energy, focusing on zinc oxide (ZnO) as a promising, cost-effective and non-toxic material for next generation energy harvesting devices. It also described the motivation, the objectives, and the goal of the current research.

Chapter two discussed in recent two-decade literature review concerning thin films.

Chapter three represented the comprehensive study of the theoretical background on the research related to AZO thin films and ZnO NRs.

Chapter Four discussed the properties of ZnO material, the characterization techniques, and the fabrication of AZO seed layers, ZnO nanorod thin films, and experimental details. It further describes the apparatus and techniques used for the electrical, structural, photoluminescence, and optical characterization of the deposited thin films.

Chapter Five represented the result and discussion of the surface morphology, structure, Photoluminescence, and electrical and optical properties of the deposited thin films obtained during the study.

Chapter Six provided a summary of findings and future research work.

Chapter 2: Literature Review

2.1 Introduction

The photovoltaic effect was discovered in 1839 by French physicist Alexandre Edmond Becquerel, who built a silver platinum-coated electrolytic cell. It was found that the electric current could be enhanced in the photo-exposed cell [31]. Photoconductivity in selenium was first observed by Willoughby Smith in 1873. Three years later, the occurrence of the photovoltaic effect in selenium was reported by Adams and Day. In 1914, the efficiency of the solar selenium cell was found to be 1%. An energy barrier was discovered to be part of both selenium and copper-copper oxide solar cells by Goldman and Brodsky in the same year [32, 33]. During the 1950s–1960s, an array of silicon solar cells was developed. A year later, the first solar cell made from a silicon single crystal, with a conversion efficiency of 6%, was produced by Chapin, Fuller, and Pearson [34]. A conversion efficiency of 6% was also claimed for cadmium sulfide / cuprous sulfide in the same year [35]. As a result, many other thin-film solar cell materials, such as CdTe, CdS, AZO, and SnO_2, were studied by various research groups, as the corresponding optimal efficiency was procured in theoretical research work [36]. In the 1970s, the more high-profile research focused primarily on the fabrication and characterization of simpler ZnO devices [37-40]. Other ZnO studies were published with Group-III [41] or Group-V [42] components, but extensive ZnO nano-structural development began in the 1980s. In the recent two decades number of research areas in ZnO has expanded. Review of some of these works are given below:

Manzen et al. [43] investigated transparent conductive oxide (TCO) coatings for flexible devices, focusing on the limitations of Indium Tin Oxide (ITO), which is rigid and contains the rare element Indium. To address these issues, they replaced ITO with an Al-doped Zinc Oxide (AZO) transparent conductive sheet. The researchers developed flexible electrodes by fabricating films on Polyethylene Naphthalate (PEN) substrates. They evaluated the

characteristics of the films by altering deposition conditions during AZO and silver (Ag) deposition. Their results showed that a 10 nm Ag layer achieved the highest resistivity of 1.24 Ω-cm and a transmittance of 84.8%.

Mandal et al. [44] in 2020 studied the growth of high-conductive, transparent AZO thin films on a glass substrate by DC magnetron sputtering with ZnO: Al (2 wt%) as the material. The films were annealed in oxygen and nitrogen ambient conditions at temperatures of 200, 300 and 400 °C. It is observed that the better crystallinity of AZO films has grown with higher annealing temperatures. The elemental composition was also influenced by annealing conditions. The films showed more than 70% of transmittance visible regions, and the annealing of the precursor varied the electrical properties of them, such as carrier mobility, concentration and resistivity.

Agarwal et al. [45] in 2020, reported a high efficiency, low-cost approach to the realisation of optoelectronic device anode by the synthesis of Al-doped ZnO nanorods (NRs) in two or successive steps. Seed layers were obtained by sol-gel, and ZnO NRs were grown by hydrothermal synthesis. For (1-10 %) doped nanorods, the rod diameters were 232 and 297 nm, respectively, with good electrical and optical characteristics. More importantly, the bandgap of the Al-doped ZnO NRs has been likewise reduced from 3.23 eV to 2.73 eV, and photoluminescence spectra also exhibited the emissions in the UV as well as the visible region, which makes it a potential candidate in the field of optoelectronics.

Sarma et al. [46] in 2019 investigated Al-doped ZnO (AZO) thin films as a candidate to replace indium tin oxide (ITO) as a transparent electrode in optoelectronic devices. Pulsed DC magnetron sputtering was employed by them to get AZO thin films with c-axis preference. The crystallites were (16–21) nm in diameter, and the films showed sheet resistance values of (9-45 Ω/sq) and were suitable for electronic purposes. With the high stability and strong

figures of merit, these films were suggested as a potential candidate for transparent photovoltaic electrodes.

Farhad et al. [47] in 2019 examined ZnO seed layer deposition using three methods, and they found that the highest c-axis texturing is obtained for drop casting, as evidenced by XRD. The optical band gap of nanocrystalline ZnO seeds and ZnO nanorods (NRs) was observed to be 3.30 eV and falls in the 3.18–3.25 eV region, respectively.

Tonny et al. [48] in 2018 investigated the sol-gel spin coating process of AZO films and discussed the effect of film thickness on the structural, electrical, and optical properties. Their x-ray diffraction (XRD) studies indicated that the films were c-axis oriented, and the sharpness of the orientation improved with an increase in the film thickness. As the film thickness grew from 295 nm to 1031 nm, the conductivity of the films increased significantly, from 2.35 Siemens/cm to 20156.27 Siemens/cm, while sheet resistance decreased from 606,300 ohms/sq to 2.08 ohms/sq.

Farhad et al. [49] in 2018, they used simple chemical methods to deposit oriented ZnO seed layers and nanorods (NRs) on soda-lime and FTO-coated glass substrates. X-ray diffraction confirmed c-axis alignment, and UV-VIS-NIR spectroscopy revealed optical band gaps of 3.45–3.95 eV and 3.20–3.25 eV for the seed and NRs, respectively.

Shahid et al. [50] In 2016 fabricated pure and Al-doped ZnO thin films on glass substrates using the sol-gel method. The films were dried at temperatures of 170°C and 400°C. Scanning electron microscopy, X-ray scattering, and Fourier transform infrared spectroscopy confirmed the successful formation of Al-doped ZnO layers. The 1% Al-doped films exhibited reduced electrical resistivity and enhanced charge carrier concentration, attributed to the uniform distribution of crystallites, compared to pure ZnO and 2% Al-doped films.

Narayanan et al. [51] in 2015 have investigated using Hydrothermal ZnO nanorods that were annealed in air at 350, 450, and 550 degrees Celsius. The morphological, structural, optical,

and electrical properties of the ZnO nanorods were produced by different annealing temperatures of the samples. They discovered that as the annealing temperature rises, the diameter of the nanorods grows. The crystallinity of Nano rods improves as the annealing temperature rises, and they relax from compressive pressure, as evidenced by XRD data and preferentially directed development along the (0 0 2) direction. The ZnO nanorod structures were annealed at different temperatures; the sample annealed at 550 ^{o}C has the least resistivity of 1.62 x 10-4 cm.

Kim et al. [52] in 2014 investigated the effects of Cu, Ag, and Al dopants on the properties of ZnO nanorods grown by chemical solution deposition on FTO-coated glass substrates. The introduction of Cu dopant significantly improved the length and crystallinity of the nanorods without causing any structural degradation. However, their visual transmittance was somewhat lower compared to undoped ZnO nanorods. In contrast, doping with Ag led to a reduction in both the length and crystallinity of the nanorods, while the transmittance of the ZnO: Ag nanorods remained high.

Kim et al. [53] (2013) examined the structural and optical properties of ZnO, Ga-doped ZnO, Al-doped ZnO, and In-doped ZnO nanorods using various characterization techniques. The incorporation of different dopants allowed for the modulation of the ZnO nanorod size, and all the nanorods exhibited excellent alignment when grown on ZnO seed layers. The reduction of the diameter of the nanorods increased with the dopants. Moreover, it was further demonstrated that the dopants played a significant role in tuning various properties of ZnO nanorods, such as size, lattice constant, residual stress, bond length, photoluminescence (PL) properties, transmission, optical band gap, and mechanical strength.

Xiaoyan et al. [54] in 2011 investigated the shape and microstructure of the ZnO Nanosheet network. Characterization using XRD, FTIR, SEM, TEM and UV–vis spectroscopy was presented. The investigated products grown on a glass substrate had a crystalline hexagonal

wurtzite structure. ZnO crystal structure seems to be ultra-long and ultrathin zinc oxide nano-sheet networks. A green emission at about 494 nm and three blue emissions at 452, 459, and 469 nm were found. Hence, the zinc oxide nanosheet network has room temperature photoluminescence properties.

Benelmadjat et al. [55] in 2010 recorded three blue flashes at 452 nm, 459 nm and 469 nm and a green emission at 494 nm, which is a clear demonstration that the ZnO Nano layer network possesses the room temperature photoluminescence (RTPL).

Smirnov et al. [56] in 2010, Spin-coating has been used to deposit a thin layer of zinc oxide (ZnO) in the glass layer. Following deposition, the films were heated to 100 degrees Celsius to remove any extraneous elements. To finish the oxidation process, the films were annealed at 500 degrees Celsius. The hexagonal structure of the polycrystalline ZnO film is obtained by X-ray splitting. As a rule, the crystals are oriented along a plane parallel to the surface of the layer (0 0 2). The films exhibit a remarkable clarity in the spectral region of 450 nm to 1300 nm (more than 75%). Analyzing absorption spectra reveals the direct existence of band-to-band transitions. The optical energy band gap is observed in the range from 3.15 eV to 3.25 eV.

Ratana et al. [57] in (2009) utilized a sol-gel dip coating of PVP-modified zinc acetate dihydrate and aluminium chloride hexahydrate solutions to create a thin film of both undoped and Al-doped ZnO on a glass substrate. Both thin films' XRD patterns indicated a strong preference for orientation along the c-axis. The exposed ZnO thin film exhibits an average grain dimension of approximately 101 nm. Conversely, as evidenced by AFM images, the grain size diminished to around 49 nm at 8 mol per cent Al. Thin films were found to be directly between the optical band gap 3.70 and 3.87 eV.

Czternastek et al. [58] in 2003 **"**A sol-gel dip-coating of PVP modified zinc acetate dihydrate and aluminum chloride hexahydrate solution forms a non-doped and Al-doped ZnO thin film over a glass layer. The XRD patterns of both thin films showed a significant preference for

orientation along the c-axis. According to AFM images, the average grain size of an undoped ZnO thin film was around 101 nm, whereas the least average grain size with 8 mol percent Al was about 49 nm. Thin films' direct optical band gap was discovered to be between 3.70 and 3.87 eV".

Shishiyanu et al. [59] in 2004 investigated the properties of tin-doped ZnO thin films for use as NO2 gas sensors. Doping with tin enhanced the sensitivity to 1.5 ppm NO2 in the atmosphere and reduced the operating temperature. The best sensitivity was obtained with a tin content of 5–10% in the ion solution and an RPP temperature of 550–650 °C.

Ibanez et al. [60] in 2004 because steel was a common foundation element for solar energy goods, spray pyrolysis has been applied to produce ZnO thin films on aluminized steel to provide an effective barrier coating with reduced temperature emittance. Their findings indicated that when substrate coverage is assured, anti-corrosion efficiency rises, with deposition time and substrate temperature being critical variables in satisfying the optical criteria of ZnO-coated galvanized steel.

Mahalingam et al. [61] in 2007 electrodeposited zinc oxide thin films onto SnO2: F doped conducting glass substrates underwent microstructural analysis. The hexagonal wurtzite structure was discovered by XRD research, and the variance of texture coefficient for different cathode potentials was investigated. The microstructural parameters of ZnO thin films were studied, and they were discovered to be reliant on the wideness of the film and the bath temperature.

Zhao et al. [62] in 2006 orientation consisting of ZnO thin films (0 0 2) was successfully formed in a quartz glass substrate using a vibrating laser removal of a Zn target in an oxygen environment at a relatively lowest point temperature range of 100-250^{0}C. The structural and optical characteristics of the film were investigated, and the findings were consistent with earlier studies.

Inoue et al. [63] in 2005 **t**hermal properties of amorphous zinc oxide non-doped (ZnO) thin films between the room temperature and 673k have been studied, and samples produced at the room temperature for pulsed laser deposition. Their findings reveal that as deposited films as well as heat treatments have an amorphous structure, with a random hexagonal ZnO network and latter with ZnO crystallized. The thermos compatibility of a ZnO thin film with the structure of the amorphous and variable range hopping conduction was suggested.

Zhao et al. [64] in 2013 discussed the optical and electrical features of zinc oxide thin films deposited on silicon substrates via a double RF co-sputtering technique. X-rays are amorphous in nature and X-rays are photoelectron spectra, indicating the C-axis (002) orientation with well-grown ZnO films and stunning chemical bond configurations. Furthermore, photoluminescence studies indicated that the ZnO films band-gap is 3.4 eV. The ZnO thin film exhibited hexagonal columnar morphology. It demonstrated a response to UV light at room temperature with a cut-off wavelength of 370 nm.

Gumus et al. [65] in 2006 **t**he method of spray pyrolysis was studied the optical and electrical characteristics of zinc oxide thin films produced. The films in visible ranges exhibited good transmittance, absorbance, and reflectance. Transmittance spectra interference was used to derive the absorption coefficient and film thickness. The band gap energy and diameter of the films were calculated to be 3.27 eV and 0.31-0.52 m, respectively. X-ray diffraction was used to analyze the crystallographic structure of the films. The films exhibited an amorphous morphology, measured at 40 nm, with a preferred (002) orientation on the substrate.

Mitra & Mukhopadhyay [66] in 2007 the exposure of zinc oxide (ZnO) thin film to methane (CH4) was investigated. The sensitivity, response time, and recovery process of a sensor element have all been investigated. The effect of operating temperature on sensor material performance was investigated, and a temperature of around 2000C was chosen as the optimum

temperature. At this temperature, In the presence of 1 vol percent methane (CH4) in the air the sensor element exhibited a sensitivity of around 86%.

Suwanboon et al. [67] in 2007 performed the visualization of the doping effects of Al and Mn on the optical and structural properties of ZnO films synthesized by the sol-gel method. They observed that Al ions were important in enhancing c-axis direction, but Mn ions hindered c-axis formation. Grain sizes are lowered in the Al and Mn doped in ZnO. The lowest average grain size with 10% Mn doping was 25 nm. The ready thin films band gap value ranges from 3.24 to 3.96 eV.

Hwang et al. [68] in 2007, the most recent advancements in ZnO epitaxial film development, doping control, system manufacturing procedures such as etching and ohmic contact creation, and ultimately the production and properties of ZnO light-emitting diodes were addressed.

Ilican et al. [69] in 2008 Sol-gel spin coating ZnO thin films on glass substrates at different speed rotations. The structural, optical, and electrical features of the films were correlated with their deposition conditions. Direct band gap energy was evidenced by results from optical absorption studies. The optical energy band gaps and Urbach energies offilms were quantified.

Djelloul et al. [70] in 2008 investigated how variations in temperature affected the structural and morphological properties of ZnO thin films deposited by Ultrasonic Spray Pyrolysis. Different textures of ZnO films were obtained depending on growth conditions. Certain preparation conditions were crucial to obtain exclusive (1 0 0) or (0 0 2) oriented films. Optical studies revealed that the films exhibited an average transmittance of ~90% and 3.26 eV direct band gap.

Mondal et al. [71] in 2013 the c-axis orientation was greatly improved due to Al integration, as shown by a substantial increase in the amplitude of the (002) peak as compared to other hexagonal ZnO peaks. The SEM (Scanning electron micrograph) cross sectional view also shows the growth of bulky crystallites perpendicular to the substrate. Because of the Al doping,

the film's resistance reduced by around one direction of magnitude. However, aluminum incorporation had no effect on the beginning barrier value of 0.31eV for ZnO film.

Rahmani et al. [72] in 2009 Cu doped ZnO thin films were deposited for NO2 detection using spray pyrolysis and showed an n-to-p transition. Morphological, optical and gas-sensing properties of these films were evaluated. Exposure to NO2 changed the resistance of the films, suggesting p-type conduction in the doped samples. The observed reduction in the band gap in the UV-Vis spectra indicated an increase of Cu absorption in ZnO. The presence of holes in ZnO films that results in p-type conductivity can be ascribed to Cu atoms occupying Zn sites. The X-ray diffraction data verified the amorphous states of the samples as well as their hexagonal structures, with an observed decreasing intensity corresponding to the (002) peak when more Cu was introduced. Hall effect measurements confirmed Cu-doped ZnO thin films exhibit p-type conduction, which was verified by Seabeck effect measurements.

Xu et al. [73] in 2011 examined the structural and optical characteristics of sol–gel synthesized ZnO thin films with adjustable thickness. All samples possess wurtzite structure with a preferential orientation in the order of the c-axis of the substrate, according to structural analysis. The films exhibited less structural disorder and a higher crystalline quality with increasing thickness. A changeover from vertical to lateral crystal growth mode was observed over 270 and 360 nm thickness. Optical characterizations indicated that the refractive index and strength of ultraviolet emission were enhanced with larger film thicknesses.

Singh et al. [74] in 2010 studied the impact of indium doping on zinc oxide films prepared via the chemical spray pyrolysis technique. Their findings revealed that as the indium concentration increased, the crystalline quality of the films decreased, while the electron concentration significantly rose, leading to heavily n-type films. Additionally, they observed a reduction in both the crystallinity and surface roughness of the films with higher indium doping levels.

Hoang et al. [75] in 2008 investigated the magneto-optical properties of ZnO:Co nanocrystalline films produced by spray pyrolysis. The films, which were in the wurtzite phase, had grain sizes of approximately 20 nm. The ferromagnetism was found in 5% Co-doped ZnO films at room temperature. The transmission and optical MCD measurements showed that Co^{2+} ions occupied the tetrahedral sites of the ZnO wurtzite lattice. The MCD spectra indicated that the observed ferromagnetism was not caused by carrier-induced one.

Islam et al. [76] in 2019 studied the structural, morphological, optical, and photoluminescence properties of ZnO NRs on ZnO seed thin films prepared by three methods. The ZnO(DC) seed layer showed the highest degree of c-axis texture among the others. The surface morphologies and crystallographic orientations of the resultant ZnO NR films were strongly dependent on the c-axis-oriented ZnO(DC) seeding layers. The optical band gap energies of the ZnO(DC) seed layer and ZnO NRs analyzed by UV–VIS-NIR diffuse reflection were estimated as 3.30 eV and (3.18–3.25 eV), respectively. Room temperature PL studies indicated a sharp near-band-edge emission peak around 380 nm for the nanostructured ZnO films. Moreover, no defect-related green-yellow emission peaks were observed in the ZnO nanorod arrays.

2.2 Aim of the Thesis

This study aims to fabricate a seed layer of different concentrations of aluminum-doped zinc oxide on top of the glass substrate using the spin coating method and grow ZnO nanorods on top of it through the hydrothermal method. This study aims to investigate the effects of AZO seed layer thin films and ZnO nanorods on the structural, surface morphology, electrical, and optical properties of the above-mentioned materials.

Chapter 3: Theoretical Background

3.1 Introduction

The study of thin films has been highly promoted in various fields of solid-state physics and chemistry. Thin films are typically deposited by a technique called thin-film deposition. This method allows for the accurate control the thickness (often within tens of nanometers). Molecular beam epitaxy techniques facilitate the atomic-level deposition of materials layer by layer, providing remarkable precision in the manipulation of the film's characteristics.

The composition, thickness, and architecture of films control the properties and performance of thin films extensively. Moreover, the properties of the surfaces in materials are becoming increasingly important in modern materials science with miniaturization of technology and the approach to the surfaces/volumes proportion for technology. This difference underscores the vital roles that surfaces play both in their interaction with electromagnetic fields, light and the environment and, through such interactions, how readily materials may corrode and degrade.

Thin film properties are different in comparison to the same material in bulk, and the differences are important to their applications. Thin and thick films are not always sharply separated with respect to thickness, but thin films are usually considered to be less than 1μm thick. It is generally the case that a movie is labelled “thin” for being significant [77-80].

3.2 Thin Film Formation

The thin film deposition process consists of three fundamental phases:

3.2.1 Film Deposition: In this initial phase, nuclei are formed as deposited material interacts with the substrate, influencing the quality of the resultant thin film through nucleation characteristics.

3.2.2 Growth (Source to Substrate): During growth, atoms or molecules from the vapor phase are accumulated on the substrate, with the growth mode influenced by various parameters affecting film attributes.

3.2.3 Integration (Particle Bonding on the Surface and Thin-Film Formation): This phase of film formation is finalized as single-layer particles adhere to the substrate, with adhesion quality, density, and structural integrity being critical for functionality.

3.3 Different Stages of the Growth Mechanism of Thin Films

Andrade studied the optical transmission behaviour of silver films, and his conclusions closely matched findings from electron microscopy. The growth of nuclei characterizes the development until a solid structure is formed. Based on electron microscope observations, the following stages of the growth procedure were identified:

- The cluster creates a stable nucleation.
- The nucleation process goes to an irregular form and then starts to grow.
- The island stages denote distinct phases of formation.
- The coalescence stage denotes a more hexagonal shape and is frequently imperfect.
- The channel stages refer to specific developmental periods.
- The continuous film stages illustrate ongoing processes.

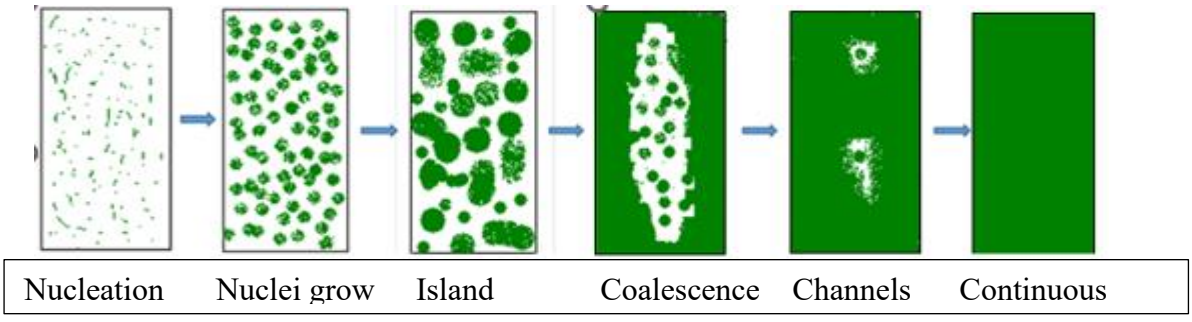

Figure.3.1 Various stages of thin film growth mechanism [81]

3.4 N-Type Thin Film Semiconductor

Zinc oxide (ZnO) is a widely used n-type semiconductor material used in thin-film solar cells and optoelectronic devices. ZnO has several advantages to be considered as a promising candidate for not only transparent electronics but also for photovoltaic applications due to its large band gap (3.37 eV) and high electron mobility. Zinc oxide (ZnO) is naturally an n-type semiconductor due to intrinsic defects such as oxygen vacancies and zinc interstitials. When ZnO is doped with group III elements like aluminium (Al), gallium (Ga), or indium (In), these dopants introduce additional free electrons, which compensate for the positive charges at the zinc sites, resulting in a decrease in resistivity.The main interest is which group (III) element is the most suitable dopant for ZnO to achieve a highly conductive and transparent oxide (TCO) for a solar cell.

First Ga exhibits a strong relationship with Zn, because the ionic and covalent radii of Ga and Zn are similar to one another. Additionally, the covalent bond length of Ga-O (1.92 Å) is closer to Zn-O (1.97 Å) [82]. It is reasonable to expect that Ga atom substitution on Zn sites will induce very little lattice strain or lattice deformation within the ZnO. At the same time the covalent bond length of Al-O is 1.96 Å (theoretically calculated by taking Al as 1.3Å and 0.66 Å for O, but estimated value is 1.87Å) is also quite close to Zn-O (1.97Å) and the covalent radii of Al (1.26 Å) is also quite close to Zn (1.31Å) [83]. It may be concluded that Ga and Al will have similar properties in ZnO.

However, Al is widely chosen to dope ZnO for TCO applications because Al-doped ZnO films (AZO) exhibit very low resistivity compared to ITO films, which are currently used commercially [84]. AZO has a wide band gap ranging from 3.4 to 3.7 eV and exhibits excellent optical transmittance in the wavelength range of 400 to 700 nm.

3.5 Thickness Measurement of Thin Film by Gravimetric Method

The gravimetric method is a general approach for determining thin film thickness. This method works by dissolving or etching the thin film in a chemical solution, and then the mass (or volume) change is used to calculate the thickness [85].

3.5.1 Thickness Calculation

The thickness of the thin film is calculated based on the amount of material removed during the etching process. The equation for the thickness (t) can be derived using the following formula [86]:

$$t = \frac{M_1 - M_2}{\rho * A}$$

Where M_1 mass is before etching, and M_2 mass is after etching. ρ is the density of the film material, and A is the area of the thin film. This chemical wet process is beneficial for measuring the thickness of thin films in various materials in research and industry [86].

3.6 Solar Cell and Thin Film Solar Cell

Solar cells are produced from different semiconductors using various fabrication methods. The main component of both single-crystal and multicrystal solar cells is silicon. Single-crystalline silicon solar cells have a maximum efficiency of about 25%. Low-energy electromagnetic radiation and infrared radiation greatly affect them [87]. Single-crystal silicon can be grown using a variety of methods. The float-zone (FZ) and Czochralski (Cz) methods [88] are well-established practices. Furthermore, single-crystal silicon can also be produced using "ribbon-growth"[89] techniques. Polycrystalline silicon solar cells, on the other hand, are less costly and have a maximum efficiency of less than 20%.

With lower requirements for semiconductor material, thin film solar cells are thought to be a promising alternative, with a lower cost of process than that of crystalline silicon solar cells. They can be made of low-cost materials, such as glass, polymer, plastic etc. The thin film

solar cells are advantageous in easy preparation process and the potential of high conversion efficiency. There are various thin film deposition techniques that are cheaper than the complex and clean procedures in silicon solar cell production.

3.7 Characterization of Structure

Multiple methods are used to characterize the structural, optical, and electrical properties of thin films. Structural, surface morphology, elemental composition and optico-physical properties of the film which are described below values of the atomic positions (atoms' coordinates).

3.7.1 X-ray Diffraction

The X-ray diffraction (XRD) is a method used for the crystal analysis of a material (to analyze the crystal lattice) by measuring the diffraction of X-rays due to the material. It is a practical method for crystal and phase identification and for atomic crystallographic configuration in solid states. Crystallinity and unit cell dimensions are determined by X-ray diffraction in the laboratory. XRD is a widely used technique for analyzing the crystal structures of materials [90]. In material science and engineering, as well as in geology and environmental investigations, X-ray powder diffraction is extensively applied to rapidly identify unknown crystalline minerals. The first step to be considered is the milling of a compound, followed by the milling of the sample into a fine powder, and then the assessment of the purity of the sample residue. Other applications include crystalline characterization, unit cell dimension assessment, and modal quantity quantification of the crystals. Additionally, X-ray powder diffraction can be used to detect single-grain raw materials.

3.7.2 X-ray Diffraction and the Bragg Equation

The preferential reflection of X-ray beams incident on crystal fracture faces at certain angles was studied by Sir W.H. Bragg and Sir W.L. Bragg in 1913 [90]. This effect is considered a model of X-ray signal interference. The Bragg law describes the angles at which radiation is diffracted by a lattice of planes. In 1913, W.L. Bragg delineated the conditions for constructive X-ray interference from parallel lattice planes. The reflection of coherent waves from identical planes in crystals is analogous to a lightly silvered mirror, with a minor portion of radiation reflected from each plane.

3.7.3. The Bragg Equation

Bragg's equation is widely used to determine crystal structures through X-ray diffraction analysis. It describes the condition for constructive interference between X-rays scattered from different planes of atoms in a crystal lattice. The Bragg equation is given by:

$$n\lambda = 2dsin\theta$$

Where n is an integer representing the diffraction order, λ is the wavelength of the incident X-rays, d is the distance between the crystal planes, and θ is the Bragg angle.

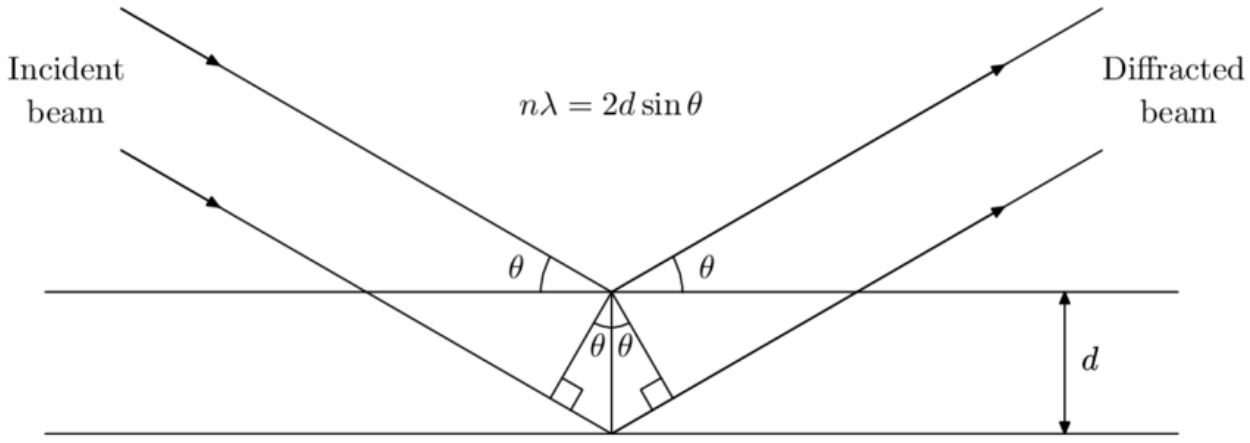

Figure 3.2: Schematic diagram of XRD and Bragg's equation [94])

3.8 Lattice Constants

The interval between planes in the hexagonal structure is provided as

$$\left[\frac{1}{d^2{}_{hkl}}\right] = \frac{4}{3}\left[\frac{h^2 + hk + l^2}{a^2}\right] + \frac{l^2}{c2}$$

where, the indices of the crystal planes are h, k and l; the interplanar spacing is $d_{hkl}$and diffraction angle is θ as

$$\frac{1}{d_{hkl}} = \frac{2sin\theta_{hkl}}{\lambda}$$

The CuKα line has an X-ray wavelength of 1.54178 Å [95]

3.9 Dimensions of Crystallites

Determination of the crystallite size(D) by Scherrer formula [82]

$$D = \frac{k\lambda}{\beta cos\theta}$$

Where K represents 0.94, λ is the X-ray wavelength, and FWHM refers to the full width at half maximum of the XRD peak.

3.10 Thin Film Surface and Composition Analysis

The analysis of surface morphology and composition in the study of thin films is crucial and more important, while the arrangement and measurement of element abundance in this sample identify the characteristics of X-rays. The analysis of the morphology of surface and compositional prepared thin films was studied using scanning electron microscopy (SEM) [96] in this thesis.

3.10.1 Principle of Scanning Electron Microscopy

The SEM works with a low-acceleration voltage to take high-resolution images [97]. A post-acceleration voltage is applied to the electron beam through an acceleration pipe in the direction of the objective lens. A checking electrical field is generated between the acceleration tube and the sample when an overlapping voltage is applied to it, which negatively influences the main electron beam. A slow electric field is imposed before the sample. It pulls the electron beam

and secondary signals, like reflected electrons, into the acceleration tube. Secondary signal detectors, which are mounted above the acceleration tunnel, track the signals.

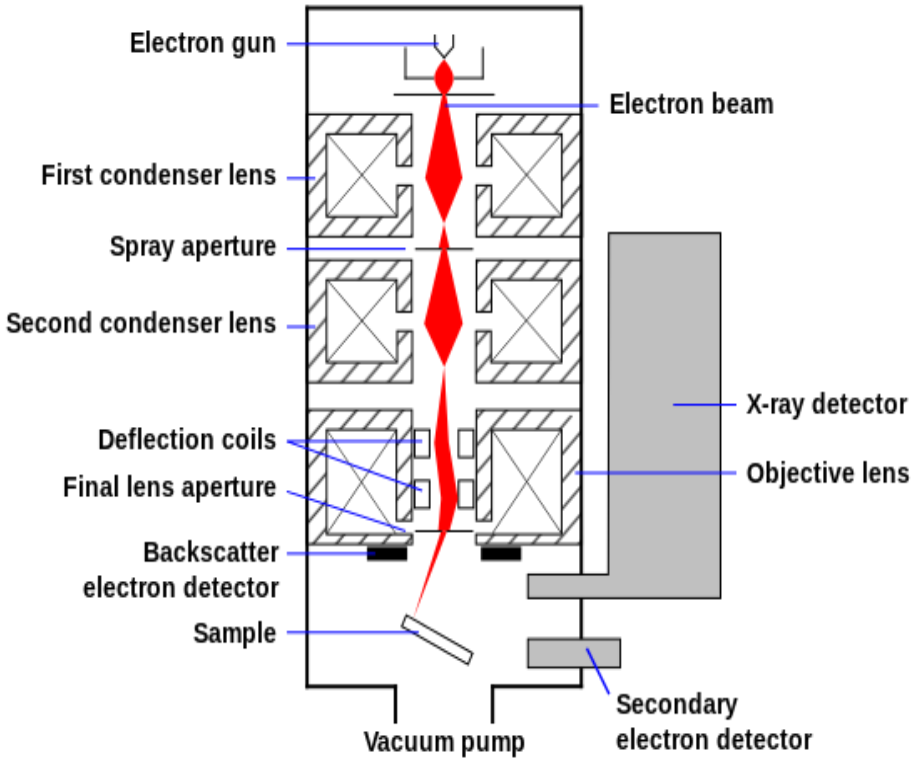

Figure 3.3: Principle of Scanning Electron Microscopy [98]

In the electron gun, cathodic electrons are accelerated to 1–50 keV energies by the anode. The first electronic lenses are called condensers, and they focus on the electron beam that has been deflected by the scan coils, which supply a magnetic field. The objective lens focuses the electron beam down to a point (1-5 nm) and scans raster-wise across the surface of the sample. Backscattered electrons, characteristic of the type of atom forming the structure, and primary electrons transmitted through the sample build the image when together with the radiation from the secondary electrons being emitted when primary electrons interact with sample atoms. Moreover, backscattered electrons are registered to give images, flagging regions with different chemical composition [96].

3.10.2 Scanning Electron Microscopy

The SEM is a high-energy electron microscope that generates surface images using a rectangular raster pattern. It is a multi-functional tool, imaging different materials and biological samples. Electron microscopes can reach magnifications as high as 100,000X, far beyond the 2,000X limit of traditional light microscopy [99]. SEM is incomparable for depth of field, keeping three-dimensional objects clear and providing. In the standard SEM, the electron beam is generated from a tungsten filament cathode in an electron gun. The common alternative cathodes are lanthanum hexaboride and improved cold-cathode guns. Condenser lenses focus the electron beam (from several 100 eV to 40 keV) to prepare a spot with a size (0.4-5nm). Using either scanning coils or deflector plates, the beam traverses the electron column to scan the surface of the specimen within a rectangle aligned with the surface. It is dependent on the landing force, atomic number, and specimen density. High-energy electrons indicated tensile strength, while inelastic scattering produces secondary electrons (high-energy, low-energy) and electromagnetic radiation, with specialized instruments detecting these [100]. The sample can absorb beam current, providing a 0D view of current distribution. The signal strength distribution is revealed by the microscope beam scanning the specimen line by line. The image, originally captured on a cathode ray tube, is stored digitally and displayed on the computer before being archived. High-resolution surface morphology of nanostructures was obtained at a secondary electron image resolution of 1.0 nm at 15 kV using a JEOL JSM-7600F FEG-SEM. The r-filter on this microscope allows secondary electron and backscattered electron pictures to merge. It also implements a gentle beam mode that minimizes beam damage and charge damage, enabling imaging of charged samples without the need for extra coating in the process [101].

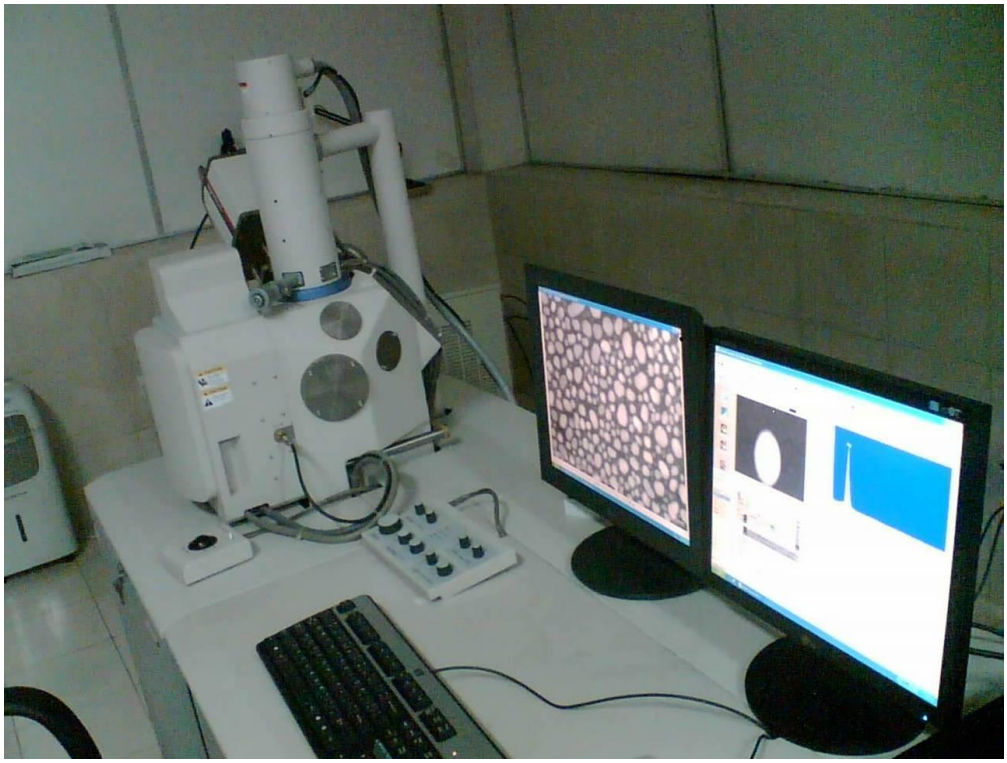

Figure 3.4: Photographs of SEM (Hitachi, S-3400N) and EDX (Thermo, Ultradry) equipment located at IPD, BCSIR

3.11 Elemental Analysis

The use of Energy Dispersive X-ray spectroscopy (EDX) is essential for analysing thin films by examining the energy dispersive spectrum. This allows for the determination of net counts, net weight percentage, and elemental percentages. Details of the constituents in the thin film can be found in the EDX table [102].

3.11.1 Energy Dispersive Analysis of X-rays

Energy Dispersive Spectroscopy (EDS) is an investigative tool for obtaining the elemental composition of a specimen. This spectroscopic method uses electromagnetic radiation to study interactions with matter, specifically by detecting the characteristic X-rays emitted when charged particles hit the sample. Its description depends on the fact that every component has an individual atomic architecture, enabling the recognition of X-rays specific to the element. A beam of high-energy electrons is targeted at the specimen in question to emit characteristic

X-rays [103]. The ground-state electrons of a resting atom are bound to the nucleus in many levels of energy or electron shells. When an incident beam stimulates an inner shell electron, it gets ejected, leaving an electron vacancy that is filled later by an electron from a higher-energy shell, resulting in energy emission at around the X-ray range. EDS measures the quantity and energy of the emitted X-rays from a sample [104].

3.12 Optical Measurement of the Thin Films

The three phenomena, namely transmission, reflection and absorption, investigate the optical behaviours of a semiconductor. When a photon hits a semiconductor's surface, certain photons are reflected, others are absorbed, and the remaining ones enter the semiconductor and might be restructured. To determine the band gap optical properties of thin films, the transmission and absorption characteristics of the created samples are analysed. This is accomplished by utilising an Ultraviolet-visible spectroscopy instrument [105]. By examining these characteristics, additional optical parameters of the thin films can also be established.

3.12.1 Ultraviolet–Visible Spectroscopy

The UV-visible spectrophotometer measures of absorption or reflectance in the UV-visible spectrum. It works with light from the visible, near-UV and near-infrared regions. The colour of materials is dependent on their absorption or reflectance in the visible spectrum. This gives us a tool to analyse the optical properties of materials. Electronic transitions happen in this part of the electromagnetic spectrum. Absorption spectroscopy detects transitions from the excited state to the ground state, whereas fluorescence spectroscopy detects the opposite transitions [106].

Figure 3.5: Photographs of Ultraviolet–Visible Spectrometer (Shimadzu, UV-2600+) IPD, BCSIR, Dhaka.

3.12.2 Absorption

Absorption of electromagnetic radiation is the transfer of energy from a photon to matter, most often an electron in an atom. This results in the conversion of electromagnetic [109] energy to different forms of energy, namely thermal energy, etc. Attenuation is defined as the reduction in light intensity from the propagation of waves. Most of the wave absorption happens regardless of intensity, but in some cases, the transparency of the medium varies depending on the wave's intensity passing through it.

3.12.3 Absorption Coefficient

When a photon strikes the interface of a semiconductor, a portion is reflected, another portion is absorbed, and the remaining photons pass into the semiconductor. Materials absorb radiation through the excitation of electrons and photons. In semiconductors, various types of absorption can occur.

- The changes in electronics span several energy levels.
- Changes in electronics fall within a similar energy band.
- The electronic changes feature customised to indicate impurity atoms.
- Lattice vibrations are another form of absorption.
- Vibrations of impurity atoms can also contribute to absorption.

In the transmission (T) of the elementary absorption area is given by [110]

$$T = A \exp\left(-\frac{4\pi k}{\lambda}\right)$$

Where A is constant, k is the extinction coefficient, and t is the width. For $K_2 << n_2$, the primary variance of T originates from the pre-exponential and exponential A. Therefore,

$$T \sim \exp(-\alpha t)$$

Where $\alpha = 4\pi k/\lambda$ represents the film's absorption coefficient. Therefore, the absorption coefficient value can be determined from the relationship [111].

$$\alpha = -\frac{In\, T}{t}$$

3.12.4 Band Gap

A band gap is an energy range devoid of electron states in insulators and semiconductors. This quantity is the energy difference between the top of the valence band and the bottom of the conduction band. This energy produces the minimum energy necessary to free any one external shell electron from the orbits around the nucleus, where they are trapped, so that they can freely travel through the solid matter. Two types of band gaps are commonly found in the field of semiconductor physics, namely, Direct and Indirect band gaps. In this paradigm, a unique k-vector in the Brillouin zone demarcates the lowest-energy state in the conduction band and the highest-energy state in the valence band [112]. When the k-vectors overlap with one the other, then we have a "direct gap". The unique components in K-vectors characterise the interaction among electrons, holes, phonons, photons, and other particles that conserve momentum and energy in crystals. where a photon at the semiconductor band gap shows low migration, and the movement of the electron from the conduction band releases the excess

energy of the photon. In direct band gap semiconductors, the electron occupies the conduction band minimum, while the hole is at the valence band maximum. However, crystal momentum is disrupted, and the condition for attaining an indirect band gap cannot be met. For radiative recombination to take place, indirect band gap materials require mediation with phonons in the form of their absorption or emission. The momentum of a phonon is the difference in momentum between electrons and holes. It could alternatively concern a crystallographic defect, which serves a similar purpose. The process involves phonons, so one would expect that to happen at a much faster rate over a given timescale, explaining why radiation recombination is much lower in the case of indirect band gap materials [47]. As a result, materials with a direct band gap are widely preferred over indirect band gap structures, such as silicon, in light-emitting diodes and laser diodes. Due to the slow nature of the recombination rate in indirect band gap materials, radiative recombination is usually a small part of the overall recombination events in many conditions. Perhaps as phonons are involved, this mechanism would happen at a much faster rate if needed; therefore, radiative recombination in indirect band gap materials is significantly slower than that of direct band gap materials. This can be done by introducing a displacement circle inside the material. Due to the split above and below this "dislocation disk", surfaces on the periphery of the loop experience separation, inducing an oppressive pressure that raises the conduction band energy, preventing the passage of electrons. In the case where the neighbouring region close to the displacement loop area does not have disorders (implying the absence of non-radiative recombination), the electrons will undergo a process called radiative recombination and return to the valence shell. So captures Run-of-the-mill "DELEDs"(Dislocation Engineered Light Emitting Diodes) [113].

3.13 Film Deposition Technique

Thin-film deposition is the process of placing a thin coating on a surface. The deposition refers to any method for depositing a thin film of material on a substrate. There are mainly two types of deposition process. It is discussed below:

3.13.1 Physical Vapor Deposition

Physical vapor deposition (PVD) is an evaporation coating process in which material is transferred at an atomic level. It serves as a non-electroplating alternative to electroplating. The material is deposited in a controlled manner onto a substrate in a specific order. It covers procedures such as Sputtering Coating (SC), Pulsed Laser Deposition (PLD), and Cathodic Arc Deposition (CAD).

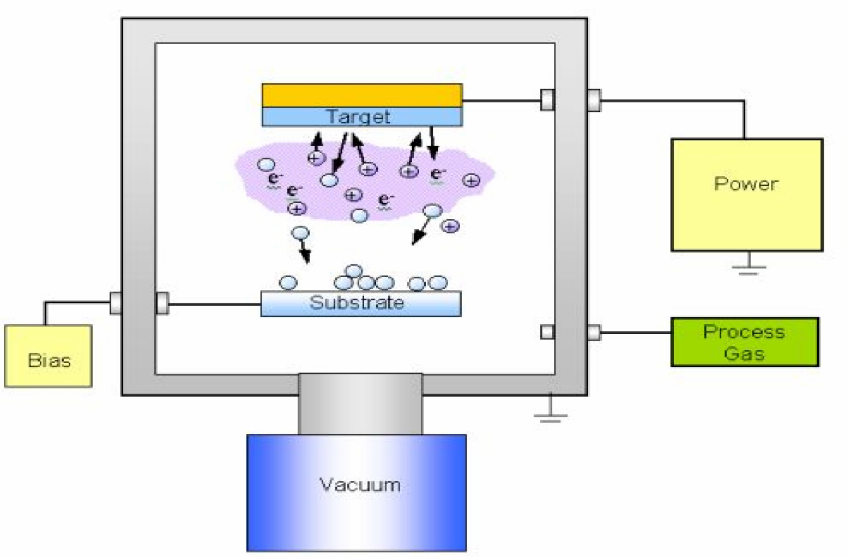

Figure 3.6: Schematic diagram of physical vapor deposition technique [127].

PVD has numerous advantages. It permits the use of inorganic materials and certain organic ones. It is eco-friendly than electroplating. Nonetheless, it also carries certain drawbacks. It is a direct-visibility process, which complicates the coating of undercuts and comparable

attributes. A significant capital cost is associated, and high vacuums and temperatures are required in some processes, necessitating skilled operators. In addition, PVD coating deposition is usually a low-rate process.

3.13.2 Chemical Vapor Deposition

Chemical Vapor Deposition (CVD) is an advanced process that enables the formation of solid materials from a vapor phase. It shows many similarities to physical vapor deposition (PVD) in various aspects. In the PVD process, solid precursors are vaporized from a specific target and then deposited onto the substrate surface. Among the process, CVD is considered one of the most effective techniques for depositing thin films. It is used to deposit solid crystalline or amorphous films and coatings on a wide range of metals, semiconductors, and compounds.

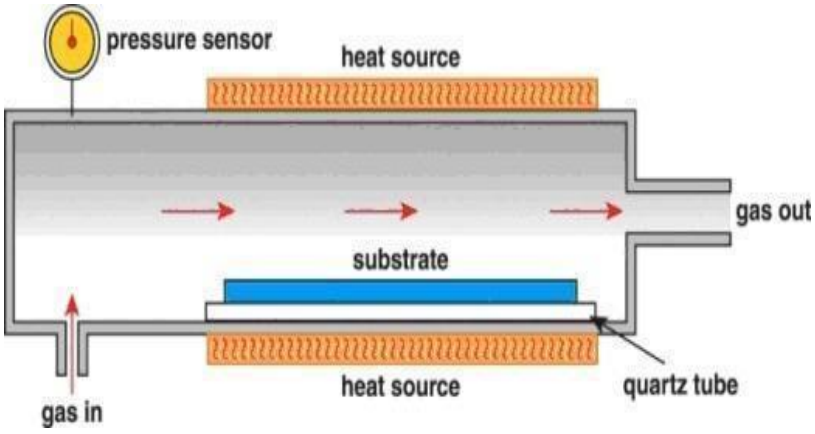

Figure 3.7: Schematic of chemical vapor deposition technique [128]

These films and coatings are of high purity and exhibit excellent properties. CVD is a method used to create thin coatings by reacting gaseous precursors. Thermal or electric discharge plasma therapy initiates the activation of the chemical reaction. As the unstable component exits the reaction chamber, the target element or compound condenses and reacts on the substrate surface. The temperature should be between 350 ^{0}C and 1100 ^{0}C. Particles are formed

as a result of chemical events occurring in the gas phase (powder formation). The deposition may take place in a vacuum under normal or high pressure. All pressures smaller than ambient are considered “in vacuum”. Plasma instigation has the benefit of lowering response temperatures dramatically. The energy of the particles is extremely low. The film development is minimally influenced by the reactants.

3.13.3 Chemical Bath Deposition

The chemical Bath Deposition technique involves the controlled release of material from a solution onto a prepared surface. This method offers several advantages over advanced vapor phase technologies, such as spray pyrolysis, CVD, and MBE. The CBD of sulfide techniques involves an alkaline environment that includes metal ions, a chalcogenide source, and an additional base. The chelating agent is used to inhibit metal ion hydrolysis and maintain the bath's stability, which would otherwise quickly hydrolyze and form precipitates. The varied reaction occurring on the surface is restricted by two primary elements: backward homogeneous solution reactions and the buildup on the reactor wall for CBD material.

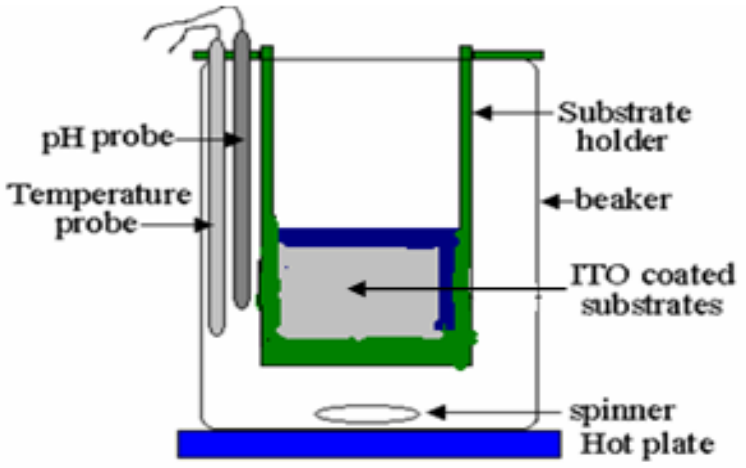

Figure 3.8: Schematic of chemical bath deposition technique [129]

Deposition occurs in a beaker containing deionized (DI) water, which is warmed to 85-90°C. Chemicals are introduced sequentially, leading to material deposition on all surfaces in the bath, including the ITO-coated glass surfaces. Generally, a thickness of 800-1000 nm can be

achieved in a 20-minute session. The layer that has been deposited is typically annealed before the addition of another layer. Molecular beam epitaxy (MBE) is an alternative deposition technique.

3.13.4 Sol-Gel Process

In the production of sol-gel thin films, inorganic precursors accumulate on the substrate surface via a method that includes gravity extraction, drying, and condensation [130]. Precursor dimensions, configuration, condensation and evaporation rates, capillary pressure, and extraction velocity determine the film size. These factors also influence film structure. It is a low-cost and straightforward method for producing a suspension of colloidal oxides. Thus, these suspensions can be converted into various solid forms, such as powders, fibers, or films. The working principle of the sol-gel method is mainly based on the hydrolysis and condensation reactions. The coating process enables the use of different oxide materials together, resulting in a variety of ceramic types. Modern ceramic and system technology necessitates high purity in nano-materials. They also facilitate simple composition and management of structure. One of the more intriguing approaches is sol-gel coating, which offers several advantages. The addition of organic or inorganic salts can promote microstructural tuning and property enhancement in oxide films.

3.13.5 Spray Pyrolysis

Spray pyrolysis represents a method that employs a liquid precursor for the deposition of thin films [131]. The heat produced by the substrate is critical in the formation of the film. When the temperature of the layer is less than 200°C, the spray slipping for the substrate undergoes partial breakdown (oxidation), resulting in a hazy film with poor transparency and inadequate electrical conductivity.

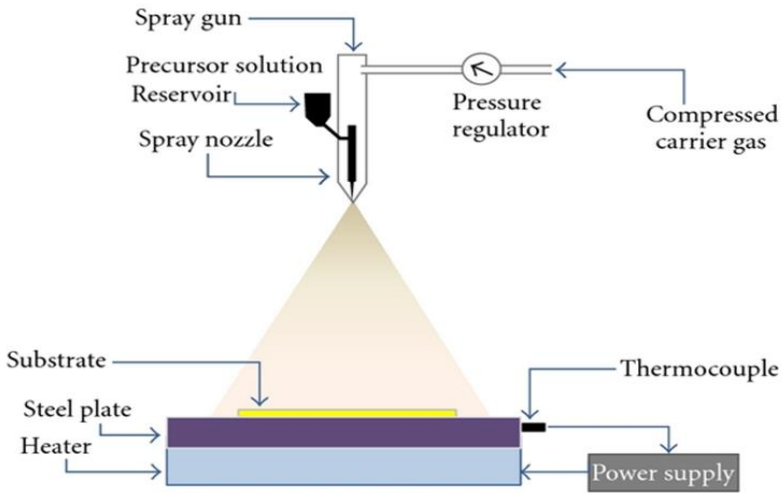

Figure 3.9: Schematic of spray pyrolysis technique [132]

If the substrate temperature is excessive (> 500°C), the spray vaporizes before contacting the substrate, resulting in a powdery layer. The devices generally consist of an atomizer, a precursor liquid, a substrate heater, and a temperature regulator. It often employs an air blast, in which the liquid is exposed to a flow of air. It additionally utilizes ultrasonic atomizers that produce short wavelengths for precise atomization. Electrostatic atomizers subject the liquid to a strong electric field.

3.14 Photoluminescence

Photoluminescence (PL) spectroscopy is a valuable, non-destructive analytical technique used to investigate the electronic and optical properties of materials, particularly semiconductors, nanomaterials, and organic compounds. By analyzing the light emitted after the absorption of photons, PL spectroscopy provides essential insights into the energy band structure, recombination processes, and defects within materials.

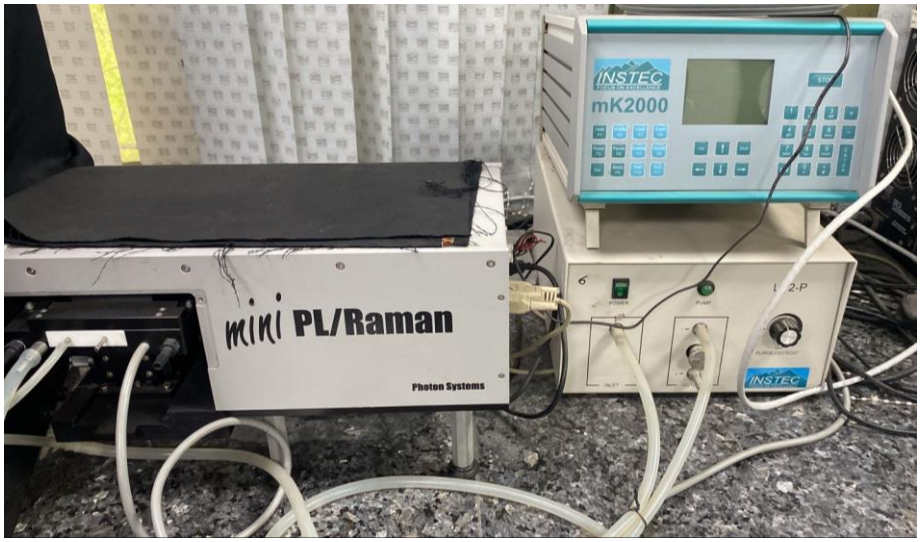

Figure 3.10: A photograph of the Photoluminescence setup (PHOTON SYSTEM) with (HeAg 30 Deep UV laser) as excitation source varying temperature facilities (CARF, BCSIR)

3.14.1 Principle of Photoluminescence:

PL is a widely used technique for studying the optical properties of semiconductor materials, nanostructures, and other optically active materials [146]. It involves the emission of light from a material after it absorbs photons, exciting electrons to higher energy levels. As these energetically excited electrons return to their original position, light energy is emitted. The energy of this light is used to probe the electronic structure of the material. This step is important to investigate the band gap and energy level of the material.

3.14.2 Significance of Photoluminescence in Material Science

PL is an important diagnosis method in material science and semiconductor physics. The subject material is exposed to light of a specific wavelength, often UV or visible. These photons have an energy, that causes those electrons in the valence band to jump to the conduction band, (creating a hole and an electron) by overcoming the band gap in the exciton. When the charge carriers (electrons and holes) combine, photons are emitted. The wavelength of this emitted light is a key characteristic of the material's electronic structure, offering valuable information about its band gap and overall properties.

3.14.3 Applications of Photoluminescence Spectroscopy

Photoluminescence (PL) spectroscopy, which is widely used for research as well as for industry [148]:

I. Material characterization:

PL spectroscopy is widely adopted to probe the optical and electronic properties of semiconductors, nanoscale materials, quantum dots, thin lms, etc. This method is useful for determination of quality, purity and homogeneity of the material.

II. Defect Characterization:

The technique is defect sensitive, and is able to detect dislocations, defects and impurities in materials. Information regarding the nature and concentration of defects can be obtained from the particular emission wavelengths of light emitted due to such defects.

III. Band Gap Estimation:

The photons emitted are directly related to the band gap energy of the material. It is widely applied in accurately determining the band gap of semiconductors and related materials by measuring the PL.

IV. Nanomaterials:

A particular strength of PL spectroscopy is found in its ability to study size-dependent optical properties of nanomaterials, including quantum dots and graphene and unique emission characteristics.

3.15 Electrical Measurement of Thin Film

Thin films are films of material deposited as the result of a surface technique such as sputter deposition. These are to be distinguished from the bulk material in both their electronic behaviour and physical structure. Study of electrical properties of thin films is important in many applications such as semiconductors, solar cells, sensors, and coatings. The electrical behavior of thin films is a multifaceted, complex phenomenon which depends on a number of parameters such as film thickness, composition, defects and substrate [143].

3.15.1 Affecting the Electrical Properties of Thin Films

Affecting the electrical properties of thin films is discussed below:

3.15.1.1 Film Thickness

When film is thin enough, its quantum effect will be highlighted, resulting in changes in electrical properties compared with those of bulk material. For example, a thin film may have higher resistivity due to the enhanced electron scattering at surfaces and interfaces.

3.15.1.2 Grain Boundaries and Defects

In polycrystalline thin films, the grain boundaries are believed to behave as charge transport barriers, leading to decreased conductivity. Defects, dislocations, and voids may also influence electrical behaviour, frequently resulting in localized high-resistance areas or leakage currents.

3.15.1.3 Substrate Material

The substrate on which they are fabricated dramatically affects the electrical characteristics of thin films. The thermal expansion coefficient, electrical conductivity and surface roughness of the substrate, for instance, can influence the growth of the film and the electrical properties thereof.

3.15.1.4 Temperature

The electrical response of thin film is very sensitive to temperature. A potential source of increased resistivity is the greater phonon scattering at high temperatures. Furthermore, variation in temperature has an effect on both carrier concentration as well as mobility, which influence the performance of the device in thin films.

3.15.2 Electrical Resistivity of Thin Film

Resistivity is the reciprocal of conductivity and describes the degree to which a material opposes the flow of an electric current. Resistivity in thin films may be different from that in bulk due to surface scattering, grain boundary scattering and quantum size effects, especially for very thin films. Resistivity is commonly measured using techniques like the four-point probe method, which helps minimize contact resistance.

3.15.3 Electrical Conductivity of Thin Film

Electrical conductivity is considered a fundamental property that indicates how easily electrons can move through a material. A range of conductivity behaviors can be exhibited by thin films, from metallic (high conductivity) to insulating (low conductivity), and even semiconducting characteristics may be displayed under certain conditions. The conductivity is influenced by factors such as the material's crystal structure, defects, and the quality of the film deposition process.

3.15.4 Electrical Analysis Process of Thin Film

The thin film's electrical characterisation [114], e.g. resistivity (ρ), conductivity (σ), sheet resistance (Rs), activation energy (Ea) are related to the electrical characteristics of the synthesised sample [115]. Resistance is defined as the material property which slows down the flow of electric current, and the resistance associated with a unit cross-sectional area of material is called resistivity. It is expressed mathematically as

$$\rho = \frac{RL}{A}$$

Here, A is the cross-sectional area, material length L, and R is the resistance along the direction of the flow of electric current. Resistivity is an inherent characteristic of a substance, and it's affected by the arrangement of its crystallites. Definition of Electrical Conductivity of material is the inverse of resistivity shown by that material. Denoted by σ, is expressed as

$$\sigma = \frac{1}{\rho}$$

The conductivity of a material depends only on its structural and physical properties [15].

3.15.5 Resistivity Measured by Four-Point Collinear Probe Method

The electrical resistivity of a material is determined by using a 4-point collinear probe. The schematic arrangement of the four-point probe method is shown in Figure 3.6. The four-probe resistivity technique consists of four thin parallel tungsten wire probes that are brought into contact with the sample surface under test. A constant current source is used to drive current (I) between the outer probes, while the voltage (V) is measured between the two inner probes [15]. The electric current flowing through the outer probes sets up an electric field in the sample. The potential difference between the inner probes is measured. Separate probes for current and voltage are used to eliminate the constant resistance between the electrodes and the material.

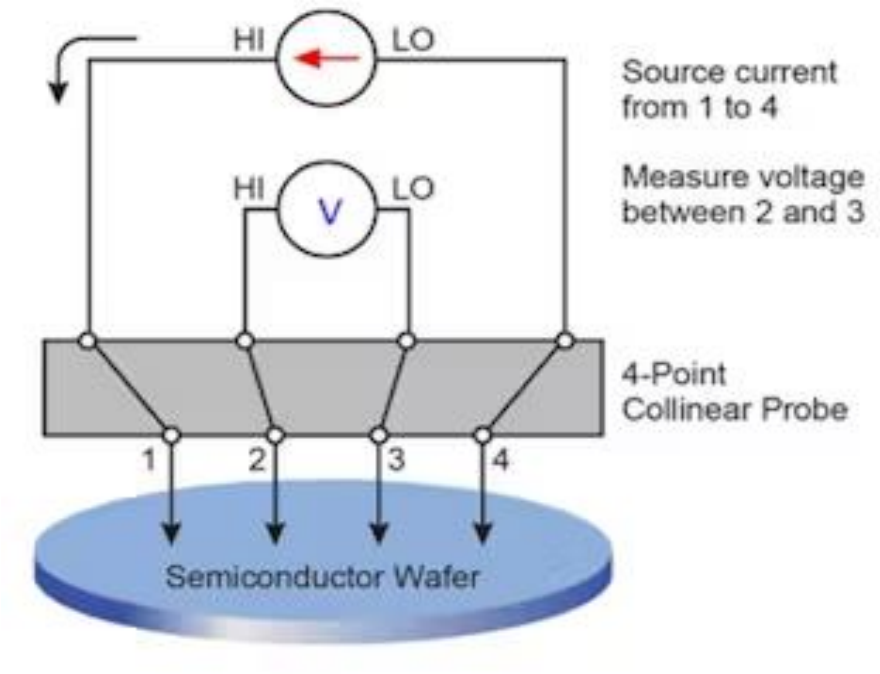

Figure 3.11: Schematic diagram of a typical Four-point collinear probe for measuring sheet resistance of thin films [116].

From the four-point probe method, sheet resistance can be determined as

$$R_{sh} = K\frac{V}{I}$$

Where, K is the constant, V is the voltage, I is the electric current, and R_{sh} is the sheet resistance of the sample. We calculated the sheet resistance by multiplying the geometrical correction factor (fi) (Farhad et al). So, after simplifying the above equation, we finally calculated the sheet resistance from the following equation:

$$R_{sh} = 4.53 \times f_1 \times R_{4pp}$$

where,f_1 is the geometrical correction factor that depends on the geometry of the substrate. R_{4pp} is the 4-point probe resistance determined by using ohm's law.

Figure 3.12: A photograph of the Homebuilt four-point collinear probe coupled with a Keithley SMU 2400 (IPD, BCSIR)

Chapter 4: Fabrication and Experimental Details

4.1 Introduction

This chapter provides a comprehensive summary of the properties, structural features, and syntheses of Aluminum (Al) doped ZnO, an essential material for today's advanced electronics, optoelectronics, and nanotechnology. This features the main physical and chemical properties of ZnO, with reference to its crystal structure, stability and optical properties, which are used for applications as coatings, sensors and thin films. The chapter also covers the fundamental properties of aluminum, including its abundance and importance in the field of materials science. Moreover, it discusses the chemical synthetic approach and thin-film deposition techniques for high-quality ZnO-based nanostructures, such as chemical bath deposition, sol-gel, spray pyrolysis, and spin coating. Finally, it investigates ZnO nanorods grown hydrothermally on seed layers.

4.2 Properties of Zinc Oxide

Zinc oxide (ZnO) has been the subject of comprehensive investigation since the year 1935 [117]. Devices based on zinc oxide (ZnO) are prevalent in modern technological applications related to electronics and optoelectronics. This compound is a good coating material and is also employed in pressure measurement instruments. Additionally, a multitude of other applications for ZnO exist, thereby establishing it as a significant area of academic inquiry. It has been widely studied within the scientific research community due to its stability and safety when subjected to high temperatures. It exhibits diverse chemical properties, allowing for various wet etching methods. An overview of several important properties is given in Table 4.1 [119,120].

Table 4.1 Elementary Properties of ZnO

Name of the property	**Value / Type**
Molecular Formula	ZnO
Crystal Structure	Wurtzite
Type of materials	Group II-VI Semiconductor
Molar Mass	81.408 g/mole
Appearance	White Solid
Odor	Odor less
Density	5.606g/cm^3
Melting Point	1975 ^{0}C (decompose)
Boiling Point	2360 ^{0}C (decompose)
Water Solubility	Insoluble
Band Gap (Room Temperature)	3.37 eV (direct)
Exciting Binding energy (Room Temperature)	60 meV
Dielectric constant	8.5
Refractive Index	2.0041

Moreover, it has demonstrated radiation resistance, biological compatibility, and minimal power requirements for optical excitation. When integrated, these characteristics are regarded as the most optimal selection for widely technological devices [118]. ZnO has a wide band gap of 3.37 eV and an exciton binding energy of 60 meV. It is non-toxic and stable form at room temperature. ZnO can be grown into a single-crystal substrate [121].

All these properties of ZnO make it a unique candidate for a variety of devices. Its applications are extended from display systems to sensing apparatuses and ultraviolet laser diodes. Further new uses for Zinc oxide and its alloys may be discovered through in-depth research.

4.2.1 Structure of Zinc Oxide

There are two primary crystal forms of ZnO: the cohesive hexagonal wurtzite and the cohesive cubic zincblende. The most thermodynamically stable structure at ambient conditions is the wurtzite structure, which is more abundant in observation. The zinc blend phase can be produced by growing on cubic lattice substrates. For both cases, Zn and O atoms form a tetrahedron. In the wurtzite structure, the Zn^{2+} ions are surrounded by four O^{2-} ions in a tetrahedral geometry, and similarly, each O^{2-} ion is surrounded by four Zn^{2+} ions [122]. At elevated pressures, around 10 GPa, ZnO undergoes a structural transformation to a rock salt structure. Both hexagonal and zincblende structures were found to lack inversion symmetry. The way the lattice is arranged causes both hexagonal and zinc-blend ZnO to exhibit the piezoelectric effect, and hexagonal ZnO also shows pyroelectricity. Lattice parameters are a = 3.25 Å and c = 5.2 Å then c/a = ∼1.6, close to the optimal hexagonal cell ratio of c/a = 1.633 [123]. It mainly has ionic bonds because of the connection between Zn^{2+} and O^{2-}, which is typical for many group II-VI compounds. The ionic radius of Zn^{2+} here is 0.074 nm, whereas for O^{2-} it is approximately. 0.140 nm [123].

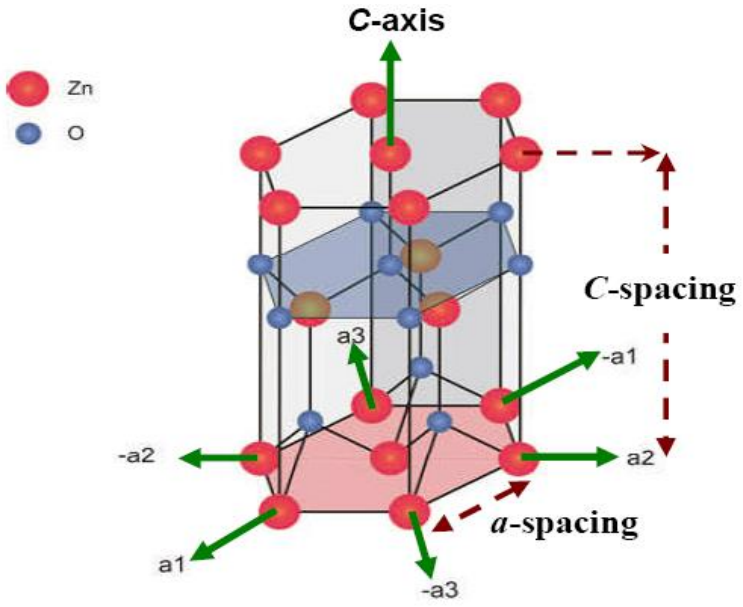

Figure 4.1: Wurtzite structure of bulk ZnO. Zn atom is denoted by red colour and the O is in blue [124].

This feature describes why wurtzite grows better than the zinc blende structure and highlights the impressive piezoelectric properties of ZnO [125]. The polarised Zn-O bonds cause the Zn and O planes to carry electric charges as shown in Figure 4.1. In Wurtzite, the nearest neighbors count is four. Four Zn (or O) ions surround each O (or Zn) ion tetrahedrally. Every ion also features twelve similarly typed next-nearest neighbors. The distance between O and Zn for the closest neighbors is 1.973 Å in the other three directions of the tetrahedral configuration [122] and 1.992 Å along the hexagonal c-axis. Tetrahedral coordination suggests a covalent bond between atoms. They have covalent radii of 1.31 Å for Zn and 0.66 Å for O. It is an isotropic crystal that belongs to the C6v point group. The hexagonal wurtzite structure has C6v symmetry, comprising rotations of ±60°, ±120°, and 180° (along the c-axis), and two sets of three mirror planes that are coincident with the hexagonal axis. A single-crystal wurtzite ZnO has twelve phonon modes, corresponding to four atoms per unit cell [124]. Evaluating the thermal, electrical, and optical characteristics of the crystal calls for knowledge of phonon modes. ZnO's phonon modes have been investigated exhaustively and predicted.

4.3 Properties of Aluminium

Aluminium is abbreviated as Al and has an atomic number of 13. Being the third most abundant element on Earth of the earth. It is only twice as plentiful as copper because copper is scarce in the mantle and core [126]. It is extracted from bauxite ore, but due to its high reactivity, the natural form and the high number of ore that is the target for extraction are rare and usually found only as ores under extreme reducing conditions. Bauxite is found in more than 270 minerals. Moreover, it is characterized by its relatively low density and excellent electrical conductivity, which gives it outstanding corrosion resistance. Its alloy plays a crucial role in the aerospace, transportation, and construction industries. The most useful component of aluminum are oxides and sulfate.

Table: 4.2. Basic Properties of Al [126]

Property Name	Value/type
Molecular Formula	Al
Atomic Mass	26.98
Odor	Odor less
Melting Point	660.32 C
Boiling point	2470 C
Appearance	Salivary grey metallic

4.4 Preparation of Stock Solution

Zinc acetate dihydrate ($Zn(CH_3COO)_2 \cdot 2H_2O$, Scharlau) and aluminium chloride hexahydrate ($AlCl_3 \cdot 6H_2O$, Sigma-Aldrich) were used as the source materials for Zn and Al precursors, respectively. An alcoholic medium, such as ethanol, was employed as the solvent,

and monoethanolamine (C_2H_7NO) (MEA) was used as the sol stabilizer. A stock solution was prepared by dissolving zinc acetate dihydrate in absolute ethanol (Sigma-Aldrich). The resulting solution was stirred with a magnetic stirrer at 60°C for one hour. Subsequently, 60 µL of 0.02 M MEA was added drop by drop until a transparent and homogeneous mixture was obtained. For Al doping, aluminum chloride hexahydrate ($AlCl_3 \cdot 6H_2O$, Sigma-Aldrich) was introduced into the prepared stock solution and stirred continuously for one hour at concentration variations of 2%, 3%, 5%, and 8 mol%. The resulting solution is used for the spin-coating of substrates. In this investigation, AZO thin films were deposited on soda-lime glass (SLG). Before the deposition, the glass layers were ultrasonically cleaned with acetone, isopropanol, and deionised water (resistivity ~ 18 Ohms-cm) for 15 min, then air-dried.

Table 4.3: Necessary Materials and Deposition Conditions for AZO Seed Layer

Precursors	Zinc acetate dihydrate [$Zn(CH_3COO)_2.2H_2O$] Aluminium chloride hexahydrate [$AlCl_3.6H_2O$]
Solvent	Ethanol
Stabilizer	Monoethanolamine (MEA)
Deposition temperature	Room temperature
Concentration of Zinc Acetate Dihydrate [$Zn(CH_3COO)_2.2H_2O$]	0.02M
Doping Percentage of Al	2,3,5 and 8 mol%
Rotation speed of the spin coater	500 rpm for 5 sec, 2500 rpm for 20 sec
Precursor solution	30 µL for each layer

4.5 Spin Coating

Spin coating is a commonly used technique for deposition, particularly in laboratory-scale research. The process involves applying a precursor solution containing salts onto a substrate. This substrate is then rotated at high speeds to achieve an even distribution of the solution. After this, the films undergo annealing to remove solvents and facilitate phase crystallization.

4.5.1 Spin-Coating Method

This method is simple and cost-effective, especially for small-scale experiments. It allows for precise control over the film's thickness by adjusting parameters like spin speed and solution concentration. However, spin coating has significant drawbacks, including high material waste, as a large portion of the precursor solution is lost during the process. Additionally, its scalability is limited, which makes it unsuitable for large-area applications.

4.5.2 Spin Coating Process

This process typically consists of four distinct stages, as shown in Figure 4.6, each crucial for determining the final properties of the film, including thickness, uniformity, and morphology [133]. The first stage is deposition, during which a precise amount of solution is dispensed into the center of the substrate using a micro-pipette. Secondly, in the acceleration stage, after the solution is dispersed, the substrate is accelerated to the desired final speed. Due to the dominant centrifugal force, the films begin to thin rapidly as the solution flows outwards from the center of the substrate. In the third stage, the process achieves the desired film thickness and uniformity. At high speeds, most of the solution is expelled from the substrate, resulting in thinner films. The solvent evaporates quickly during this stage, leading to the solidification of the film. Finally, the film is formed on the substrate, and deionized water is used to rinse the substrate, removing any excess precursor solution.

4.5. 3 Why Spin Coating

In this chapter, we have thoroughly discussed a range of deposition methodologies. Based on this study, the spin coating technique is favoured above all alternative deposition methods due to its simplicity, cost effectiveness, consistent film quality, thickness control, and minimal equipment expenses. Consequently, spin coating is employed in the fabrication of AZO seed thin films.

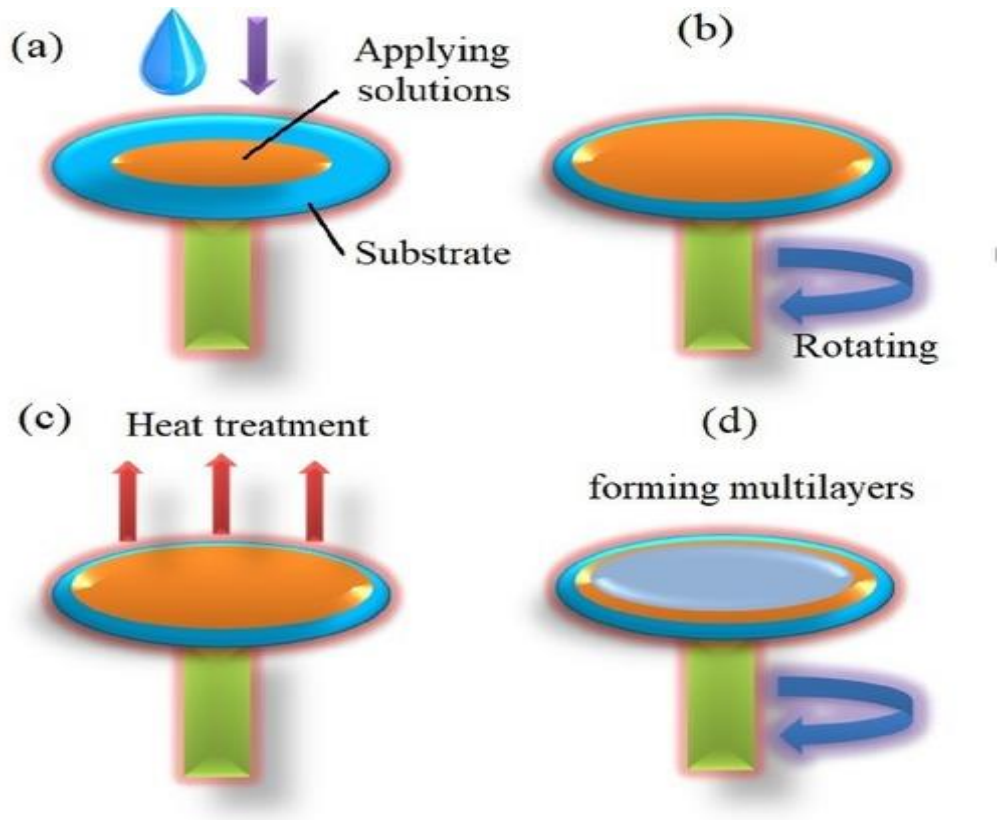

Figure 4.2: Schematic of spin coating steps(a) applying solution on substrate stage (b) accelerated (rotating) stage (c) evaporation stage, and (d) film formation stage deposition [134].

4.6 Growth of Seeding Layer

Seeding layer growth refers to the deposition of a thin layer of material onto a substrate to facilitate the development of subsequent layers in thin-film deposition, particularly in semiconductor or nanotechnology applications. This layer typically serves as a foundation or

"seed" that promotes the uniform growth of the desired material [136]. It can direct the orientation of crystals in the growing material, resulting in desirable properties such as improved conductivity or mechanical strength. Seeding layers improve the adhesion between the substrate and the ever-increasing material. It enables better control over the growth process, which is particularly important in applications such as electronics, photovoltaics, or coatings. This layer serves as the nucleation center on the substrate, enabling the growth of Nano Road and controlling the vertical alignment of rods relative to the substrate [136]. Various techniques have been employed for cultivating seeding layers. The properties of the seeding layer significantly affect the morphology of the subsequently grown nanorods (NRs). These include magnetron sputtering [137], Pulsed Laser Deposition (PLD) [138], sol-gel methods [139], spray pyrolysis [140], and electrodeposition [141].

4.6.1 Preparation of AZO Seeding Layer

The soda-lime glass (SLG) microscope slide was cut into 2 cm × 1 cm strips and then washed with acetone, isopropanol, and deionized (DI) water (resistance ~18 ohms-cm) for 15 minutes each, followed by air-drying. Toluene was also used previously on SLG substrates before soaking in acetone. The molar concentrations of 0.02M zinc acetate dihydrate (ZAD) were dissolved in absolutely ethanol for the deposition of AZO seed layers. The similar method was used by Farhad et al [142,143].

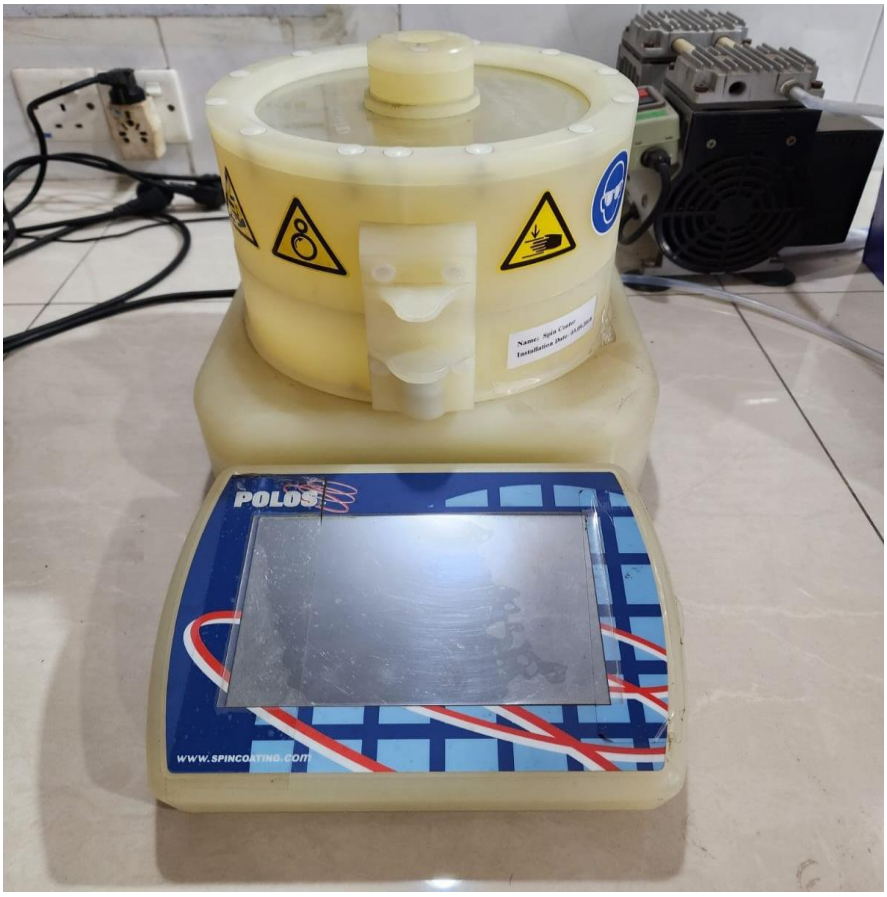

*Figure 4.3: A photograph of the Spin coater (*Model POLOS SPIN150i*, IPD, BCSIR) used in this study to grow AZO seed layers.*

For the deposition of AZO films on soda-lime glass (SLG) substrates, spin coating was used in two steps: the first at a rate of 500 rpm for 5 seconds and the second at 2500 rpm for 20 seconds. To add to the film thickness, this process was repeated 20 times. The films' substrates were annealed in air at 250°C for 1 hour at a heating rate of 5°C/min and then allowed to cool to room temperature.

4.7 Hydrothermal Growth Mechanism for ZnO Nanorods.

The hydrothermal synthesis of ZnO nanorods has been extensively explored by several researchers. Vayssieries was the first to report the hydrothermal synthesis of ZnO microrod arrays, which complemented the colloidal particle synthesis previously described by Andres-Vergés et al. In Vayssieries' method, zinc nitrate (ZN) and hexamethylenetetramine (HMT) were mixed in an equimolar solution and heated to 90°C to facilitate the growth of nanorods (NRs). This method has since become one of the most widely studied and successful approaches for ZnO nanorod growth from solution [144]. HMT has also been used to produced good quiet nano reported. When zinc nitrate and HMT are mixed in an aqueous solution, synergistic effects are often observed. Zinc ions are provided by zinc nitrate, while HMT serves as a reducing agent, controlling the crystal growth of ZnO. ZnO nanorods may be synthesized through the subsequent chemical reaction [145].

1) $Zn(NO_3)_2 \rightarrow Zn^{2+} + 2NO_3$
2) $C_6H_{12}N_4 + 6H_2O \rightarrow 4NH_3 + 6CH_2O$
3) $Zn^{2+} + 2OH^- \rightarrow Zn(OH)_2$
4) $Zn(OH)_2 \rightarrow ZnO + H_2O$

This process provides a relatively simple and cost-effective method for producing high-quality ZnO nanorods with controlled sizes and shapes, which have numerous applications in electronics, photovoltaics, sensors, and optical devices.

4.7.1 Preparation of ZnO NRs on AZO Seed Layers by the Hydrothermal Method

Individual 0.1M aqueous arrangements of ZNH and HMT were arranged in DI water and then consolidated in a Schott bottle. On a clean microscope glass slide, PTFE thread tape was applied to join a naked and a seeded substrate [29]. This microscope glass slide was quickly submerged in the solution, with substrates inclined toward the bottom of the bottle.

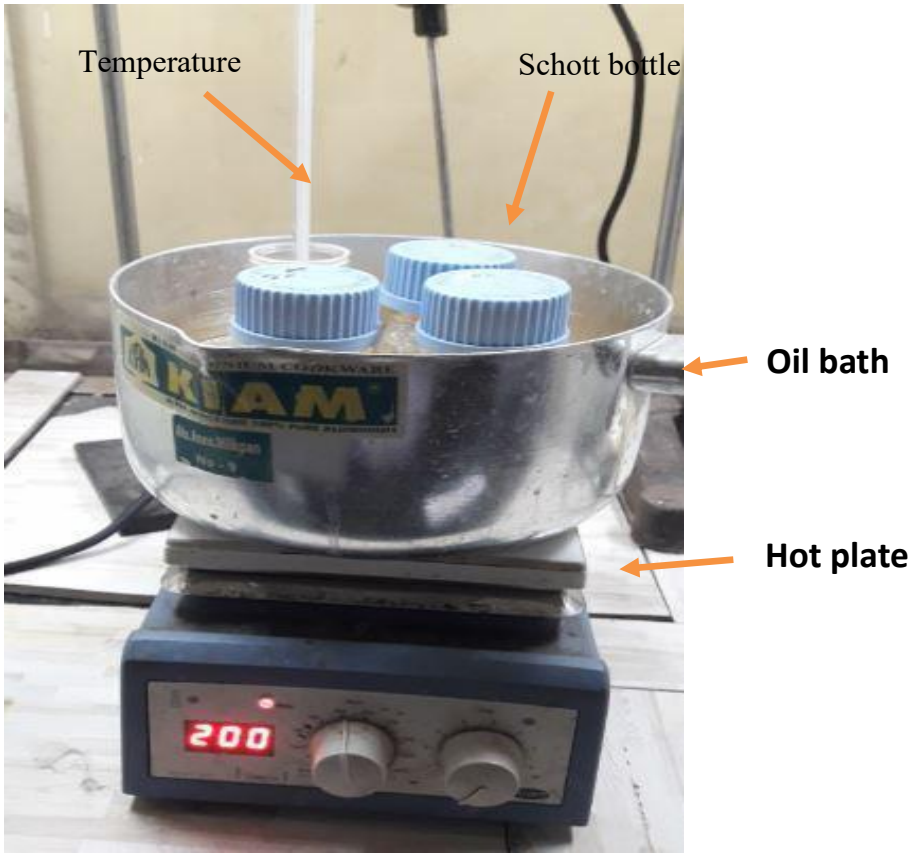

Figure 4.4: A photograph of the home-built hydrothermal growth setup (IPD, BCSIR) of ZnO Nanorods

This orientation prevents ZnO nanoparticles from depositing on the substrate during the hydrothermal growth process. We incrementally heated the complex solution to 90.2 °C in a controlled oil bath over 80 minutes. During this interval, the solution transitioned from transparent to dull, signifying a chemical reaction. The reaction was still confined in Schott bottle for the deposition time, and the oil bath temperature was controlled while the hot plate was set to maintain a temperature of 200 °C. We removed the substrates from the solution after an hour, thoroughly washed them with deionized water, and dried them using an air blower. The hydrothermally prepared thin films were heated for 1 hour at 250 °C in air, similar to the seeded layer, to remove any remaining organic materials from the bath solution [145].

4.8 Estimating Effective Surface Area.

To estimate the effective surface area of the ZnO nanorods (NRs), the NRs were displayed as hexagonal columns. The surface area for a given projected area was calculated using the following equation [146]:

$$A = \sum \left(\frac{3\sqrt{3}}{2} \left(\frac{Dn}{2} \right) 2 + 6 \left(\frac{Dn}{2n} \right) L \right)$$

where:

A is the surface area for a given SEM image,

Dn is the diameter of the NRs measured between opposite corners,

L is the average length of the NRs for a given growth time, measured from the SEM cross sections.

The first part of the equation calculates the area of the top of the NRs, while the second part represents the area of the sides of the nanorods. The schematic form of the nanorod dimensions is shown in Figure 4.5.

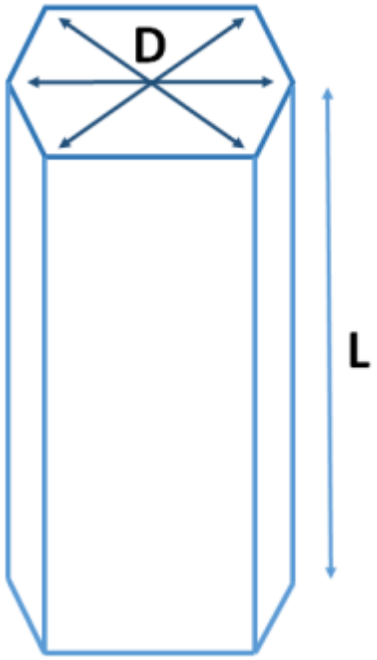

Figure 4.5: The schematic sketch of the nanorod dimensions.

Chapter 5: Results and Discussion

5.1 Introduction

This chapter elaborates the systematic study reporting the detailed structural, morphological, optical, and electrical response of the Aluminium-doped ZnO (AZO) seed layers and ZnO nanorods (NRs) prepared on these seed layers. The aim is to gain insights into the effect of doping concentrations and post-growth annealing conditions on the surface morphology, crystallinity structure, optical transparency and electrical characteristics of the materials. These properties were investigated in detail using advanced characterization techniques such as SEM, EDX, XRD, and PL.

5.2 Characterization of AZO Seed Layers

AZO seed layers thin films are significantly transparent and conductive due to their variety of applications, like solar cells and light-emitting diodes. The study on AZO seed layers in this section includes detailed SEM, EDX, crystal size, optical band gap, thickness, and resistivity analysis.

5.2.1 Morphological Characterization of AZO Seed Layers

The SEM images of AZO seed layers with different Al-doping concentrations are shown in Fig. 5.1 for a comparison of surface morphologies at different doping levels. These are represented in Figs. 5.1(a) and 5.1(b) correspond to doping levels of 2 mol% and 3 mol%, respectively, which exhibit remarkable similarities, indicating comparable structural features at these lower levels of doping. On the other hand, Figures 5.1(c) and 5.1(d), representing doping concentrations of 5% and 8 mol%, display more uniform structural appearance, with minimal variations in morphology, highlighting the potential for optimized material properties across these doping ranges.

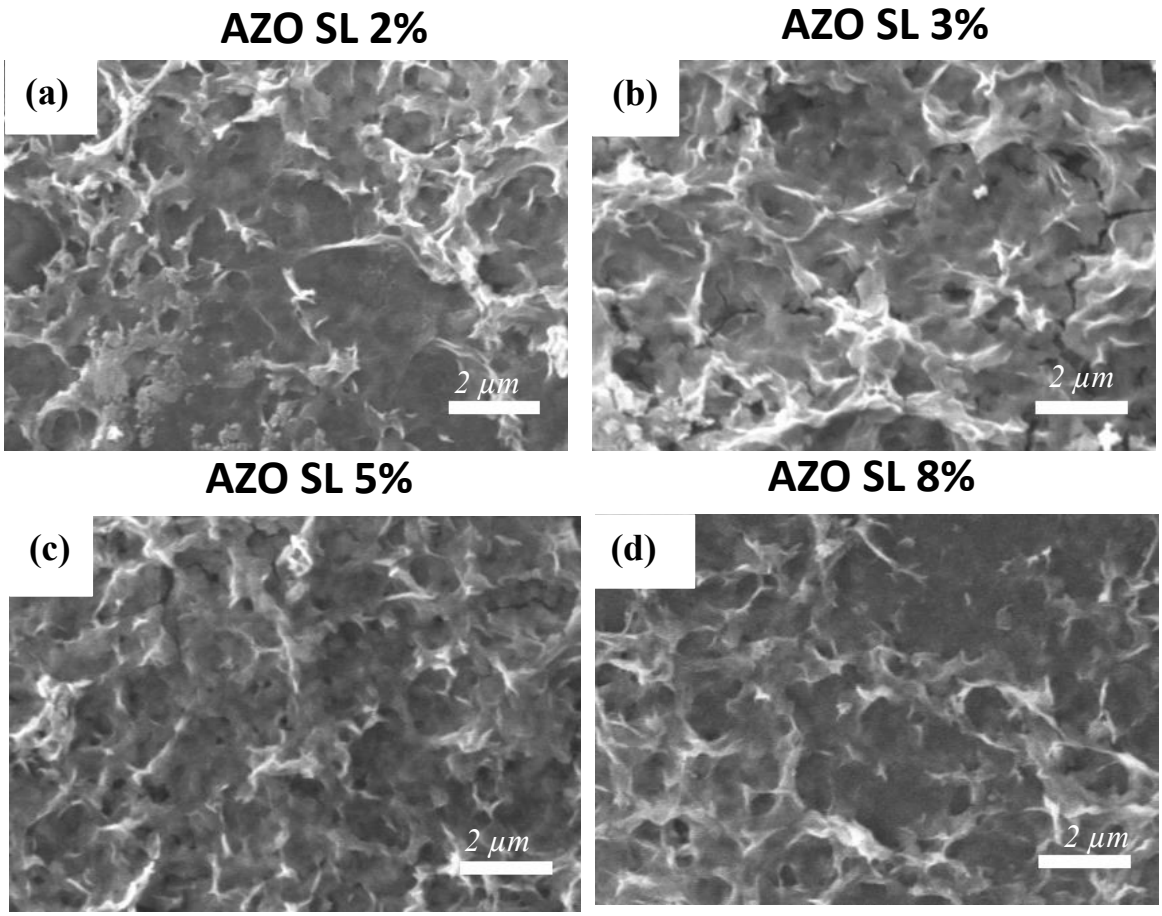

Figure 5.1: Scanning electron microscope micrographs of AZO seed layers (SL) with (a) 2%, (b) 3%, (c) 5%, and (d) 8% Al-doping concentrations. The scale bar in all images is 2 μm.

In all the cases, the SEM images reveal a densely textured pours surface, with a distinct dendrite-like network (bright features) observed across the entire surface area [24]. This dendritic structure, as shown in the images, is crucial for enhancing the conductivity of the thin films, as it promotes better charge transport pathways. The presence of this texture, particularly in the form of a well-organized dendritic network, plays a key role in improving the electrical properties of the films. Consequently, it can be concluded that variations in doping concentration significantly influence the surface morphology, with each doping level contributing to the formation of this conductive surface structure, thereby affecting the overall performance of the thin films.

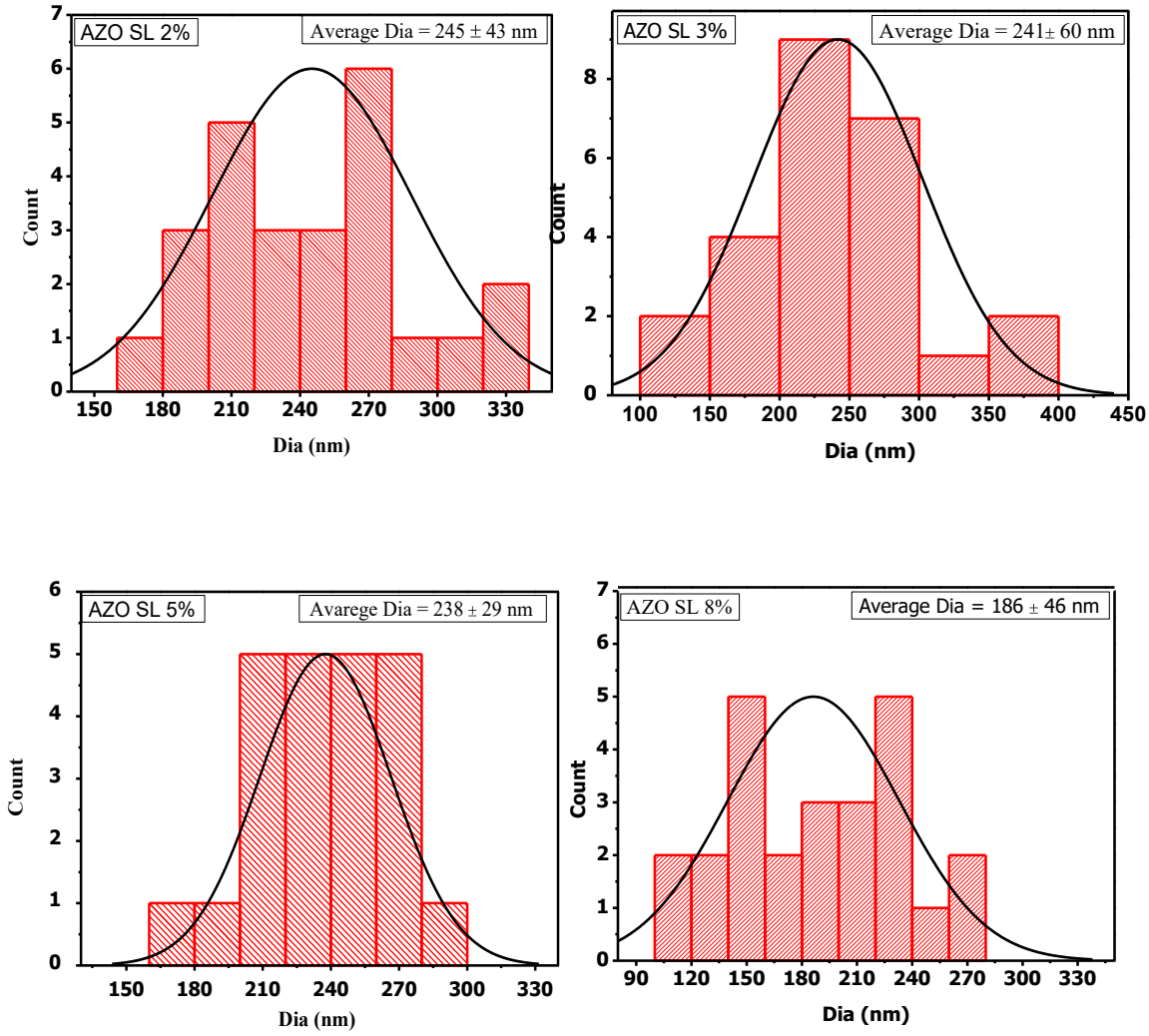

Figure 5.2: Histogram of the various diameters of AZO seeds with (a) 2%, (b) 3%, (c) 5%, and (d) 8% Al-doping concentration onto SLG.

The histograms of the AZO seed layers, as shown in Figure 5.2, illustrate the particle size distribution and its uniformity with increasing doping concentrations. The measured average diameters of the particles for the different doping levels were (245 ± 43) nm, (241 ± 60) nm, (238 ± 29) nm, and (186 ± 46) nm. A noticeable decrease in the average diameter was observed with increasing dopant concentration, which suggests that aluminum ions play a significant role in influencing the grain boundaries. This result is increased nucleation, reduced void formation, and more uniform and compact surface. The histograms give a clear picture of the

individual particles or grains in the thin films. The grain size could be easily improved when compared with the changing doping concentration, which corresponds to the surface quality and the grain organization.

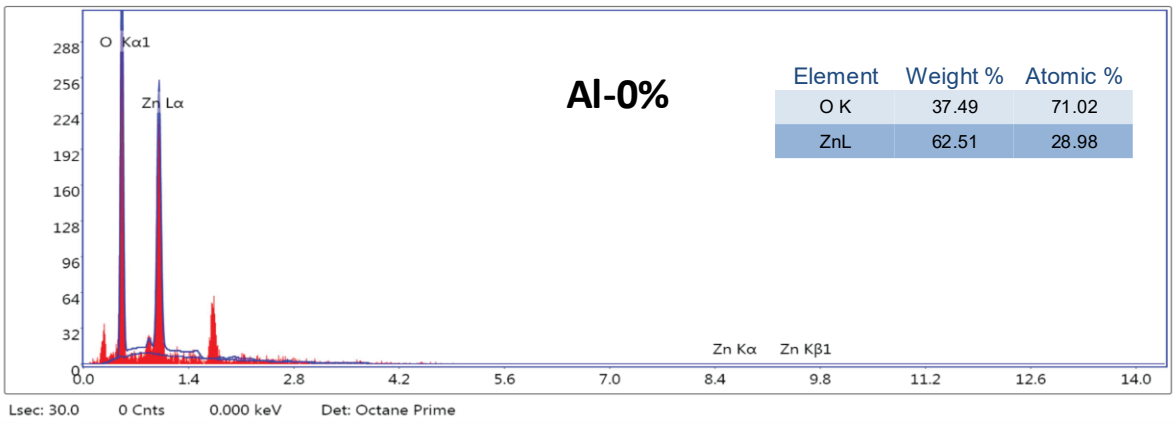

(a)

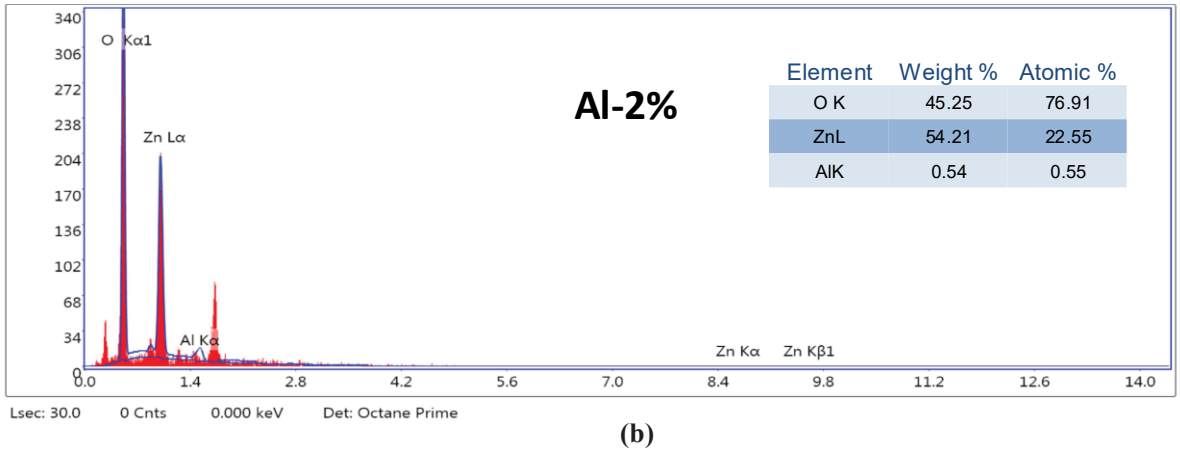

(b)

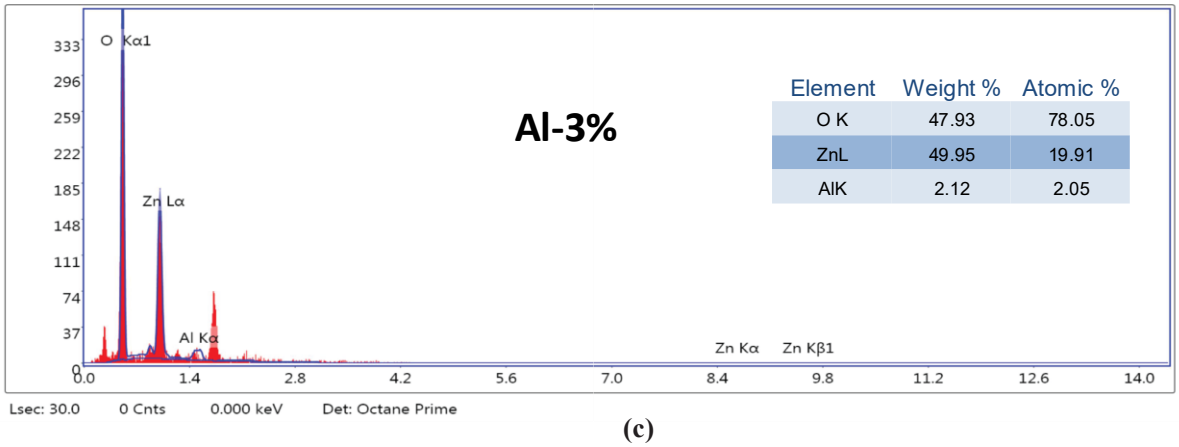

(c)

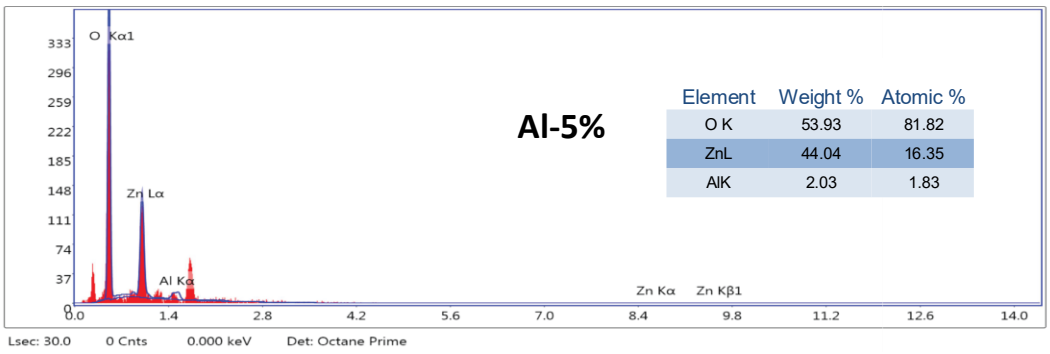

(d)

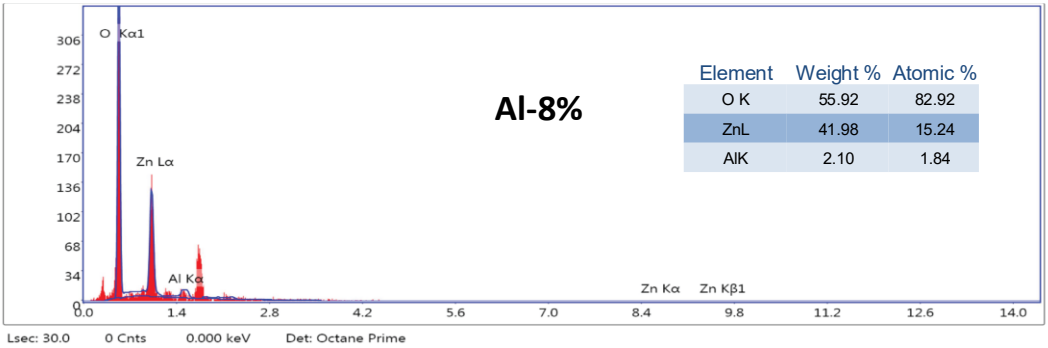

(e)

Figure 5.3: EDX elemental analysis of deposit AZO seed layers with (a) 0%, (b) 2%, (c) 3%, (d) 8%, and (e) 8% of Zn, Al, and O.

Table 5.1: EDX analysis of AZO seed layers and element composition of Zn, Al and 0 with various doping concentrations.

Al^{3+} Concentrations	Zn Wt%	O Wt%	Al Wt%
0%	62.51	28.98	0
2%	54.21	45.25	0.54
3%	49.95	47.93	2.12
5%	44.04	53.73	2.03
8%	41.98	55.92	2.10

EDX measurements offer spectral information of the element content of the AZO seed layers. The Zn, Al and oxygen (O) contents of the samples and corresponding Al/Zn ratios are given in Figure 5.3. The Al contents in the AZO seed layers are 0%, 0.54 wt.%, 2.12 wt.%, 2.03

wt.%, and 2.10 wt.% by doping concentrations as summarized from the data. This change in the Al/Zn ratio has a profound effect on the electrical and optical characteristics of the material as listed in Table 5.1. It can be seen from the results that parameter fluctuations, especially doping concentrations, have a direct impact on the performance of the device, which strongly suggests the necessity of controlling the doping ratio for fine performance tuning.

5.2.2 Characterization of Thickness, Resistivity and Sheet Resistance of AZO Seed Layers.

Electrical and thickness properties of the Al-doped AZO seed layers were examined by the four-point collinear probe method and a gravimetric approach for measuring resistivity (ρ), thickness, and sheet resistance (Rsh) of the fabricated samples. The probe arrangement was such that voltage and current were measured through the material; the voltage being applied directly across the material. Resistance is an important property of the material, which is related to the resistance to the flow of the electric current within the material. The resistivity, as the resistance of a wire per unit of cross-sectional was estimated to measure the current-carrying capability of the same. These data offer valuable understanding of the electrical behaviors of the AZO seed layers, which, however, are strongly dependent on the doping levels as well as the thickness of the films.

Table 5.2: Surface Resistivity (four-point collinear probing method) of AZO Seed layers.

AZO Seed Layer On SLG	Al- Doping (%)	Film Thickness (nm)	Resistivity (ρ) (kΩ-cm)
	2	492	30.1 ± 1.5
	3	178	13.0 ± 0.2
	5	731	41.4 ± 3.9
	8	283	19.8 ± 0.2

The average thickness of the AZO seed thin film used in this work was in the range from 178 nm to 731 nm by gravimetric analysis. Resistivity measurements, obtained using a four-point collinear probe technique, revealed values ranging from (13.0 ± 0.2) kΩ·cm to (41.4 ± 3.9) kΩ·cm. The thickness, resistivity, and conductivity of the films were measured and are shown in Table 5.2.

5.2.3 Optical Characterization of AZO Seed Layers.

The UV − VIS − NIR spectroscopy was used to study the optical properties of the AZO seed layers. The transmittance spectra as well as the optical band gap were investigated for different levels of aluminium (Al) doping. As shown in Figure 5.4, the maximum transmittance of the AZO thin film was reached up to 90%, which indicates that the AZO material possesses high transparency in the visible spectrum. The optical band gap of the films was also measured between 3.44 and 3.55 eV, and a slight lack of change depending on the Al doping concentration, as shown in Figure 5.5. These features demonstrate the potential of AZO thin films for optoelectronic devices grow to the high transparency and appropriate band gap ensuring better performance of the device application.

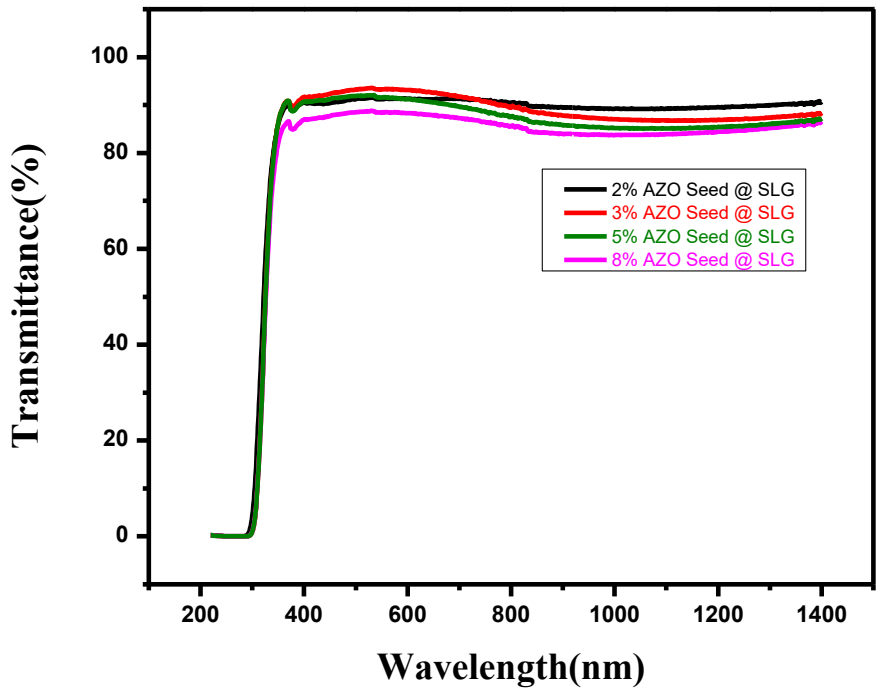

Figure 5.4: Variation of transmittance vs. wavelength of AZO seed layers at different doping concentrations.

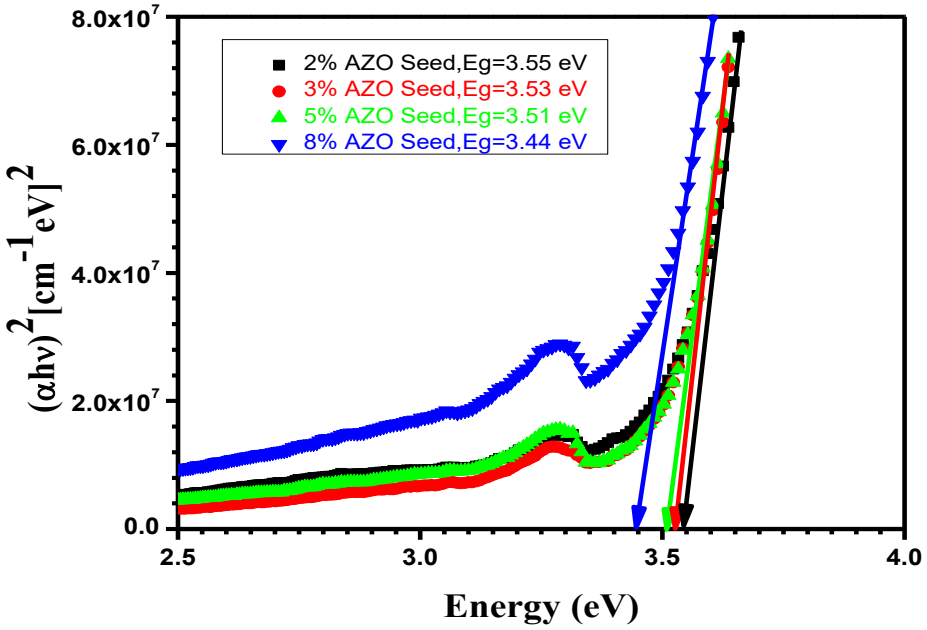

Figure 5.5: Variation of energy band gap of AZO seed layers at different doping concentrations.

Table 5.3: Comparison study of AZO seed layers' thin film parameters.

AZO Seed Layer On SLG	Al-Doping (%)	Film Thickness (± 20 nm)	Resistivity (ρ) (kΩ-cm)	Average Diameter (nm)	Al Wt.% Composition	Bang Gap E_g (eV)
	2	492	30.1 ± 1.5	245 ± 43	0.54	3.55
	3	178	13.0 ± 0.2	241 ± 61	2.12	3.53
	5	731	41.4 ± 3.9	238 ± 39	2.03	3.51
	8	283	19.8 ± 0.2	186 ± 46	2.10	3.44

So, to summarize, the AZO seed thin films were characterized using various techniques, including SEM, EDX, thickness measurement, resistivity, and optical analysis. SEM and EDX confirmed the uniformity and elemental composition, while the thickness varied between 178 nm and 730 nm. Resistivity measurements showed a range of values from (13.0 ± 0.2) kΩ·cm to (41.4 ± 3.9) kΩ·cm, indicating a dependence on film thickness. Optical properties, analyzed through UV-VIS-NIR spectroscopy, revealed a high transmittance of 90% and an optical band gap between 3.44 and 3.55 eV, demonstrating the material's suitability for optoelectronic applications.

5.3: Characterization of Zinc Oxide Nano Rods

The characterization of ZnO NRs was carried out using XRD, SEM, photoluminescence (PL), optical band gap analysis, and sheet resistance measurements. Crystalline structure was characterized by XRD, and the nanorod morphology and dimensions were analysed by SEM. PL study revealed the optical properties, and sheet resistance measurements determined the electrical conductivity, which are important for any optoelectronics and sensor applications.

5.3.1 Structural Characterization of ZnO NRs

The XRD pattern for the ZnO nanorod (NR) thin films were confirmed the crystalline structure. The XRD patterns of doped ZnO nanorods at different doping concentrations of 2%, 3%, 5%

and 8 mol% are shown in Figure 5.6. This analysis offers useful information on the crystallinity and phase purity of the films. These peaks are related to the wurtzite structure of ZnO (002), (101), (102), (103) and (004). The XRD results showed the prominent peak at the (002) plane corresponding to the hexagonal wurtzite structure of ZnO nanorods along the c-axis direction.

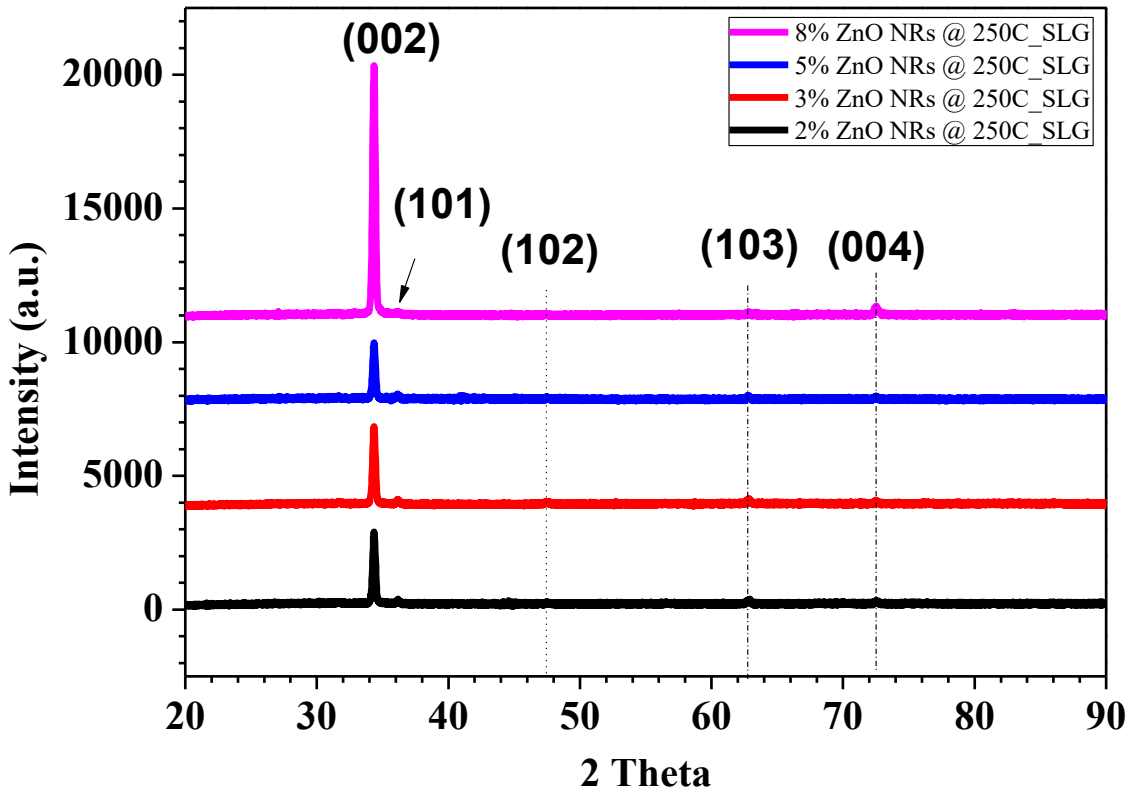

Figure 5.6: X-ray Diffraction Spectra of ZnO NRs film with different doping concentrations.

The XRD peaks of the ZnO NRs were found at 2θ positions 34.350, 34.344, 34.348, 34.345 for doping concentrations 2, 3, 5, and 8 mol%, respectively. Notably, the peak intensity was most significant at the 8 mol% doping concentration, indicating enhanced crystallinity. The Full Width at Half Maximum (FWHM) of the (002) peak was measured to be 0.2605 deg., and the crystallite size was calculated to be 31.54 nm, suggesting improved crystallization with higher doping. A detailed summary of the lattice constants (a and c), crystallite size, and FWHM values is provided in Table 5.4.

Table 5.4: Structural parameters of ZnO NRs thin film with different doping concentrations

Al–doping concentration (mol%)	2Θ (002) (deg.)	Lattice constant, *a* (Å)	Lattice constant, *c* (Å)	*c*/*a*	Crystallite size (nm)	FWHM (deg.)
2	34.350	2.6075	5.2154	1.73	31.12	0.2640
3	34.344	2.6076	5.2153	1.73	31.16	0.2637
5	34.348	2.6076	5.2156	1.73	31.19	0.2673
8	34.345	2.6079	5.2157	1.73	31.54	0.2605

5.3.2 Morphological Characterization of ZnO NRs

Figures (5.7 to 5.10) display the surface morphology of ZnO nanorods (NRs) grown on AZO seed layers at various doping concentrations. The SEM images clearly reveal a well-aligned hexagonal wurtzite structure along the C-axis (002) direction, demonstrating the crystalline integrity of the nanorods. The AZO seed layers played a crucial role in promoting the growth of well-aligned ZnO nanorods. From the top view of the micrographs, it is evident that the nanorods generally originate from a common nucleation site, particularly when the seed layer density is high, as previously reported by Farhad et al. [24]. This uniformity in growth is a testament to the effectiveness of the AZO seed layers in controlling the morphology of the ZnO NRs.

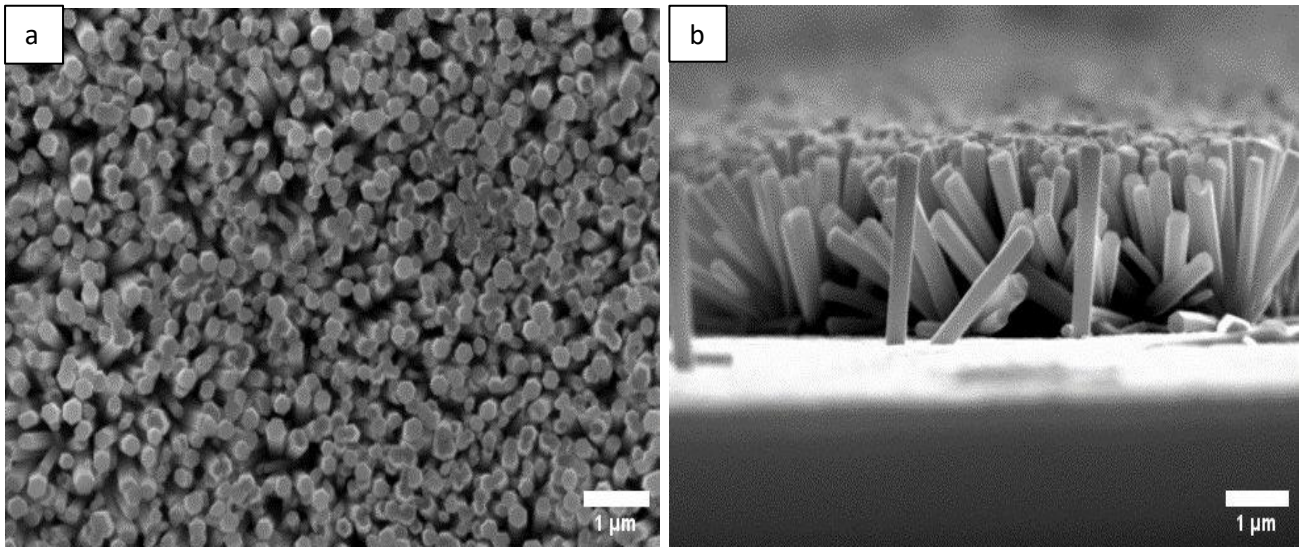

Figure 5.7 :(a) Top view and (b) Cross-section view of the SEM micrographs of 2 mole% ZnO NRs at 250 °C

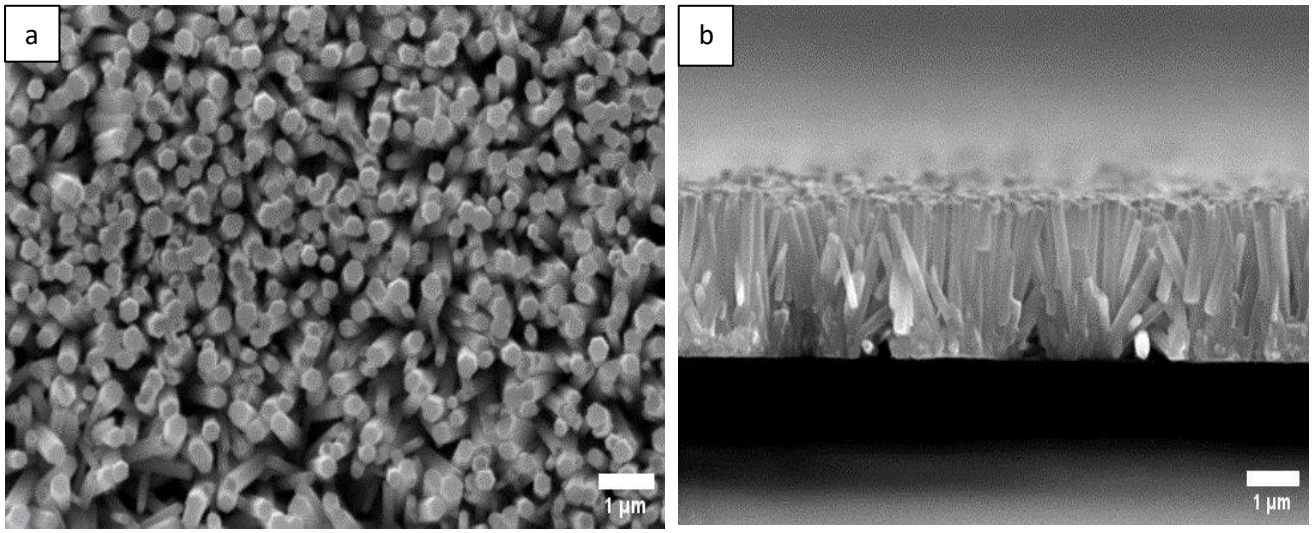

Figure 5.8 :(a) Top view and (b) Cross-section view of the SEM micrographs of 3 mole% ZnO NRs at 250 °C

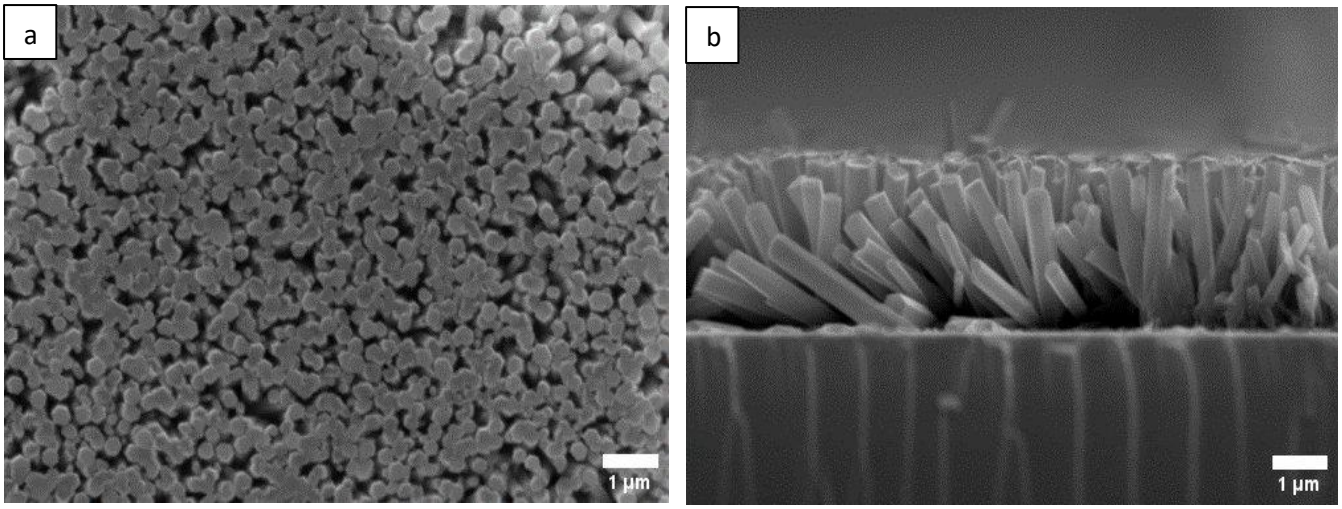

Figure 5.9:(a) Top view and (b) Cross-section view of the SEM micrographs of 5 mole% ZnO NRs at 250 °C

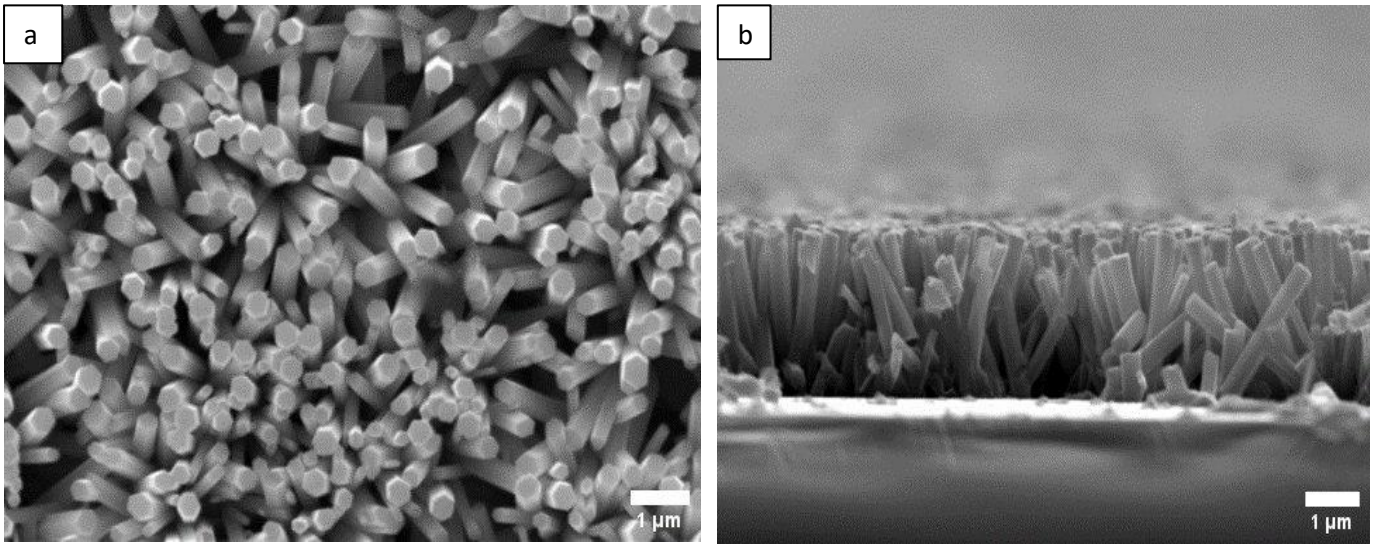

Figure 5.10 :(a) Top view and (b) Cross-section view of the SEM micrographs of 8 mole% ZnO NRs at 250 °C

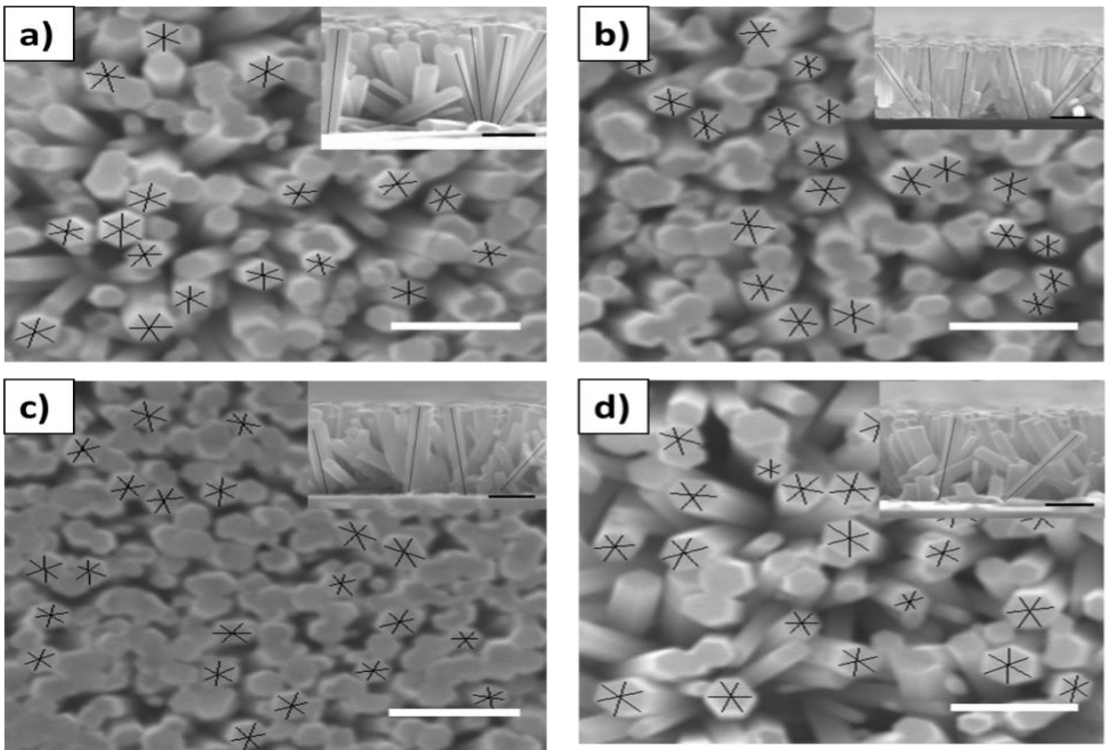

(A)

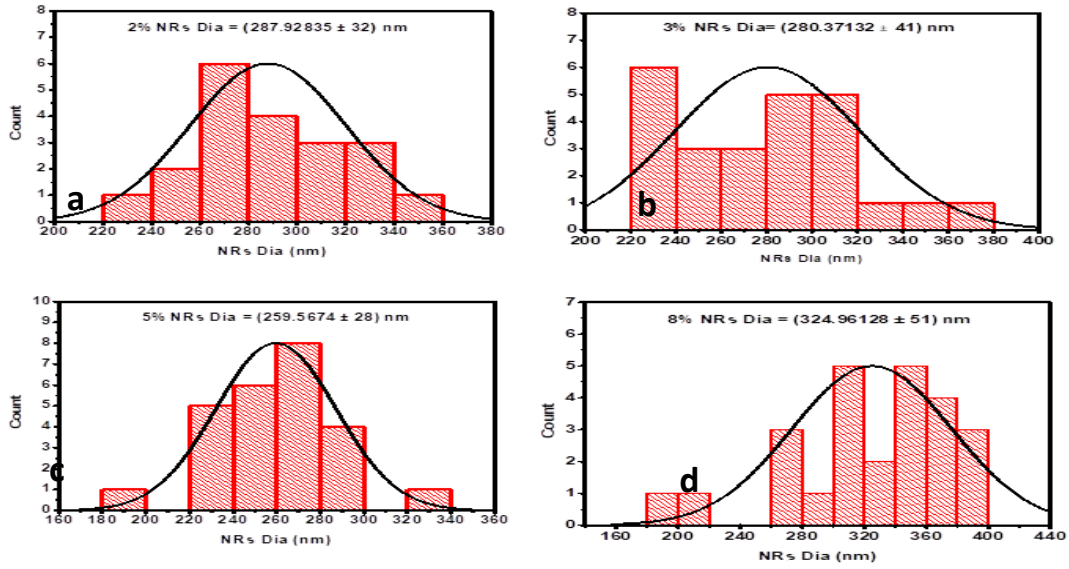

(B)

Figure 5.11: SEM image of (A) Diameter measurement ZnO NRs top-view and cross-section view (inset) of (a) 2%, (b) 3%, (c) 5%, and (d) 8% Al-doping concentrations (B) Histogram of different diameters of ZnO NRs.

The average diameters of the ZnO nanorods were measured as (288 ± 32) nm, (280 ± 41) nm, (260 ± 32) nm, and (325 ± 50) nm for doping concentrations of 2%, 3%, 5%, and 8 mol%, respectively. A decrease in the diameter with increasing dopant concentration can be attributed to the atomic radii of Zn (1.31 Å) and Al (1.26 Å), which are nearly identical. Notably, Al atoms substitute for Zn sites in the crystal lattice, leading to lattice deformation.

The lengths of the ZnO NRs were found to be (2410 ± 37) nm, (2355 ± 94) nm, (2357 ± 44) nm, and (2339 ± 13) nm, as shown in Table 5.5. From the Figure 5.11 (A & B), the nanorod densities, or the number of rods per unit area, were calculated as (9.90×10^6) nm^{-2}, (6.80×10^6) nm^{-2}, (11.02×10^6) nm^{-2}, and (6.01×10^6) nm^{-2} respectively, as presented in Table 5.5.

Table 5.5: The Rod density, average diameter, and length obtained from SEM images of ZnO NRs.

Al-doping concentration	Rod Density ($\times 10^6$ nm^{-2})	Rod Length L (nm)	Rod Diameter D (nm)	Aspect Ratio (L/D)
2%	09.90	2410 ± 37	288 ± 31	8.36
3%	06.80	2355 ± 94	280 ± 40	8.39
5%	11.02	2357 ± 45	260 ± 27	9.08
8%	06.01	2339 ± 13	325 ± 50	7.19

With increasing Al doping concentration, a noticeable decrease in the rod density was observed, accompanied by an increase in the aspect ratio, which varied as 8.36, 8.39, 9.08, and 7.19 for doping concentrations of 2%, 3%, 5%, and 8 mol%, respectively. The higher aspect ratio indicates that the nanorods became longer and thinner as the doping concentration increased. This morphological change can be attributed to the influence of the AZO seed layers, which played a crucial role in controlling the growth of the ZnO nanorods, both in terms of size and density. The seed layers effectively promoted the formation of longer, more elongated nanorods while reducing the overall rod density.

5.3.3 Photoluminescence Analysis of ZnO NRs

The PL spectra of the ZnO nanorods, synthesized via the hydrothermal method at four different doping concentrations, are shown in Figure 5.12. Two distinct emission peaks were observed in the spectra. The first, a blue emission peak, appeared in the near-band edge (NBE) region of the UV spectrum at 380 nm. The second, a green emission peak, was observed in the deep-level emission (DLE) region of the visible spectrum, spanning from 500 nm to 700 nm. It was observed that the intensity of the NBE peak in UV range was significantly increased on doping concentration; on the other hand, the hump shape emission peak in visible range was gradually diminished due to decrease of defect-related emissions caused by improved crystallinity of the ZnO nanorods.

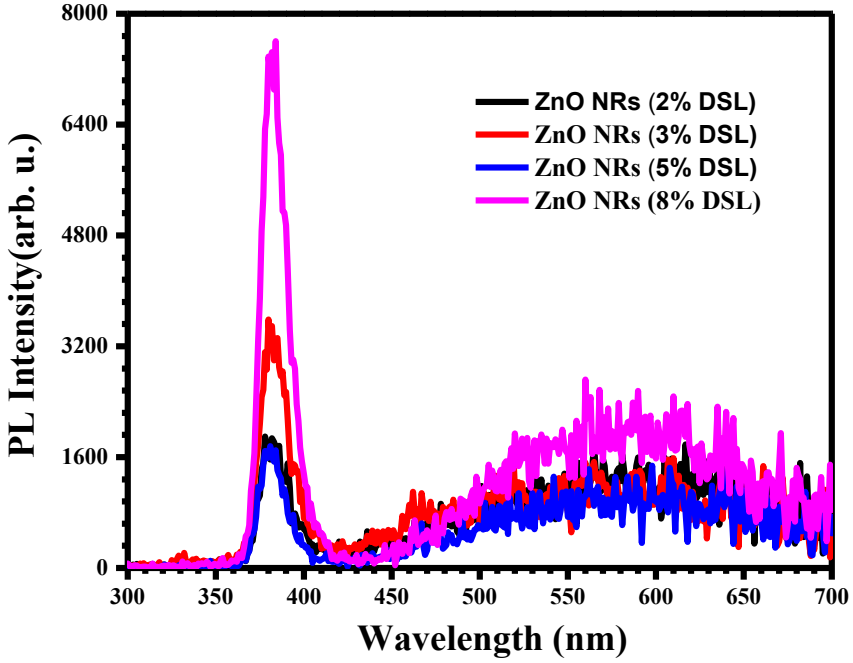

Figure 5.12. Room temperature PL spectra of as-made ZnO Nanorods on 2%, 3%, 5% and 8% Al-doped seed layer (DSL) grown on SLG substrates.

The deep-level emission observed in the visible region is commonly attributed to oxygen vacancies within the ZnO nanorods. The emission peaks vary in intensity and position with doping concentration. Notably, at a doping concentration of 8 mol%, both a sharp intensity peak in the near-band edge (NBE) region and a pronounced peak in the deep-level emission (DLE) region were observed. These results are in good agreement with what is reported for the non-doping ZnO NR by Farhad et al. (2018) [142]. It was in good agreement with the literature report, the PL spectra of ZnO nanorods typically showed a strong UV emission peak around 380 nm and a broader visible emission peak, which was observed within the range of 500 nm – 600 nm (Ashfold, 2007) [147].

5.3.4 Optical Characterization of ZnO NRs

The optical band gap (Eg) was determined using the Tauc plots:

$$(\alpha h\upsilon)^2 = A(h\upsilon - Eg)$$

where α is the absorption coefficient, $h\upsilon$ is the incident photon's energy, Eg is the optical band gap, and A is a proportionality constant in this equation.

The band gap (Eg) can be determined using the wavelength (λ) via the formula

$$E_g = \frac{1240}{\lambda}$$

The maximum diffuse reflection of the ZnO nanorods (NRs) was found to be 70%, with the diffuse reflection band gap ranging from 3.06 eV to 3.16 eV, as shown in Figure 5.14.

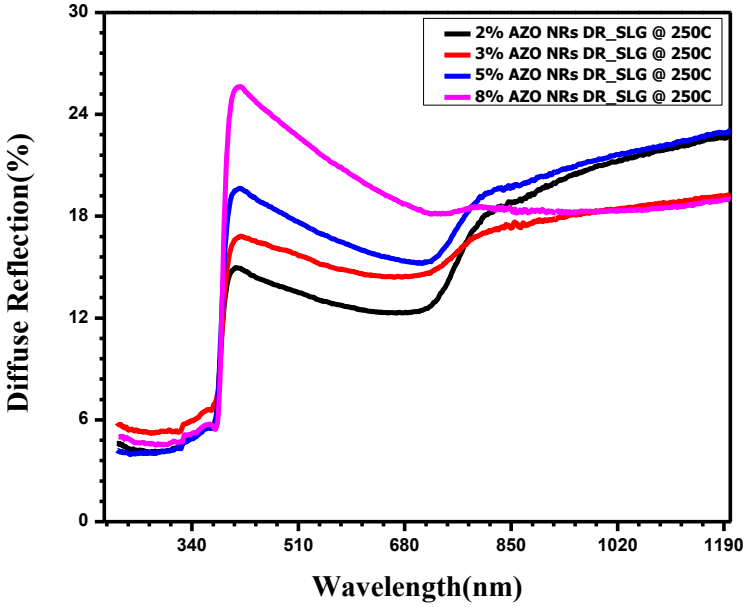

Figure 5.13: Variation of Diffuse Reflection vs. wavelength, of ZnO NRs at different doping concentrations.

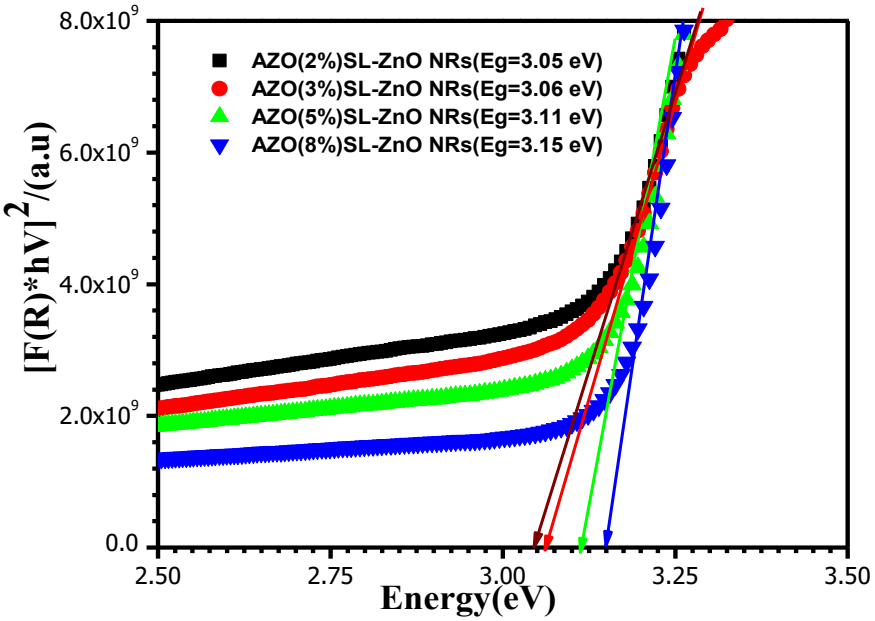

Figure 5.14: Variation of energy Band gap of ZnO NRs on AZO SL at different doping concentrations.

Upon analyzing the optical properties, it was observed that both the transmittance and optical band gap decreased with increasing Al-doping concentration. The highest transmittance of 90% was recorded for the AZO seed layer thin film, while an average transmittance of 65% was observed for the ZnO NR thin film. The reduction in transmittance was attributed to the increasing Al doping concentration and variations in the annealing effects. Additionally, the decrease in the optical band gap due to the dopants contributed to enhanced electrical conductivity, highlighting the interplay between optical and electrical properties in the nanorods.

5.3.5 Characterization of Sheet Resistance of ZnO NRs

The sheet resistance was calculated using the equation:

$$R_{sh} = 4.53 \times f_1 \times R_{4pp}$$

Where f_1 is the geometrical correction factor that depends on the geometry of the substrate, R_{4pp} is the 4-point collinear probe resistance determined by using Ohm's law.

The sheet resistance was measured using the four-point collinear probe method. The lowest sheet resistance was measured for 8 mol% at 114 MΩ/Square as shown in Table 5.6.

Table 5.6: A comprehensive comparison of the parameters for ZnO nanorods (NRs), Key observations

Al-doping concentration	Rod Density ($\times 10^6$ mm^{-2})	Aspect Ratio (L/D)	Crystallite size (nm)	Band Gap (eV)	Sheet Resistance (MΩ/□)	FWHM (deg.)
2%	9.90	8.36	31.12	3.05	450	0.2640
3%	6.80	8.39	31.16	3.06	352	0.2637
5%	11.02	9.08	31.19	3.11	706	0.2673
8%	06.01	7.19	31.54	3.15	114	0.2605

So, to summarize, the properties of ZnO nanorods (NRs) were studied at different Al-doping concentrations (2%, 3%, 5%, and 8%). The rod density varied, with the highest value observed at 5% doping (11.02×10^6 nm^{-2}), while the lowest was at 8% doping (6.01×10^6 nm^{-2}). The aspect ratio (L/D) showed an increasing trend, with the highest value at 5% doping (9.08). The crystallite size remained relatively constant, ranging from 31.12 nm to 31.54 nm across the doping levels.

The optical band gap increased from 3.05 eV at 2% doping to 3.15 eV at 8% doping, indicating a slight redshift with higher doping concentrations. Sheet resistance was lowest at 8% doping (114 MΩ/□), suggesting improved conductivity. The FWHM values varied slightly between 0.2640 deg and 0.2605 deg, indicating narrow peaks and good crystallinity.

5.4 Characterization of Post-Annealing Effect of ZnO NRs

Post-annealing treatment plays a crucial role in enhancing the structural and optical properties of ZnO nanorods (NRs), as it helps in reducing defects, improving crystallinity, and influencing their electrical and optical characteristics, which are essential for various applications.

5.4.1 Annealing Effect on the Structure Characterization of ZnO NRs.

The X-ray diffraction (XRD) analysis reveals two prominent peaks, (002) and (101), in the normalized intensity pattern, as shown in Figure 5.15. These peaks correspond to a hexagonal wurtzite structure with a C-axis orientation. The XRD patterns of all ZnO nanorod samples primarily exhibit the (002) peak, with the (101) peak being almost absent, suggesting the single-phase nature of the ZnO nanorod thin films.

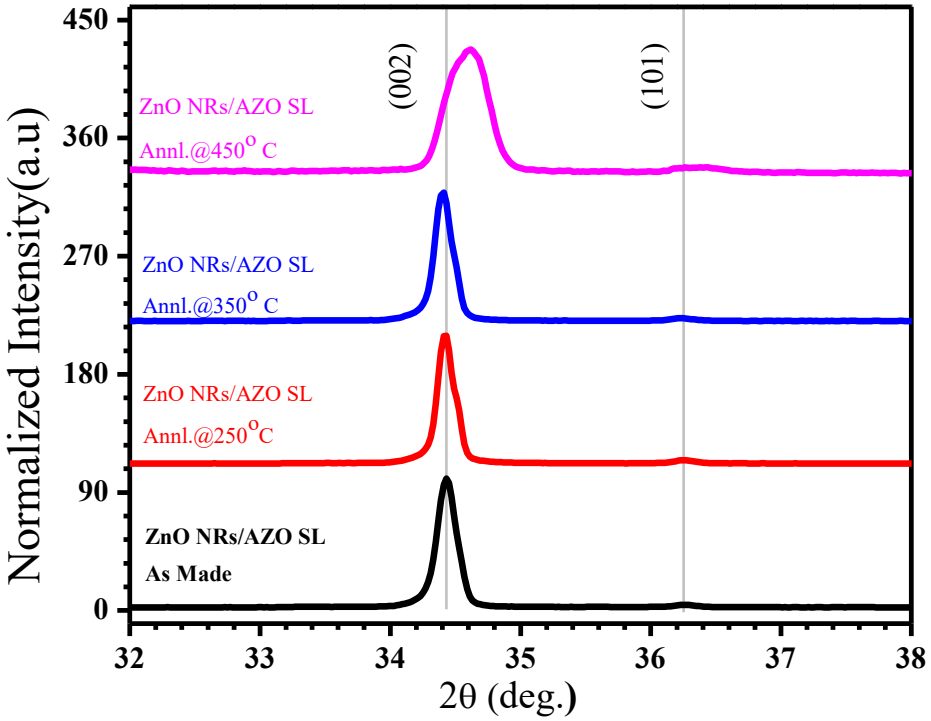

Figure 5.15: Normalized X-ray diffraction (XRD) patterns of ZnO NRs on 8 mole% with temperature variation.

At various annealing temperatures, the 2θ values of the XRD peaks were observed at 34.43°, 34.41°, 34.40°, and 34.60° for temperatures of 250 °C, 350 °C, and 450 °C, respectively, with the peak positions shifting to lower 2θ values as the annealing temperature increased. The highest crystallite size (48.58 nm) and the lowest full-width at half-maximum (FWHM) (0.1692) were achieved at the optimum annealing temperature of 250°C, indicating good crystallization. Farhad et al. [29] reported a similar observation of the (002) peak at 250°C using a zinc oxide seed layer for the hydrothermal growth of zinc oxide nanorods. Furthermore, it was noted that the crystallite size decreased significantly with increasing aluminum doping, as higher doping concentrations led to a reduction in the crystallite size. All values for the lattice parameter (c/a), crystallite size, and 2θ values at different annealing temperatures for the dominant (002) peak are presented in Table 5.7.

The crystallite size of the films was calculated using the Scherrer equation:

$$D = \frac{K.\lambda}{\beta.cos\theta}$$

Here, D is the crystallite size, K is the shape factor (0.9), λ =1.5406 A^0, β is the FWHM of the peak in radiation, and θ is the Bragg angle.

Table 5.7: Structural properties obtained from X-ray diffraction analysis with temperature variation.

Annealing Effect	2Θ (002) (deg.)	Lattice constant, *a* (Å)	Lattice constant, *c* (Å)	*c*/*a*	Crystallite size (nm)	FWHM (deg.)
As made	34.43	2.6013	5.2034	1.73	43.84	0.1875
250 ^{0}C	34.41	2.6034	5.2063	1.73	48.58	0.1692
350 ^{0}C	34.40	2.6046	5.2078	1.73	46.73	0.1759
450 ^{0}C	34.60	2.5905	5.1780	1.73	22.38	0.3674

5.4.2 Annealing Effect on the Surface Morphology of ZnO NRs of 8 Mol%.

The annealing effect on the growth of ZnO NRs at different temperatures is shown in Figures (5.16 to 5.19). The results show improved alignment and the crystalline hexagonal shape of the rods, indicating the formation of high-quality ZnO nanorods. These rods are well-aligned vertically on AZO seed layers, as confirmed by both the top and side views observed in the scanning electron microscopy (SEM) images.

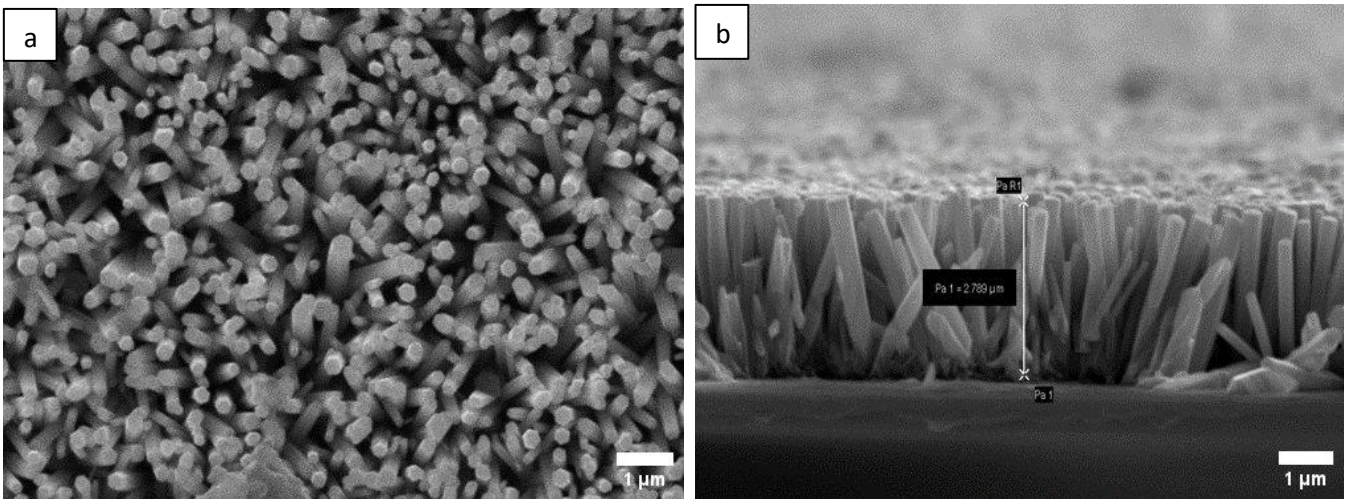

Figure 5.16: (a) Top view and (b) cross-section view of the SEM micrographs of 8 mole% of as-made ZnO NRs

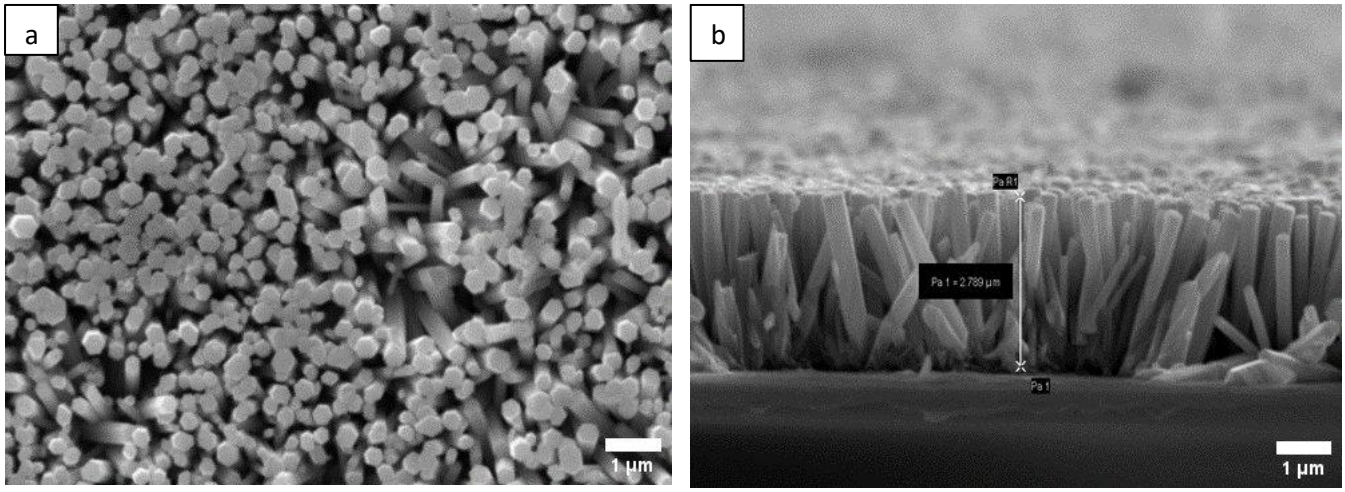

Figure 5.17: (a) Top view and (b) cross-section view of the SEM micrographs of 8 mole% of ZnO NRs @ 250^0C

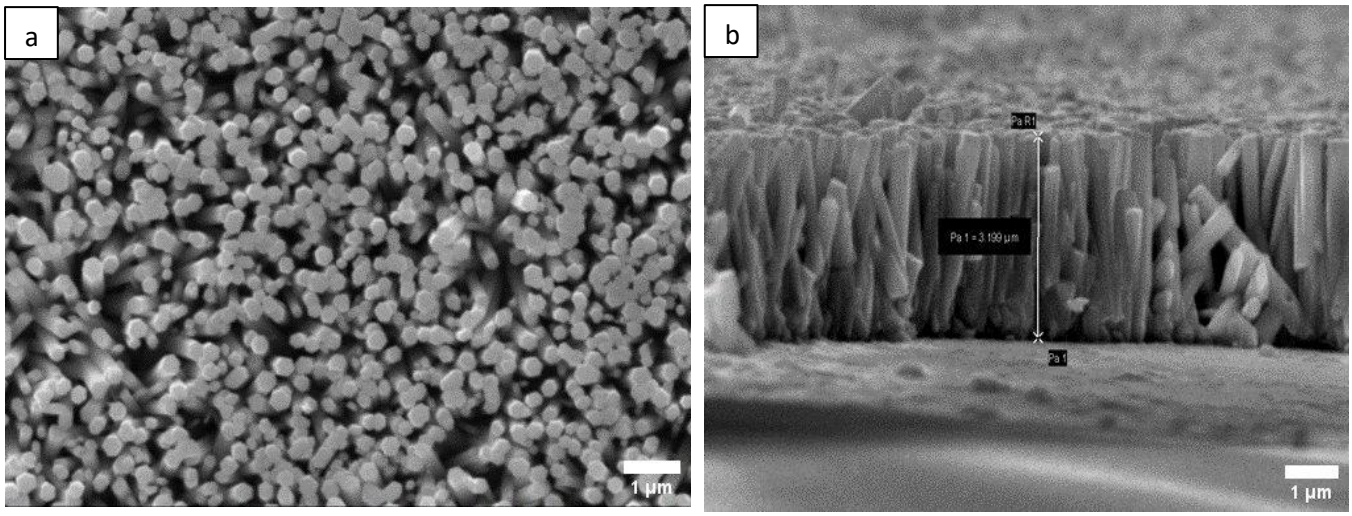

Figure 5.18: (a) Top view and (b) cross-section view of the SEM micrographs of 8 mole% of ZnO NRs_SLG. Annealed @ 350^{0}C

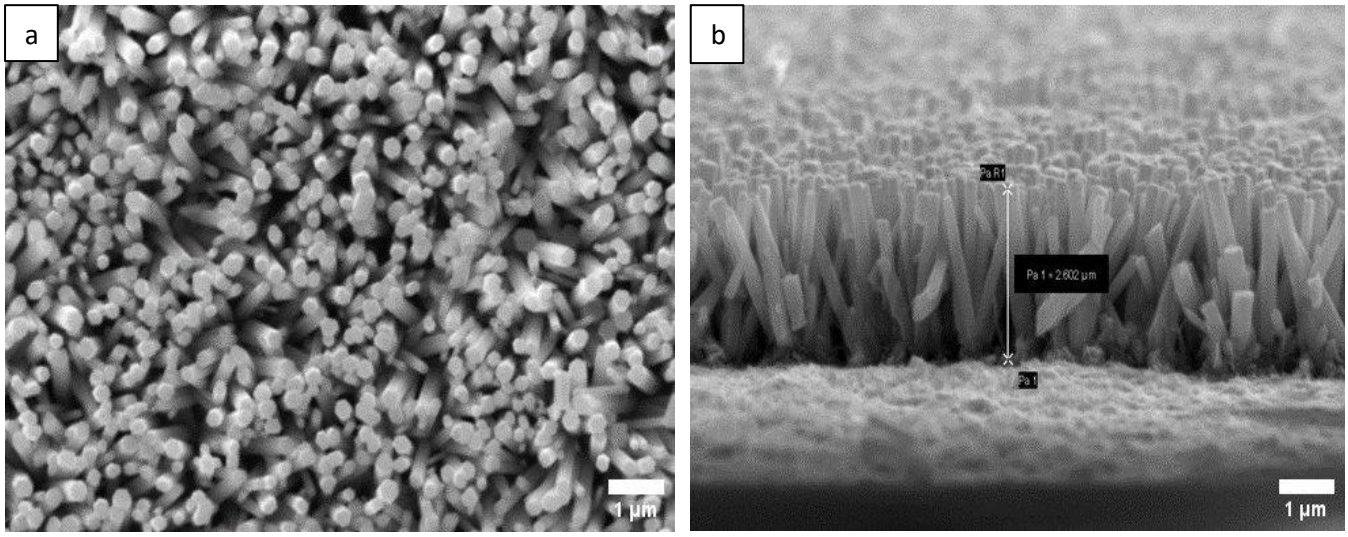

Figure 5.19: (a) Top view and (b) cross-section view of the SEM micrographs of 8 mole% of ZnO NRs Annealed @ 450^{0}C

The rod density was measured at ten different spots from the top view of the SEM image within an area of 1021.53 nm × 1021.53 nm. A notable improvement in rod density was observed, reaching 9.423 × 10^6 mm^{-2}, alongside the highest aspect ratio of 22.11. As the annealing

temperature increased from 250 °C to 350 °C and 450 °C, both the length and diameter of the nanorods decreased, as summarized in Table 5.8.

A significant change in rod density was observed at 250 °C, and the aspect ratio of the length to the diameter was compared. The majority of the nanorods (NRs) in the sample were oriented along the C-axis direction. The diameters of the ZnO NRs were measured as 365 nm, 294 nm, 284 nm, and 246 nm. The lowest aspect ratio, recorded as 07.12, corresponded to a rod density of 85 million per mm². This reduction in nanorod size can be attributed to the presence of aluminum atoms at zinc sites in the rod structure, which led to the observed size decrease. Aluminum (Al) has a smaller atomic radius (118 pm) compared to zinc (Zn) (142 pm), as described by S. Rajamanickam et al. (2020) [145].

Table 5.8: Aspect ratio of 8 mole% ZnO NRs and rod density obtained from SEM micrographs at different temperatures.

Temperature variation	Rod Density ($\times 10^6$ mm^{-2})	Rod Length L (nm)	Rod Diameter D (nm)	Aspect Ratio (L/D) from SEM
As made	8.57	2608	366	07.12
250 ^{0}C	9.42	3255	294	11.07
350 ^{0}C	9.33	3079	284	10.84
450 ^{0}C	7.23	2677	246	10.88

5.4.3 Annealing Effect on the Photoluminescence Analysis of ZnO NRs.

The deep-level emission (DLE) in the visible region is typically associated with oxygen vacancies in the layer. The emission peak shifted as a result of variations in doping levels. It was observed that the sharp intensity peak in the near-band-edge (NBE) and the prominent peak in the DLE occurred at a doping level of 8 mole%, in good agreement with the findings

of Farhad et al. (2018). According to the literature, most photoluminescence (PL) spectra for zinc oxide nanorods (ZnO NRs) exhibit a distinct ultraviolet (UV) emission feature at 380 nm, alongside a significantly broader emission feature in the visible spectrum, specifically within the range of 500 to 600 nm (Ashfold, 2007; Farhad et al., 2018) [142,146].

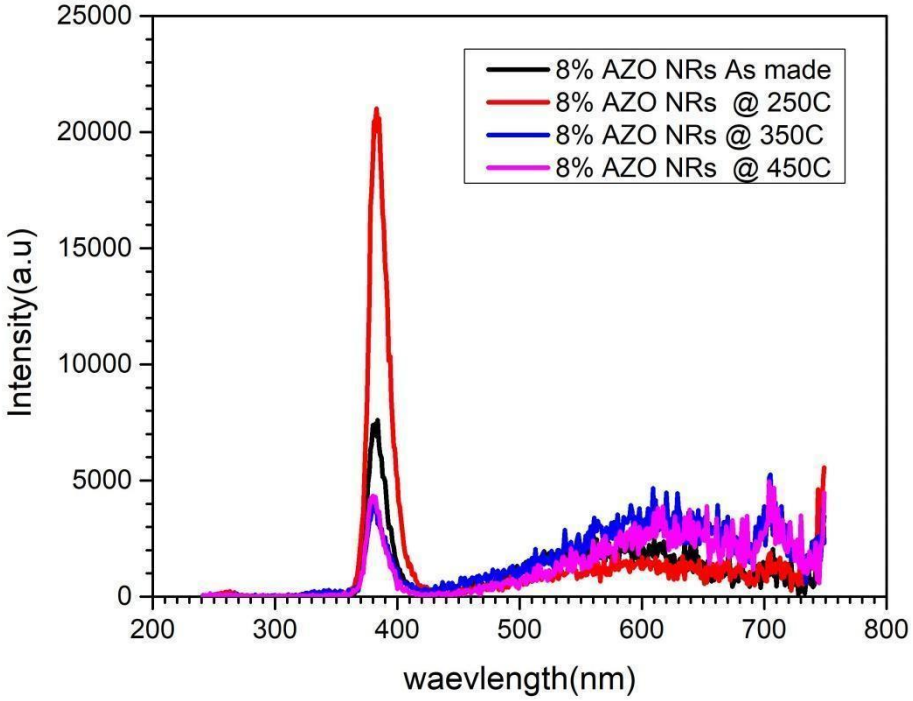

Figure 5.20. PL Spectra of 8% of ZnO NRs thin films annealed at different temperatures deposited on SLG substrates.

The optimum doping concentration is considered to be 8 mol%, with annealing effects observed at temperatures of 250 °C, 350 °C, and 450 °C. As shown in Figure 5.20, the sharp intensity peak in the near-band-edge (NBE) region increased, while the intensity peak in the visible region decreased at 250 °C. Additionally, a new intensity peak appeared, and the annealing effects at 350 °C and 450 °C led to a decrease in the NBE emission at 380 nm (I_{380}nm), accompanied by an increase in the visible emission peak at 600 nm (I_{600}nm).The intensities at the two positions under the area under curve are calculated using the Gaussian or Lorentzian formula. Furthermore, the NBE band gap, which ranges from 3.22 to 3.25 eV

as derived from the photoluminescence spectra, is in good agreement with the estimated optical band gap, which ranges from 3.12 to 3.16 eV for the ZnO nanorods (NRs).

Table 5.9: Band gap values of Diffuse reflection and Photoluminescence Spectra annealed at different temperatures of 8 mole% of ZnO NRs thin films.

Temperature	PL (Intensity)				
	I_{380nm}	I_{600nm}	Ratio = I_{600}/I_{380}	Diffuse Reflection E_g(eV)	Band Gap from PL (eV)
As made	129973	479446	3.69	3.15	3.23
250 ^{0}C	376942	508602	1.34	3.16	3.22
350 ^{0}C	65196	533440	8.18	3.12	3.23
450 ^{0}C	68328	476719	6.97	3.14	3.25

This estimated band gap, ranging from 3.12 to 3.16 eV, was calculated using a Tauc plot based on the diffuse reflection data presented in Table 5.9. In conclusion, the post-heat treatment at 250 °C reduced the green emission peak in the visible region, indicating the formation of a high-quality thin film.

5.4.4 Optical analysis of post-annealing effect of ZnO NRs

The optical band gap (Eg) was determined using the Tauc plots:

$(\alpha h\upsilon)^2 = A(h\upsilon - Eg)$

where α is the absorption coefficient, $h\upsilon$ is the incident photon's energy, Eg is the optical band gap, and A is a proportionality constant in this equation.

It was found that the optimum Al doping concentration of 8 mol% for ZnO nanorods (NRs) at varying temperatures of 250 °C, 350 °C, and 450 °C resulted in a maximum transmittance of 60%. The diffuse reflection band gap was observed to range from 3.14 eV to 3.17 eV for ZnO NRs, as shown in Figure 5.21.

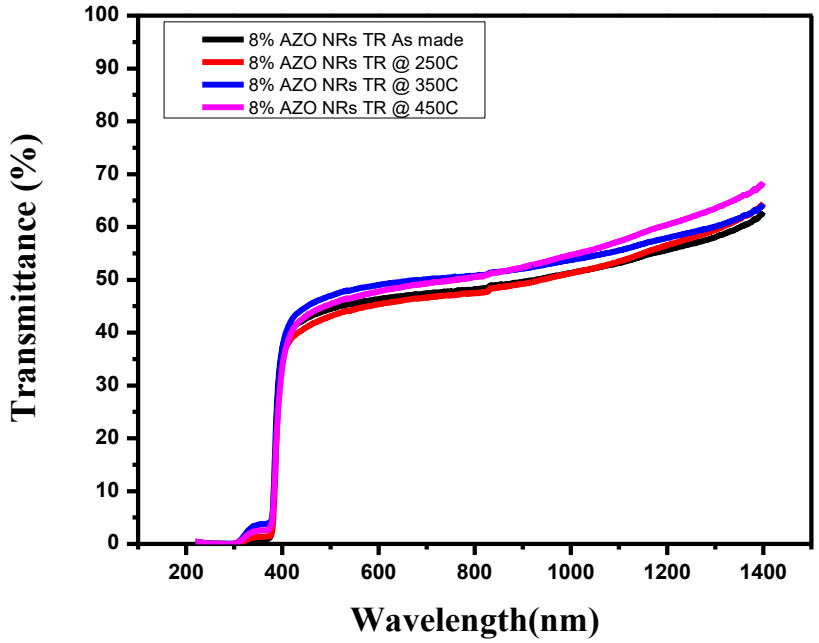

(a)

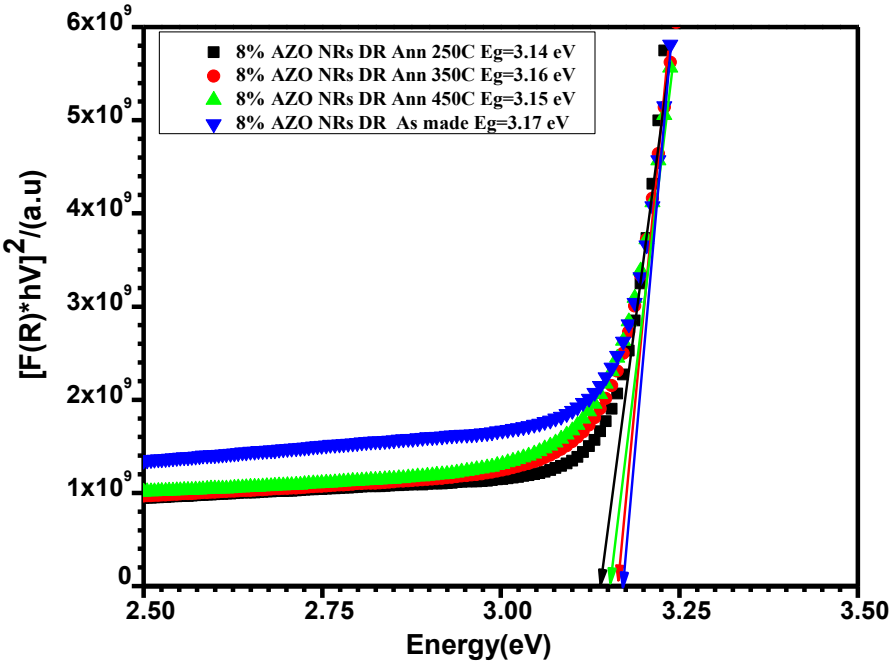

(b)

Figure 5.21: Variation of a) Transmittance vs. wavelength, b) Band gap energy of ZnO NRs at 8% doping concentration at different temperatures.

5.4.5 post-annealing effect on Electrical resistivity of sheet resistance ($R_{□}$).

We calculated the sheet resistance by multiplying the geometrical correction factor (f_1) (Farhad et al). So, after simplifying the above equation, we finally calculated the sheet resistance from the following equation:

$$R_{sh}=4.53 \times f_1 \times R_{4pp}$$

Where f_1 is the geometrical correction factor that depends on the geometry of the substrate.

R_{4pp} is the 4-point collinear probe resistance determined by using Ohm's law.

The sheet resistance was measured after annealing at 250 °C, 350 °C, and 450 °C. The sheet resistance values were measured at 1.76 MΩ/Square, 4.22 MΩ/Square, and 5.66 MΩ/Square, respectively. The lowest sheet resistance of 1.76 MΩ/Square was recorded at 250 °C for 8 mol% ZnO NR, as shown in Table 5.10. Sheet resistance has also decreased the optimum concentration of Al-doping (8 mol%) at different temperatures of ZnO NRs.

Table 5.10: Sheet Resistance ($R_{□}$) of ZnO NRs after annealing on SLG.

ZnO NRs ON AZO	**Al – Doping (%)**	**After Annealed (MΩ/□)**		
		250 ^{0}C	**350 ^{0}C**	**450 ^{0}C**
	3%	297.87 MΩ/□	203.36 MΩ/□	201.06 MΩ/□
	3%	197.87 MΩ/□	133.36 MΩ/□	101.06 MΩ/□
	5%	788.87 MΩ/□	135.36 MΩ/□	145.56 MΩ/□
	8%	01.76 MΩ/□	04.22 MΩ/□	05.66 MΩ/□

So, to summarize the post-annealing temperature significantly influences the structural and optical properties of ZnO nanorods (ZnONRs). At different annealing temperatures (250 °C, 350 °C, and 450 °C), changes in the nanorod characteristics were observed. At 250 °C, the ZnO NRs exhibited optimal crystallization, with a high crystallite size and low full-width at half-maximum (FWHM), indicating high-quality growth. The sharp intensity peak in the near-band-

edge (NBE) region increased, while the visible emission peak decreased, suggesting improved alignment and crystallinity.

The NBE emission at 380 nm decreased with increasing annealing temperature up to 350 °C and 450 °C, but a strong visible emission appeared at 600 nm. These variations in emission behavior are attributed to the changes in the electrical properties of the nanorods, which are attributed to the generation of more oxygen vacancies and defects at elevated temperatures. In addition, the optical properties of the ZnO NRs are consistent with their band gap, which is obtained from photoluminescence (PL) and diffuse reflection spectra, ranging from 3.12 to 3.16 eV. Specifically, it was found that the green emission peak of the visible region was decreased at the annealing temperature of 250 °C, indicating that the thin film had higher optical properties.

Chapter 6: Conclusion and Suggestions for Future Work

6.1 Conclusion

This thesis presents a comprehensive study on the synthesis, characterization, and optimization of aluminium-doped zinc oxide (AZO) seed layers and vertically aligned zinc oxide (ZnO) nanorods (NRs) grown on AZO-seeded soda-lime glass substrates for potential optoelectronic applications. Spin coating and hydrothermal techniques were employed for the fabrication of AZO seed layers and ZnO NRs, respectively. The effects of varying Al doping concentrations (2, 3, 5, and 8 mol%) and post-deposition annealing temperatures (250 °C, 350 °C, and 450 °C) were thoroughly investigated with respect to structural, morphological, optical, electrical, and photoluminescence properties.

Surface morphology and structural evolution were systematically evaluated using SEM, XRD. SEM analysis confirmed the successful deposition of uniformly distributed AZO seed layers with thicknesses ranging from 178 nm to 731 nm and average grain diameters between 186 nm and 246 nm. No direct correlation was observed between increasing Al doping concentration and film thickness. The EDX spectroscopy verified the elemental composition, confirming the incorporation of Zn, O, and Al. Electrical measurements of AZO seed thin films revealed that resistivity decreased with increasing Al content in the seed layers, ranging from (41.47 ± 3.98) kΩ·cm to (13.00 ± 0.21) kΩ·cm, indicating enhanced electrical conductivity and improved charge transport due to Al doping.

Hydrothermally grown ZnO nanorods exhibited a well-aligned hexagonal wurtzite crystal structure, as verified by XRD and SEM. The rod density and aspect ratio were significantly influenced by both doping and annealing conditions, with optimal morphology and crystallinity observed at an annealing temperature of 250 °C. The nanorods exhibited c-axis orientation along the (002) plane, with the highest peak intensity and largest crystallite size (48.58 nm) observed at 8 mol% doping. A decrease in crystallite size and an increase in full width at half

maximum (FWHM) were observed with further increases in annealing temperature, indicating a reduction in crystalline quality.

The PL studies revealed significant improvement in optical quality at optimal doping and annealing conditions. Before annealing, dual emission was observed: a near-band-edge (NBE) peak at ~380 nm in the UV region and a broad deep-level emission (DLE) in the visible region (500–700 nm). Post-annealing at 250 °C, the NBE emission intensity markedly increased, while the DLE diminished, particularly at 8 mol% doping, indicating a reduction in structural defects and enhanced crystal quality. This suppression of defect-related emission signifies the successful optimization of both composition and thermal treatment for optoelectronic quality.

The optical band gap of AZO seed layers varied between 3.44 and 3.55 eV, depending on the doping concentration, while ZnO NRs exhibited band gap values between 3.05 and 3.15 eV as estimated from diffuse reflectance data using the Tauc method. These values were corroborated by photoluminescence NBE emissions in the 3.22–3.25 eV range. Notably, the optimal doping concentration (8 mol%) combined with an annealing temperature of 250 °C yielded the most desirable optical and structural properties, with corresponding diffuse reflectance and PL band gaps closely matching at 3.15 eV and 3.22 eV, respectively.

The transmittance spectra confirmed that both AZO seed layers and ZnO nanorods are highly transparent in the visible range, achieving up to 90% transmission. Such transparency, combined with enhanced electrical conductivity and strong NBE photoluminescence, underlines the potential of these nanostructured materials for use in transparent optoelectronic devices.

In summary, this research demonstrates that careful control of aluminum doping concentration on seed layers and post-annealing temperature to AZO/ZnO nanostructures enables the fabrication of high-quality, vertically aligned ZnO nanorods with tunable structural and optoelectronic properties. The findings contribute significantly to the understanding and

practical development of AZO/ZnO-based nanomaterials for future applications in photovoltaics, LEDs, sensors, and other transparent electronic devices.

6.2 Suggestion for Future Work

In the future, the following characterizations can be performed to gain a better understanding of the properties of the thin film materials.

- The potential of Al-doped ZnO nanorods (NRs) as a high-performance electron transport layer (ETL) can be explored.
- Raman spectroscopy can be performed for ZnO NR
- The photocatalytic activity and antibacterial properties of Al-doped ZnO nanorod films studied.

References

[1] Owusu, P. A., & Asumadu-Sarkodie, S. (2016). A review of renewable energy sources, sustainability issues and climate change mitigation. *Cogent Engineering*, *3*(1), 1167990.

[2] Dorling, D. (2021). World population prospects at the UN: our numbers are not our problem. In *The struggle for social sustainability* (pp. 129-154). Policy Press.

[3] Newell, R., Raimi, D., Villanueva, S., & Prest, B. (2020). Global Energy Outlook 2020: energy transition or energy addition. *Resources for the Future*.

[4] International Energy Agency (IEA), "Global Energy Demand," IEA Report, 2020

[5] Sourmehi, C. (2021). EIA projects nearly 50% increase in world energy use by 2050, led by growth in renewables. *Today in Energy*, 1.

[6] De Angelis, F. (2018). Perovskite Solar Cells in the Public Domain as the Community Gears Up for Technical Advances. *ACS Energy Letters*, *3*(4), 890-891.

[7] National Renewable Energy Laboratory (NREL), "Benefits of Solar Energy," NREL Report, 2020.

[8] Abel, D., Holloway, T., Harkey, M., Rrushaj, A., Brinkman, G., Duran, P., Janssen, M., & Denholm, P. (2018). Potential air quality benefits from increased solar photovoltaic electricity generation in the Eastern United States. *Atmospheric Environment, 175*, 65–74. https://doi.org/10.1016/j.atmosenv.2017.11.049

[9] Kannan, N., & Vakeesan, D. (2016). Solar energy for the future world: -A review. *Renewable and sustainable energy reviews*, *62*, 1092-1105.

[10] Kishore, T. S., Kumar, P. U., & Ippili, V. (2025). Review of global sustainable solar energy policies: Significance and impact. *Innovation and Green Development*, *4*(2), 100224.

[11] https://en.wikipedia.org/wiki/Swanson%27s_law?utm_source

[12] Kojima, A., Teshima, K., Shirai, Y., & Miyasaka, T. (2009). Organometal halide perovskites as visible-light sensitizers for photovoltaic cells. *Journal of the american chemical society*, *131*(17), 6050-6051.

[13] Romeo, A., & Artegiani, E. (2021). CdTe-Based Thin Film Solar Cells: Past, Present and Future. *Energies*, *14*(6), 1684. https://doi.org/10.3390/en14061684

[14] Green, M. A. (2006). Third-generation photovoltaics.

[15] Taberna, P. L., Simon, P., & Fauvarque, J. F. (2003). Electrochemical characteristics and impedance spectroscopy studies of carbon-carbon supercapacitors. *Journal of the Electrochemical Society*, *150*(3), A292.

[16] S. F. U. Farhad, N. I. Tanvir, M. S. Bashar, M. S. Hossain, M. Sultana, and N. Khatun, "Synthesis of Oriented Zinc Oxide Seed Layer for the Hydrothermal Growth of Zinc Oxide Nanorods," Bangladesh Journal of Scientific and Industrial Research, vol. 53, no. 4, pp. 335-340, 2018, doi: 10.3329/bjsir. V53i4.39186.

[17] Kötz, R., & Carlen, M. J. E. A. (2000). Principles and applications of electrochemical capacitors. *Electrochimica acta*, *45*(15-16), 2483-2498.

[18] Kim, B. K., Sy, S., Yu, A., & Zhang, J. (2015). Electrochemical supercapacitors for energy storage and conversion. *Handbook of clean energy systems*, 1-25.

[19] Zhang, Q., Dandeneau, C. S., Zhou, X., and Cao, G., "ZnO Nanostructures for Dye-Sensitized Solar Cells," Adv. Mater. vol. 21, pp. 4087–4108, 2009.

[20] Maldonado, F., and Stashans, A., "Al-doped ZnO: Electronic, Electrical and Structural Properties," J. Phys. Chem. Solids, vol. 71, pp. 784–787, 2010.

[21] Basyooni, M. A., Shaban, M., and Sayed, A. M. E., "Enhanced Gas Sensing Properties of Spin coated Na-doped ZnO Nanostructured Films," Sci. Rep., vol. 7, pp. 41716, 2017.

[22] Taabouche, A., "Properties of Cobalt-doped Zinc Oxide Thin Films Grown by Pulsed Laser Deposition on Glass Substrates," Matter. Sci. Semicond. Process, vol. 28, pp. 54–58, 2014.

[23] Ceylan, H., Akgun, C. O., Erkal, T. S., Donmez, I., Garifullin, R., Tekinay, A. B., Usta, H., Biyikli, N., and Guler, M. O., "Size-controlled Conformal Nanofabrication of Biotemplated Three-Dimensional TiO_2 and ZnO Nanonetworks," Sci. Rep., vol. 3, pp. 2306, 2013.

[24] Nair, G. M., Nirmala, M., Rekha, K., and Anukalini, A., "Structural, Optical, Photo Catalytic and Antibacterial Activity of ZnO and Co Doped ZnO Nanoparticles," Mater. Lett., vol. 65, pp. 1797–1800, 2011.

[25] Farhad, S. F. U., Hossain, M. A., Tanvir, N. I., Akter, R., Patwary, M. A. M., Shahjahan, M., & Rahman, M. A. (2019). Structural, optical, electrical, and

photoelectrochemical properties of cuprous oxide thin films grown by modified SILAR method. *Materials Science in Semiconductor Processing*, *95*, 68-75.

[26] Calnan, S., & Tiwari, A. N. (2010). High mobility transparent conducting oxides for thin film solar cells. *Thin solid films*, *518*(7), 1839-1849.

[27] Wang, Q., Yang, H., Meng, T., Yang, J., Huang, B., Gu, F. L., ... & Tong, Y. (2021). Boosting electron transfer with heterointerface effect for high-performance lithium-ion storage. *Energy Storage Materials*, *36*, 365-375.

[28] Salam, S., Islam, M., & Akram, A. (2013). Sol–gel synthesis of intrinsic and aluminum-doped zinc oxide thin films as transparent conducting oxides for thin film solar cells. *Thin Solid Films*, *529*, 242-247.

[29] Islam, M. R., Rahman, M., Farhad, S. F. U., & Podder, J. (2019). Structural, optical and photocatalysis properties of sol–gel deposited Al-doped ZnO thin films. *Surfaces and Interfaces*, *16*, 120-126.

[30] Farhad, S. F. U., Tanvir, N. I., Bashar, M. S., Hossain, M. S., Sultana, M., & Khatun, N. (2018). Facile synthesis of oriented zinc oxide seed layer for the hydrothermal growth of zinc oxide nanorods. *Bangladesh Journal of Scientific and Industrial Research*, *53*(4), 233-244.

[31] Oktik, Ş. (2022). The holy triangle of science, technology and industry for photovoltaic solar energy conversion. In Renewable Energy Based Solutions (pp. 51-80). Cham: Springer International Publishing.

[32] Hempstead, C. A. (1977). *Semiconductors 1853-1919: an historical study of selenium and some related materials* (Doctoral dissertation, Durham University).

[33] Nelson, J. A. (2003). *The physics of solar cells*. World Scientific Publishing Company.

[34] https://www.researchgate.net/publication/274961489_Chapter_1_History_of_Solar_Cell_Development.

[35] Wu, X., Asher, S., Levi, D. H., King, D. E., Yan, Y., Gessert, T. A., & Sheldon, P. (2001). Interdiffusion of CdS and Zn 2 SnO 4 layers and its application in CdS/CdTe polycrystalline thin-film solar cells. *Journal of Applied Physics*, *89*(8), 4564-4569.

[36] Shukla, V., & Panda, G. (2020). The performance study of CdTe/CdS/SnO2 solar cell. *Materials Today: Proceedings*, *26*, 487-491.

[37] Ellmer, K., Klein, A. (2008). ZnO and Its Applications. In: Ellmer, K., Klein, A., Rech, B. (eds) Transparent Conductive Zinc Oxide. Springer Series in Materials Science, vol 104. Springer, Berlin, Heidelberg. https://doi.org/10.1007/978-3-540-73612-7_1

[38] Soylu, M., & Yakuphanoglu, F. (2016). Fabrication and characterization of light-sensing device based on transparent ZnO thin film prepared by sol-gel. *Optik*, *127*(20), 8479-8486.

[39] Sharma, D. K., Shukla, S., Sharma, K. K., & Kumar, V. (2022). A review on ZnO: Fundamental properties and applications. Materials Today: Proceedings, 49, 3028-3035.

[40] Coleman, V. A., & Jagadish, C. (2006). Basic properties and applications of ZnO. In *Zinc oxide bulk, thin films and nanostructures* (pp. 1-20). Elsevier Science Ltd.

[41] Fan, J. C., Sreekanth, K. M., Xie, Z., Chang, S. L., & Rao, K. V. (2013). p-Type ZnO materials: Theory, growth, properties and devices. *Progress in Materials Science*, *58*(6), 874-985.

[42] Hegde, M., Mohammadbeigi, F., Kure, T., Senthil Kumar, E., Wagner, M. R., Hoffmann, A., & Watkins, S. P. (2020). Triple group-V donors in ZnO. *Journal of Applied Physics*, *127*(7).

[43] Manzen, I., Yoshimura, Y., Matsubara, K., & Nitta, A. (2020). Improvement of characteristics of flexible Al-doped ZnO/Ag/Al-doped ZnO transparent conductive film using silver. *J. Vac. Sci. Technol. B* 38, 022205 (2020) https://doi.org/10.1116/1.5137796

[44] Mandal, S., Basak, A., & Singh, U. P. (2021). Effect of post annealing on the properties of aluminium doped Zinc oxide thin films deposited by DC sputtering. *Materials Today: Proceedings*, 47, 1821–1828. https://doi.org/10.1016/j.matpr.2020.05.029

[45] Agarwal, M. B., Malaidurai, M., Sharma, A., & Thangavel, R. (2020). Effect of Al doping on hydrothermal growth and physical properties of doped ZnO nanoarrays for optoelectronic applications. *Materials Today: Proceedings*, *21*, 1781-1786. DOI: 10.1016/j.matpr.2020.01.231

[46] Sarma, B., Barman, D., & Sarma, B. K. (2019). Structural, optical, and electrical properties of doped ZnO thin films. Applied Surface Science, 479, 786–795. https://doi.org/10.1016/j.apsusc.2019.01.256.

[47] Farhad, S. F. U., Tanvir, N. I., Bashar, M. S., & Sultan, M. (Year not specified). Title not specified. MRS Advances. Manuscript ID: MRSAdv-2018-3015965.

[48] Tonny, K. N., Rafique, R., Sharmin, A., Bashar, M. S., & Mahmood, Z. H. (2018). Structural and optical properties of ZnO thin films deposited by sol–gel technique. AIP Advances, 8(6), 065307. https://doi.org/10.1063/1.5023020.

[49] Farhad, S. F. U., Tanvir, N. I., Bashar, M. S., Hossain, M. S., Sultana, M., & Khatun, N. (2018). Structural and optical properties of ZnO thin films prepared by sol-gel method. Bangladesh Journal of Scientific and Industrial Research, 53(4), 233–244.

[50] Shahid, M. U., Deen, K. M., Ahmad, A., Akram, M. A., Aslam, M., & Akhtar, W. (2016). Structural and optical properties of ZnO thin films deposited by sol–gel method. *Applied Nanoscience*, 6, 235–241. https://doi.org/10.1007/s13204-015-0425-7

[51] Narayanan, G. N., Ganesh, R. S., & Karthigeyan, A. (2016). Effect of annealing on structural, optical and electrical properties of ZnO thin films deposited by spray pyrolysis. *Thin Solid Films*, 603, 148–155. https://doi.org/10.1016/j.tsf.2015.11.071.

[52] Kim, K. H., Jin, Z., Abe, Y., & Kawamura, M. (2014). Effect of Al doping on the properties of ZnO thin films prepared by sol-gel method. Superlattices and Microstructures, 75, 455–460. https://doi.org/10.1016/j.spmi.2014.07.033

[53] Kim, S., Nam, G., Park, H., Yoon, H., Lee, S.-h., Kim, J. S., Kim, D. Y., Kim, S.-O., & Leem, J. Y. (2013). Electrical and optical properties of Al-doped ZnO thin films prepared by sol–gel method. Bulletin of the Korean Chemical Society, 34(4), 1205–1210. https://doi.org/10.5012/bkcs.2013.34.4.1205

[54] Cai, X., Li, X., Liu, L., Zhu, J., & Wang, Y. (2011). Structural, optical and electrical properties of Al-doped ZnO thin films prepared by sol–gel method. *Superlattices and Microstructures*, 50(3), 311–318. https://doi.org/10.1016/j.spmi.2011.05.013

[55] Benelmadjat, H., Touka, N., Harieche, B., Boudine, B., Halimi, O., & Sebais, M. (2010). Structural and optical properties of Al-doped ZnO thin films prepared by sol–

gel spin coating. *Optical Materials*, 32(4), 764–767. https://doi.org/10.1016/j.optmat.2010.01.015

[56] Smirnov, M., Baban, C., & Rusu, G. I. (2010). Influence of substrate temperature on the properties of ZnO:Al thin films prepared by RF magnetron sputtering. *Applied Surface Science*, 256(8), 2405–2408. https://doi.org/10.1016/j.apsusc.2009.09.064

[57] Ratana, T., Amornpitoksuk, P., Ratana, T., & Suwanboon, S. (2009). Structural and optical properties of Al-doped ZnO thin films prepared by sol–gel method. Journal of Alloys and Compounds, 470(1–2), 408–412. https://doi.org/10.1016/j.jallcom.2008.02.069

[58] Czternastek, H. (2004). Electrical and optical properties of ZnO:Al thin films deposited by spray pyrolysis. *Opto-Electronics Review*, 12(1), 49–52.

[59] Shishiyanu, S. T., Shishiyanu, T. S., & Lupan, O. I. (2005). Sensing characteristics of tin-doped ZnO thin films as NO₂ gas sensor. Sensors and Actuators B: Chemical, 107(2), 379–386. https://doi.org/10.1016/j.snb.2004.11.072

[60] López, R., Ibáñez, R., Romero, R., Martín, F., Ramos-Barrado, J. R., & Leinen, D. (2006). Deposition of ZnO thin films by spray pyrolysis: relationship between the growth conditions and the electrical, structural and optical properties. *Surface and Interface Analysis*, 38(6), 789–792. https://doi.org/10.1002/sia.2273.

[61] Mahalingam, T., John, V. S., & Hsu, L. S. (2007). Electrodeposition and characterization of ZnO thin films. Journal of New Materials for Electrochemical Systems, 10, 9–14.

[62] Zhao, L., Lian, J., Liu, Y., & Jiang, Q. (2006). Influence of substrate temperature on the structural and optical properties of ZnO thin films deposited by pulsed laser deposition. Applied Surface Science, 252(24), 8451–8455. https://doi.org/10.1016/j.apsusc.2005.10.054.

[63] Inoue, Y., Okamoto, M., Kawahara, T., Okamoto, Y., & Morimoto, J. (2005). Structural and optical properties of Al-doped ZnO thin films prepared by pulsed laser deposition. Materials Transactions, 46(7), 1470–1475. https://doi.org/10.2320/matertrans.46.1470

[64] Zhao, L., Lian, J., Liu, Y., & Jiang, Q. (2013). Influence of substrate temperature on the structural and optical properties of ZnO thin films deposited by pulsed laser

deposition. *Applied Surface Science*, 252(24), 8451–8455. https://doi.org/10.1016/j.apsusc.2005.10.054:contentReference[oaicite:5]{index=5}

[65] Gumus, C. E. B. R. A. İ. L., Ozkendir, O. M., Kavak, H., & Ufuktepe, Y. Ü. K. S. E. L. (2006). Structural and optical properties of zinc oxide thin films prepared by spray pyrolysis method. *Journal of optoelectronics and advanced materials*, *8*(1), 299.

[66] Mitra, P., & Mukhopadhyay, A. K. (2007). ZnO thin film as methane sensor. *Bulletin of the Polish Academy of Sciences Technical Sciences | 2007 | vol. 55 | No 3* | *281-285*

[67] Suwanboon, S., Ratana, T., & Ratana, T. (2007). Structural and optical properties of ZnO thin films prepared by sol–gel method. Walailak Journal of Science and Technology, 4(1), 111–121.

[68] Hwang, D.-K., Oh, M.-S., Lim, J.-H., & Park, S.-J. (2007). Recent progress in ZnO-based optoelectronic devices. Journal of Physics D: Applied Physics, 40(13), R387–R412. https://doi.org/10.1088/0022-3727/40/13/R01

[69] Ilican, S., Caglar, Y., & Caglar, M. (2008). Optical and structural properties of ZnO thin films deposited by sol–gel spin coating method. Journal of Optoelectronics and Advanced Materials, 10(10), 2578–2583.

[70] Djelloul, A., Bouzid, K., & Guerrab, F. (2008). Role of substrate temperature on the structural and morphological properties of ZnO thin films deposited by ultrasonic spray pyrolysis. Turkish Journal of Physics, 32(1), 49-58.

[71] Mondal, S., Kanta, K. P., & Mitra, P. (2008). Structural and optical properties of ZnO thin films prepared by spray pyrolysis. *Journal of Physical Sciences*, 12, 221–229.

[72] Rahmani, M. B., Keshmiri, S. H., Shafiei, M., Latham, K., Wlodarski, W., du Plessis, J., & Kalantar-Zadeh, K. (2009). ZnO-based gas sensors: A review. Sensor Letters, 7, 1–8. https://doi.org/10.1166/sl.2009.1041

[73] Xu, L., Li, X., Chen, Y., & Xu, F. (2011). Structural and optical properties of Al-doped ZnO thin films prepared by sol–gel method. Applied Surface Science, 257(9), 4031–4037. https://doi.org/10.1016/j.apsusc.2011.01.051.

[74] Singh, G., Shrivastava, S. B., Jain, D., Pandya, S., Shripathi, T., & Ganesan, V. (2010). Structural and optical properties of Al-doped ZnO thin films prepared by sol–

gel method. *Bulletin of Materials Science*, 33(5), 581–587. https://doi.org/10.1007/s12034-010-0077-0

[75] Hoang, L. H., Khoi, N. T., Hai, N. H., Pacuski, W., & Yang, I.-S. (2008). Optical and magnetic properties of Co-doped ZnO films grown by pulsed laser deposition. *Journal of the Korean Physical Society*, 52(5), 1621–1624. https://doi.org/10.3938/jkps.52.1621

[76] Islam, M. R., Rahman, M., Farhad, S. F. U., & Podder, J. (2019). Structural, optical and photocatalysis properties of sol–gel deposited Al-doped ZnO thin films. Surfaces and Interfaces, 16, 120-126.

[77] West, A. R. *Solid State Chemistry*. John Wiley & Sons, Singapore, 2003.

[78] Chopra, K. L. *Thin Film Phenomena*. McGraw-Hill, New York, 1969.

[79] Kern, W., & Schuegraf, K. K. (2001). Deposition technologies and applications: Introduction and overview. In *Handbook of Thin Film Deposition Processes and Techniques* (pp. 11-43). William Andrew Publishing.

[80] Sakthinathan S, Meenakshi GA, Vinothini S, Yu C-L, Chen C-L, Chiu T-W, Vittayakorn N. A Review of Thin-Film Growth, Properties, Applications, and Future Prospects. *Processes*. 2025; 13(2):587. https://doi.org/10.3390/pr13020587

[81] **https://www.researchgate.net/profile/Mebrouk-Ghougali**

[82] Farhad, S. F. U., Hossain, M. A., Tanvir, N. I., Akter, R., Patwary, M. A. M., Shahjahan, M., & Rahman, M. A. (2019). Structural, optical, electrical, and photoelectrochemical properties of cuprous oxide thin films grown by modified SILAR method. *Materials Science in Semiconductor Processing*, *95*, 68-75.

[83] Asvarov, A. S., Abduev, A. K., Akhmedov, A. K., & Kanevsky, V. M. (2022). On the Effect of the Co-Introduction of Al and Ga Impurities on the Electrical Performance of Transparent Conductive ZnO-Based Thin Films. *Materials*, *15*(17), 5862.

[84] Aleksandrova, M., Ivanova, T., Strijkova, V., Tsanev, T., Singh, A. K., Singh, J., & Gesheva, K. (2021). Ga-Doped ZnO Coating—A Suitable Tool for Tuning the Electrode Properties in the Solar Cells with CdS/ZnS Core-Shell Quantum Dots. *Crystals*, *11*(2), 137.

[85] Singh, Girjesh, et al. (2010). *Studies on ZnO thin films for optoelectronic applications*. Bulletin of Materials Science**,** Reports on n-type conductivity and optical band gap of ZnO thin films. 33(5)**,** 581–587., DOI: [10.1007/s12034-010-0092-0]

[86] Ilican, S., Caglar, Y., & Caglar, M**.** (2008). *Electrical and optical properties of ZnO thin films*. Journal of Optoelectronics and Advanced Materials**,** 10(10)**,** 2578–2583. Demonstrates Al-doped ZnO (AZO) thin films as transparent n-type semiconductors.

[87] V. Srivastava, E. S. Babu, and S.-K. Hong, "Effect of Al Doping on the Properties of ZnO Nanorods Synthesized by Hydrothermal Growth for Gas Sensor Applications", doi: 10.3740/mrsk.2020.30.8.399

[88] J. Chen et al., "Mechanism and Optimized Process Conditions of Forming One-Dimensional ZnO Nanorods with Al-Doping by Electrodeposition Method," International Journal of Photoenergy, Mar. 2021, doi: 10.1155/2021/8827911

[89] Helenbrook, B. T., Kellerman, P., Carlson, F., Desai, N., & Sun, D. (2016). Experimental and numerical investigation of the horizontal ribbon growth process. *Journal of Crystal Growth*, *453*, 163-172.

[90] Bragg, W. L., & Bragg, W. H. (1913). The Reflection of X-rays by Crystals. Proceedings of the Royal Society A, 88(605), 428-438

[91] Y. Wang, J. Li, and J. Sun, "Effects of Al doping on the morphology of ZnO nanowires and the properties of dye-sensitized solar cells," Dec. 2019.

[92] https://www.sciencedirect.com/topics/materials-science/energy-dispersive-x-ray-analysis

[93] A. T. Ali et al., "UV random laser in aluminum-doped ZnO nanorods," Journal of The Optical Society of America B-optical Physics, Sep. 2021, doi: 10.1364/JOSAB.427132

[94] https://wiki.anton-paar.com/en/x-ray-diffraction-xrd/

[95] Warren, B.E., "X-ray Diffraction", Addision Wesly Publishing Co.: London, (1969).

[96] Hirsch, P. B., Howie, A., Nicholson, R. B., Pashley, D. W., & Whelan, M. J. (1965). *Electron Microscopy of Thin Crystals*. Washington D.C.: Butterworths.

[97] Goldstein, J. I., Newbury, D. E., Joy, D. C., Lyman, C. E., Echlin, P., Lifshin, E., Sawyer, L., & Michael, J. R. (2003). Scanning Electron Microscopy and X-ray Microanalysis (3rd ed.). Springer.

[98] https://biologynotesonline.com/scanning-electron-microscope-principle-parts-uses/

[99] Williams, D. B., & Carter, C. B. (2009).***Transmission Electron Microscopy: A Textbook for Materials Science*** (2nd ed.). Springer.

[100] Gupta, B. K., Agnihotri, O. P., "Structural investigations of spray-deposited CdS films doped with Cu, In and Ga", Phil. Mag.(b), 37, 631-633, (1978).

[101] Kumar, P., Misra, A., Kumar, D., Dhama, N., Sharma, T.P., Dixit, P.N., "Structural and optical properties of vacuum evaporated Cd*x*Zn1−*x*S thin films" Opt. Mater., 27(2), 261–264, (2004).

[102] Abd Mutalib, M., Rahman, M. A., Othman, M. H. D., Ismail, A. F., & Jaafar, J. (2017). Scanning electron microscopy (SEM) and energy-dispersive X-ray (EDX) spectroscopy. In *Membrane characterization* (pp. 161-179). Elsevier.

[103] Nelson, J. B., Riley, D.P., "An experimental investigation of extrapolation methods in the derivation of accurate unit cell dimension of crystals", Proc. Phys. Soc., 57, 160-177, 1945

[104] Cullity, B. D., & Stock, S. R. (2001). Elements of X-Ray Diffraction (3rd ed.). Prentice Hall.

[105] Bedir, M., Oztas, M., Bakkaloglu, O.F., Ormanci, R., "Investigations on Structural, Optical and Electrical Parameters of Spray Deposited ZnSe Thin Films with Different Substrate Temperature", Eur. Phys. J. B 45, 465-471, (2005).

[106] https://upload.wikimedia.org/wikipedia/commons/thumb/0/0d/Schema_MEB_%28en%29.svg/560px-Schema_MEB_%28en%29.svg.png

[107] Lee C-S, Kim J., Son J. Y., Maeng W. J., Jo D-H, Choi W., Kim H., "Plasma-enhanced ALD of TiO2 thin films on SUS 304 stainless steel for photocatalytic application", J. Electrochem. Soc., 156, 5, pp. 188-192, 2009.

[108] Poelman, D., & Smet, P. F. (2003). Methods for the determination of the optical constants of thin films from single transmission measurements: a critical review. *Journal of Physics D: Applied Physics*, *36*(15), 1850.

[109] Rey, G., Spindler, C., Babbe, F., Rachad, W., Siebentritt, S., Nuys, M., ... & Platzer-Björkman, C. (2018). Absorption coefficient of a semiconductor thin film from photoluminescence. *Physical Review Applied*, *9*(6), 064008.

[110] Rey, G., Spindler, C., Babbe, F., Rachad, W., Siebentritt, S., Nuys, M., ... & Platzer-Björkman, C. (2018). Absorption coefficient of a semiconductor thin film from photoluminescence. *Physical Review Applied*, *9*(6), 064008.

[111] Lee, K. E., Wang, M., Kim, E. J., & Hahn, S. H. (2009). Structural, electrical and optical properties of sol–gel AZO thin films. Current Applied Physics, 9(3), 683-687.

[112] Subramanyam, T. K., Goutham, P., Kumar, S. P., Yadhuraj, S. R., & Geetha, K. S. (2018). Optimization of sputtered AZO thin films for device application. Materials Today: Proceedings, 5(4), 10851-10859.

[113] Lourenço, M. A., Siddiqui, M. S. A., Gwilliam, R. M., Shao, G., & Homewood, K. P. (2003). Efficient silicon light emitting diodes made by dislocation engineering. *Physica E: Low-dimensional Systems and Nanostructures*, *16*(3-4), 376-381.

[114] Wang, F., Wu, M. Z., Wang, Y. Y., Yu, Y. M., Wu, X. M., & Zhuge, L. J. (2013). Influence of thickness and annealing temperature on the electrical, optical and structural properties of AZO thin films. *Vacuum*, *89*, 127-131.

[115] Sinkkonen, A. (2023). GOLD THIN FILM FABRICATION AND RESISTIVITY CHARACTERIZATION.

[116] https://www.electronicdesign.com/technologies/industrial/article/21206843/materials-characterization-resistivity-measurements-using-a-four-point-collinear-probe

[117] Bunn, C.W., “A Comparative Review of ZnO Materials and Devices”, Proc. Phys. Soc. London. 47, 835, (1935).

[118] Allenic, A. L., “Structural, Electrical and Optical Properties of P-type Zinc Oxide Epitaxial Films”, Ph.D. thesis, University of Michigan: ProQuest, (2008).

[119] Özgür, Ü. , Alivov, Y. I., Liu, C., Teke, A., Reshchikov, M. A., Doğan, S., Avrutin, V., Cho, S.J., Morkoç, H., "A comprehensive review of ZnO materials and devices", J. Appl. Phys., 98 (4), 041301-1-041301-101, (2005).

[120] Schmidt-Mende, L., & MacManus-Driscoll, J. L. (2007). ZnO–nanostructures, defects, and devices. *Materials today*, *10*(5), 40-48.

[121] Rossler , U., Bornstein, L, “New Series, Group III.17B, 22, 41B”, Springer: Heidelberg, (1999).

[122] Liu, Z. F., Wu, M. F., Zheng, F. K., Wang, S. H., Zhang, M. J., Chen, J., ... & Wu, A. Q. (2013). Zinc (ii) coordination compounds based on in situ generated 3-(5 H-tetrazol) benzaldehyde with diverse modes: hydrothermal syntheses, crystal structures and photoluminescent properties. *CrystEngComm*, *15*(35), 7038-7047.

[123] Klingshirn, C. F., Waag, A., Hoffmann, A., Geurts, J., "Zinc Oxide: From Fundamental Properties Towards Novel Applications", Springer Series in Materials Science. 120, Springer Science & Business Media, (2010).

[124] Talwar, D. N., & Becla, P. (2025). Systematic Simulations of Structural Stability, Phonon Dispersions, and Thermal Expansion in Zinc-Blende ZnO. *Nanomaterials*, *15*(4), 308.

[125] Roth, A. P., & Williams, D. F. (1981). Properties of zinc oxide films prepared by the oxidation of diethyl zinc. *Journal of Applied Physics*, *52*(11), 6685-6692.

[126] Mondolfo, L. F. (2013). *Aluminium alloys: structure and properties*. Elsevier, https://www.politicalfunda.com/2024/02/aluminum-descriptions-chemical-and-physical-properties-uses-and-facts.html.

[127] Mahan, J. E., "Physical Vapor Deposition of Thin Films", John Wiley & Sons: New York, (2000).

[128] Dobkin, D., Zuraw, M. K., "Principles of Chemical Vapor Deposition", Springer Science & Business Media, (2003).

[129] Lincot, D., Hodes, G., "Chemical Solution Deposition of Semiconducting and Non-metallic Films", Proc. Int. Symp. Electrochem. Soc., 2003-2032, (2006).

[130] Hench, L. L., West, J.K., "The Sol-Gel Process", Chem. Rev., 90(1), 33-72, (1990).

[131] Chamberlin, R. R., Skarman, J. S., "Chemical spray deposition process for inorganic films", J. Electrochem. Soc., 113(1), 86-89, (1966).

[132] https://images.app.goo.gl/3628miFv8FrYcieg8

[133] Wang, Y., Xu, G., Yang, J., Mao, W., Wang, J., Liu, Z., ... & Li, J. (2022). Fabrication of AZO and FAZO films using low-cost spin-coating method. *Optical Materials*, *126*, 112204.

[134] Tonny, K. N., Rafique, R., Sharmin, A., Bashar, M. S., & Mahmood, Z. H. (2018). Electrical, optical and structural properties of transparent conducting Al doped ZnO (AZO) deposited by sol-gel spin coating. *AIP Advances*, *8*(6).

[135] A. Sugunan, H. C. Warad, M. Boman, and J. Dutta, "Zinc oxide nanowires in chemical bath on seeded substrates: Role of hexamine," *J. Sol-Gel Sci. Technol.*, vol. 39, no. 1, pp. 49–56, May 2006.

[136] S. Baruah and J. Dutta, "Effect of seeded substrates on hydrothermally grown ZnO nanorods," *J. Sol-Gel Sci. Technol.*, vol. 50, no. 3, pp. 456–464, Feb. 2009.

[137] M. Law, L. E. Greene, J. C. Johnson, R. Saykally, and P. Yang, "Nanowire dye-sensitized solar cells.," *Nat. Mater.*, vol. 4, no. 6, pp. 455–9, Jun. 2005. R. B. M. Cross, M. M. De Souza, and E. M. Sankara Narayanan, "A low temperature combination method for the production of ZnO nanowires.," *Nanotechnology*, vol. 16, no. 10, pp. 2188–92, Oct. 2005.

[138] S. J. Henley, M. N. R. Ashfold, D. P. Nicholls, P. Wheatley, and D. Cherns, "Controlling the size and alignment of ZnO microrods using ZnO thin film templates deposited by pulsed laser ablation," *Appl. Phys. A*, vol. 79, no. 4–6, pp. 1169–1173, Jul. 2004.

[139] J.-S. Huang and C.-F. Lin, "Influences of ZnO sol-gel thin film characteristics on ZnO nanowire arrays prepared at low temperature using all solution-based processing," *J. Appl. Phys.*, vol. 103, no. 1, p. 014304, 2008.

[140] Y. Sun, N. George Ndifor-Angwafor, D. Jason Riley, and M. N. R. Ashfold, "Synthesis and photoluminescence of ultra-thin ZnO nanowire/nanotube arrays formed by hydrothermal growth," *Chem. Phys. Lett.*, vol. 431, no. 4–6, pp. 352–357, Nov. 2006.

[141] Farhad, S. F. U., Tanvir, N. I., Bashar, M. S., Hossain, M. S., Sultana, M., & Khatun, N. (2018). Facile synthesis of oriented zinc oxide seed layer for the hydrothermal growth of zinc oxide nanorods. *Bangladesh Journal of Scientific and Industrial Research*, *53*(4), 233-244.

[142] Farhad, S. F. U., Tanvir, N. I., Bashar, M. S., & Sultana, M. (2019). Synthesis and characterization of c-axis oriented Zinc Oxide thin film and its use for the subsequent hydrothermal growth of Zinc Oxide nanorods. *MRS Advances*, *4*(16), 921-928.

[143] Vayssieres, L. (2003). Growth of arrayed nanorods and nanowires of ZnO from aqueous solutions. *Advanced Materials*, *15*(5), 464-466.

[144] R. Tena-Zaera, J. Elias, G. Wang, and C. Levy-Clement, "Role of chloride ions on electrochemical deposition of ZnO nanowire Arrays from O-2 reduction," *J. Phys. Chem. B*, vol. 111, no. 45, pp. 16706–16711, 2007.

[145] Rajamanickam, S., Prasanna, J., & Chandrasekhara Sastry, C. (2020). Analysis of high aspect ratio small holes in rapid electrical discharge machining of superalloys using Taguchi and TOPSIS. *Journal of the Brazilian Society of Mechanical Sciences and Engineering*, *42*, 1-13.

[146] M. N. R. Ashfold, R. P. Doherty, N. G. Ndifor-Angwafor, D. J. Riley, and Y. Sun, "The kinetics of the hydrothermal growth of ZnO nanostructures," Thin Solid Films, vol. 515, no. 24, pp. 8679–8683, Oct. 2007.

THE END

Mukul Hossain

Fabrication of Zinc Oxide (ZnO) Nanorods on Aluminium Doped ZnO (AZO) Seeding Layers

University of Dhaka

Document Details

Submission ID
trn:oid:::3117:469159016

Submission Date
Jun 23, 2025, 4:27 PM GMT+6

Download Date
Jun 24, 2025, 1:22 PM GMT+6

File Name
Update @ 22.05.25Thesis Final copy.docx

File Size
7.7 MB

105 Pages

22,158 Words

125,518 Characters

3% Overall Similarity

The combined total of all matches, including overlapping sources, for each database

Filtered from the Report

- Bibliography
- Quoted Text
- Small Matches (less than 14 words)

Match Groups

- **36 Not Cited or Quoted 3%**
  Matches with neither in-text citation nor quotation marks
- **2 Missing Quotations 0%**
  Matches that are still very similar to source material
- **0 Missing Citation 0%**
  Matches that have quotation marks, but no in-text citation
- **0 Cited and Quoted 0%**
  Matches with in-text citation present, but no quotation marks

Top Sources

- 3% Internet sources
- 2% Publications
- 0% Submitted works (Student Papers)

Integrity Flags

0 Integrity Flags for Review

No suspicious text manipulations found.

Our system's algorithms look deeply at a document for any inconsistencies that would set it apart from a normal submission. If we notice something strange, we flag it for you to review.

A Flag is not necessarily an indicator of a problem. However, we'd recommend you focus your attention there for further review.

24.06.25

24 JUN 2025
Prof. Dr. Kazi Mostak Gausul Hoq
Librarian (In-charge)
University of Dhaka